ABSTRACT

Title of dissertation: BIO-INSPIRED DISTURBANCE REJECTION
                           WITH OCELLAR AND DISTRIBUTED
                           ACCELERATION SENSING FOR
                           SMALL UNMANNED AIRCRAFT SYSTEMS

                           Gregory Michael Gremillion,
                           Doctor of Philosophy, 2015

Dissertation directed by: Professor J. Sean Humbert
                           Department of Aerospace Engineering

Rapid sensing of body motions is critical to stabilizing a flight vehicle in the presence of exogenous disturbances as well as providing high performance tracking of desired control commands. This bandwidth requirement becomes more stringent as vehicle scale decreases. In many flying insects three simple eyes, known as the ocelli, operate as low latency visual egomotion sensors. Furthermore many flying insects employ distributed networks of acceleration-sensitive sensors to provide information about body egomotion to rapidly detect external forces and torques. In this work, simulation modeling of the ocelli visual system common to flying insects was performed based on physiological and behavioral data. Linear state estimation matrices were derived from the measurement models to form estimates of egomotion states. A fully analog ocellar sensor was designed and constructed based on these models, producing state estimation outputs. These analog state estimate outputs were characterized in the presence of egomotion stimuli. Feedback from the ocellar

sensor, with and without complementary input from optic flow sensors, was implemented on a quadrotor to perform stabilization and disturbance rejection. The performance of the closed loop sensor feedback was compared to baseline inertial feedback. A distributed array of digital accelerometers was constructed to sense rapid force and torque measurements. The response of the array to induced motion stimuli was characterized and an automated calibration algorithm was formulated to estimate sensor position and orientation. A linear state estimation matrix was derived from the calibration to directly estimate forces and torques. The force and torque estimates provided by the sensor network were used to augment the quadrotor inner loop controller to improve tracking of desired commands in the presence of exogenous force and torque disturbances with a force-adaptive feedback control.

BIO-INSPIRED DISTURBANCE REJECTION WITH OCELLAR AND DISTRIBUTED ACCELERATION SENSING FOR SMALL UNMANNED AIRCRAFT SYSTEMS

by

Gregory Michael Gremillion

Dissertation submitted to the Faculty of the Graduate School of the
University of Maryland, College Park in partial fulfillment
of the requirements for the degree of
Doctor of Philosophy
2015

Advisory Committee:
Professor J. Sean Humbert, Chair/Advisor
Professor Inderjit Chopra
Professor David Akin
Professor Derek Paley
Professor Timothy Horiuchi

Acknowledgments

Firstly, I would like to thank my advisor Dr. Sean Humbert for picking me out of the blue to be a part of his truly interesting, exciting, and fun lab, for expertly securing ever-necessary funding for my research, and most of all honing my presenting skills and penchant for anal-retentive chart design and slide aesthetics.

Secondly, I would like to thank several organizations that aided this work, including US Army Research Laboratory, US Air Force Office of Scientific Research, L3 Communications, Centeye Inc., and most importantly the University of Maryland and the Department of Aerospace Engineering.

Thirdly, I would like to thank every past and present member of the AVL for every time you offered up your advice, expertise, effort, and occasionally beer money solely for my benefit. I would not have made it to this point, in both professional and personal contexts, without your immeasurable contributions.

To Joe "J-Co" Conroy, you taught me almost everything I know about how to be a grad student, and I hope I lived up to your example to some degree. I was proud to accept the torch you passed to me as de facto godfather of the AVL. Perhaps more importantly, I thank you for being instrumental in my better-late-than-never introduction to the wonderful world of booze and all that College Park has to offer in that realm. Oh Turtle.

To Badri "B-Pod" Ranganathan, thank you for being the most selfless person I know. I echo Joe's sentiments from his dissertation in saying that you are, without a doubt, the hardest working person I know. Thank you for being my philosophical

discussion buddy even when you had a mountain of work to do. When you're back home don't hesitate to send me plots to ask what color a line is, and I won't hesitate to include you in the founding of Seacrets, Chennai.

To Andrew "Slippy-Sloppy" Hyslop, thank you for being an ever-present source of inspiration to work hard, play hard, and imitate Australians. I could always count on you to be up for any activity at a moment's notice and to always call shotgun and share some Sonic on the way to Ocean City. You will be sorely missed during your time in the land of dikes and tulips, as much as I'm sure you miss your dear friend Bruce.

To Hector "Ectorrr" Escobar, thank you for the crucial help with getting the vehicle up and running. More so, thank you for being my truly fearless wingman and daring me to start conversations with pretty girls. I truly appreciate your positivity and willingness to say "yes" to life and hope it rubs off on me. Also, thank you for being my faithful disciple of the gospel of Austin. Hook 'em!

On an abstract note, thank you to coffee, beer, and science, for being nutritious, delicious, and not superstitious. Honorable mention goes to MATLAB, LabVIEW, Vicon™, LaTeX, and Pandora.

Finally, and most of all, thank you to my family. Mom, Dad, and Ang, I can never fully express my gratitude for how much you all have done to get me to this point, but I'm going to try. You really are **the best**.

Table of Contents

List of Tables

List of Figures

Nomenclature

u	Forward translational velocity		γ	Accelerometer azimuth angle
v	Lateral translational velocity		β	Accelerometer elevation angle
w	Heave translational velocity		$\boldsymbol{\zeta}^T$	Accelerometer orientation vector
p	Roll angular velocity		$\boldsymbol{\rho}^T$	Accelerometer parameter vector
q	Pitch angular velocity		$\boldsymbol{\mu}^T$	Linear parameter vector
r	Yaw angular velocity		$\boldsymbol{\xi}$	Acceleration time history vector
ϕ	Euler roll angle		$\boldsymbol{\nu}$	Accelerometer noise vector
θ	Euler pitch angle		σ_e	Standard estimate error
t	Time		ϵ_r	Position error fraction
k	Discrete index		λ_p	Peak output wavelength
I	Ocellar luminance (Section 2.1)		f_c	Complementary filter factor
$\dot{I}$	Ocellar luminance rate		$\boldsymbol{x}$	State vector
I'	Ocellar filtered luminance		$\hat{\boldsymbol{x}}$	State estimate vector
f	Luminance field		$\boldsymbol{x}_r$	State reference vector
∇f	Luminance gradient		$\boldsymbol{y}$	Output measurement vector
$\hat{e}$	Unit vector		$\boldsymbol{u}$	Control command vector
V	Voltage		$\boldsymbol{d}$	Disturbance state vector
R	Resistance		$\boldsymbol{n}$	Measurement noise vector
C	Capacitance (Section 3.1 only)		$\boldsymbol{x}_{accel}$	Acceleration state vector
ω_L	Low-pass cutoff frequency		$\boldsymbol{u}_r$	Control reference command vector
ω_H	High-pass cutoff frequency		$\boldsymbol{\delta}$	Control adaptation vector
ω_o	Unity gain frequency		A	Dynamic matrix
σ_{rel}^2	Relative variance		B	Control authority matrix
F_n	Partial F-ratio		C	Measurement matrix
s_n^2	Estimated fit error		G	Disturbance matrix
σ^2	Variance		M	Estimation matrix
$\bar{M}_p$	Mean peak response		K_o	Outer loop control gain matrix
$\bar{t}_s$	Mean settling time		K_i	Inner loop control gain matrix
O	Inertial origin		$S_o G$	Disturbance transfer function
O'	Moving body origin		$\bar{\sigma}$	Maximum singular value
P	Accelerometer origin			
$\boldsymbol{r}$	Accelerometer position vector		*Subscripts*	
$\boldsymbol{\omega}$	Angular velocity vector		i	Ocellus index (Section 2.1)
$\boldsymbol{a}$	Translational acceleration vector		OF	Optic flow
$\boldsymbol{v}$	Translational velocity vector		i	Accelerometer index (Section 2.2)
$\boldsymbol{\alpha}$	Angular acceleration vector		P/O	P with respect to O
$\boldsymbol{F}$	Force vector		P/O'	P with respect to O'
$\boldsymbol{\tau}$	Torque vector		O'/O	O' with respect to O
I	Inertia tensor (Section 2.2)		S	Series
z	Accelerometer output		F	Feedback
κ	Accelerometer gain		M, d	Manipulated with disturbance
b	Accelerometer bias		M, n	Manipulated with noise

Abbreviations

sUAS	Small unmanned aircraft systems
DOF	Degree-of-freedom
3-D	Three-dimensional
2-D	Two-dimensional
FOV	Field of view
UV	Ultraviolet
IR	Infrared
RGB	Red-green-blue
PA	Preferred axis
VLSI	Very-large-scale integration
MEMS	Microelectromechanical systems
IMU	Inertial measurement unit
GFINS	Gyro-free inertial navigation systems
LSB	Least significant bit
SNR	Signal-to-noise ratio
MSE	Mean squared error
MSE_{tr}	Transient mean squared error
MSE_{ss}	Steady-state mean squared error
PID	Proportional-integral-derivative
SISO	Single-input-single-output
MIMO	Multiple-input-multiple-output
HPF	High-pass filter
LPF	Low-pass filter
FAFB	Force-adaptive feedback

Chapter 1: Introduction

1.1 Motivation

Small unmanned aircraft systems (sUAS), typically characterized by extremely limited payloads, low mass and inertia, as well as rapid body dynamics, are especially challenging platforms to stabilize. Traditionally, sUAS stabilization is accomplished with a standard suite of sensors including accelerometers, gyroscopes, and magnetometers, [1] [2] [3] [4] [5]. These small-scale inertial measurement units are generally capable of providing sufficient measurements for estimating the vehicle orientation necessary for stabilizing feedback. However, these systems often have limited or no redundancy, and therefore provide minimal robustness to component failure and measurement noise. The digital feedback architecture of these sensing and control systems imposes inherent bandwidth limits. These systems also often have a significantly diminished measurement quality as they are scaled to micro-scale flight vehicles. The complex routines that may mitigate these detrimental characteristics are also not scalable due to processing limitations and bandwidth requirements of micro-scale flight. Furthermore, the low mass, inertia, and actuator authority of these small platforms often make them much more susceptible to gust disturbances.

Conversely, flying insects provide examples of robust stability and navigational abilities despite similar constraints on sensor payload, processing power, and loop closure speeds. They achieve this robustness through several means. The insect body is effectively a flying, multimodal sensor network. Information from visual, inertial, and tactile receptors are collected across networks distributed spatially across the entirety of the insect body. These measurements are fused to provide information about the state of the insect and its environment. This encoded information includes egomotion, aerodynamic disturbances, obstacle proximity, damage detection, proprioception, and numerous other sources of rich information. Insects are also characterized by highly redundant sensor networks. A highly redundant sensor architecture provides several advantages, foremost is the output of less noisy and more informative measurements. This redundancy also mitigates the effect of sensor damage or failure in the aggregate output information. Flying insects also do not close digital sensing, processing, and control loops. Rather, they have direct analog connection between their sensory systems and their flight motor neurons. This makes them capable of closing feedback control loops at extremely high speeds. This capability is paramount for both effective stabilization and gust rejection for flight at these small scales. These characteristics are the driving motivation for developing biologically inspired sensing and estimation strategies to achieve high performance stabilization and gust rejection in micro-air vehicles.

1.2 Ocellar Sensing

Most flying insects depend heavily on visual mechanisms to complement mechanosensory systems. The visual sensing modality provides some of the most useful measurements for performing both outer loop navigational tasks, such as obstacle avoidance, and inner loop stabilization tasks, such as disturbance rejection.

Many species of flying insects possess two visual systems, the compound eyes and the ocelli, or simple eyes, [6] [7]. The compound eye provides signals encoding measures of proximity to obstacles, relative velocity, and rotation rate, [8] [9]. Directionally selective cells analyze optic flow to estimate comparatively slow state changes [10], while ocelli measure changes in light intensity within the dorsal visual hemisphere correlated with fast attitude changes, [6].

In many species, the ocelli are arranged in a triangular pattern in the dorsal region of the head between the compound eyes. Typically a median ocellus is positioned in the midsagittal plane and the lateral ocelli are positioned to the left and right posterior of it. The retina of each ocellus is positioned several micrometers from the focal plane of the ocellar lens. Therefore, the ocelli act as wide-field luminance sensors, incapable of forming a focused image in most cases, [11] [12]. The medial ocelli in dragonflies have been shown to produce directionally selective responses to motion patterns, [13]. Despite this variability, the "single sensor hypothesis" as described by [14] and [15] is used as the guiding model for the ocellar function described in this work. The ocelli have large overlapping fields of view each of which encompasses nearly one third of the visible environment. Across species,

the wavelength of peak sensitivity varies to a large degree from ultraviolet to infrared, sometimes with bimodal spectral sensitivity distribution, [11] [16] [17]. The ocelli have a higher bandwidth light response, with bandpass characteristics, and a faster connection to the steering muscles of the flight motor than the compound eyes, [11] [16] [18] [19]. The ocelli have a latency significantly shorter than that of the compound eyes. The functional characteristics of the ocelli of several species suggest they are well suited to sensing rapid changes in the overall luminance of large portions of the visual environment. Luminance changes of this type are typically caused by rapid changes in attitude of the body, and thus the head, in an environment with asymmetric light intensity distributions, e.g. bright sky versus darker ground. The connectivity between the ocellar system and neural pathways providing the neck and flight motor suggest them to be involved in both gaze stabilization to keep the head aligned with the horizon and in maintaining a level flight attitude. This has been concluded based on electrophysiological and behavioral studies on blowfly [20] [21], dragonfly [22], wasps [23], and other flying insects [6].

Previous engineering implementations of ocelli-inspired flight stabilization have focused on attitude control of a sUAS. A simulation model of a *Drosophila*-inspired omnidirectional imager was implemented by [14]. Wide-field luminance and optic flow measurements were taken from this imager and compared to optimally derived weighting patterns to extract information about attitude and nearness to objects, respectively. Closed-loop control of the inner stabilization loop and outer navigation loop was demonstrated in simulation with respective measurements of luminance level and optic flow. Here the authors applied the matched filter method, typical

to optic flow state estimation, to the outputs of a simulated ocelli. Differential combinations of the luminance outputs of four photodiodes arranged in a pyramidal configuration were used by [24] to determine the direction of the brightest light source, approximating an attitude estimate. Using the same sensor, a method of attitude estimation was investigated by [25] using sinusoidal functions of intensity on the visual sphere. In [26], roll attitude was stabilized by balancing light intensities on right and left hemispheres of a simulated flight vehicle with nine receptor fields in an omnidirectional configuration. [27] demonstrated gaze stabilization of a camera tracking a fiducial point. In [28], near-omnidirectional imagery, from two digital cameras, was classified into regions of sky and ground and matched to pre-computed databases of attitude dependent image kernels to estimate the vehicle attitude. An attitude sensor based on the function of the dragonfly ocelli was developed for Mars surface exploration by [29]. An initial stage of UV and green sensitive photodiodes were combined antagonistically to form luminance values from the right, left, and forward positions of the vehicle. Differencing of these luminance measurements formed the estimate of roll and pitch angle. [30] developed an ocellar sensor with four pairs of UV and green filtered diodes, oriented along the lateral and frontal directions. The UV signal from each pair of photodiodes was normalized by the corresponding green signal to produce a spectral opponent signal. The opponent signals from the right and left pairs of diodes were combined differentially, to produce a feedback signal proportional to the roll attitude of the sensor body. Using this sensor, roll attitude tracking was demonstrated on a fixed-wing aircraft.

The work presented herein differs from these previous works in that it replicates

5

the function of the insect visual system to determine attitude *rate* information from ocelli and utilizes this information for vehicle stabilization with an analog ocellar sensor. To determine how a system with the functional properties of the ocelli might be utilized for stabilizing feedback, empirical simulation modeling of such a system was performed. This simulation allowed for determination of which vehicle motion states may be encoded in ocellar outputs.

1.3   Acceleration Sensing

Effective rejection of disturbance forces and torques requires high bandwidth sensing of these exogenous inputs before they propagate to lower order states of a flight vehicle. Traditionally, disturbance rejection has focused on sensing and feedback from pose and velocity estimates. Disturbances between the controller-issued commands and the plant state can be induced by gust disturbances, actuator failures, physical impacts with obstructions, and various other sources. Traditionally, stability control systems regulate the effect of these disturbances through feedback from estimation of lower order states, such as attitude or angular velocity. Furthermore, the estimation of these states is implemented with measurements from a minimal set of inertial sensors approximately collocated at the vehicle center of mass. By distributing sensors across the airframe, additional state information is encoded in the sensor measurements, and thus a more rich state estimate may be extracted from the measurements. Sensing with distributed arrays of redundant sensors yields improvements in signal-to-noise ratio even with relatively low quality

individual sensors components. Noise reduction is achieved by weighting across the all available measurements to produce an aggregate state estimate.

These sensor architecture characteristics are supported biologically in many insects, especially flying insects, where rapid sensation of a wide range of multimodal states is critical to effective flight. Insects are typified by distributed mechanosensory systems. As detailed by [31], mechanoreceptors in insects may be delineated into four functional categories: trichoid sensilla, campaniform sensilla, stretch receptors, and chordotonal organs. The fundamental function of each of these organs is respectively tactile and air movement sensing, proprioception and appendage orientation sensing, muscular position sensing, and vibration sensing. Chordotonal organs have various sensory functions across species of insects, but often are sensitive to acceleration [32]. These four types of mechanoreceptors form fundamental components, which when fused, can provide sensory information about complex physical states.

The halteres are an example of this type of sensory organ, and have been thoroughly studied from physiological, behavioral, and functional contexts [33] [34] [35] [36] [37]. These structures are small appendages, specifically vestigial hind wings, that beat out of phase with the wings. The halteres are typically thought of as biological analogues of a mechanical gyroscope, as they encode information about angular velocity, in the way that the ocelli encode this information in the visual modality. However, the mechanism by which flying insects sense angular rates via a halteres is fundamentally through sensation of forces. As an angular velocity is experienced by the insect body, a Coriolis force is induced on the flapping haltere. This force is sensed by strain sensitive mechanoreceptors, primarily campaniform

sensilla and chordotonal organs [31], thus encoding angular rate information. Angular accelerations are also encoded within the strains sensed at the haltere base. These angular acceleration dependent forces have the same direction and frequency as the Coriolis forces, but are 90° phase shifted and have a smaller magnitude [36]. This implies that the Coriolis and angular acceleration states may be separately extracted from measurements produced by the haltere mechanoreceptors. The halteres represent an example of spatially distributed mechanosensors that directly detect linear and rotational accelerations, from which corrective flight maneuvers are triggered [38] Similarly, hair-like mechanoreceptors exist in many species, invertebrate and vertebrate, that are sensitive to accelerations of the body [39]

Biologically inspired microelectromechanical system (MEMS) halteres have been developed by [40] and [41] capable of sensing linear and rotational forces. A method of sensing strains, that may encode force information, based on the campaniform sensilla was developed by [42] and [43] to be embedded in space structures. Acceleration sensors can detect such disturbance forces and torques before they propagate to lower order states, and therefore can act to reject those disturbances more rapidly when incorporated in feedback control. Incremental dynamic inversion has been shown in simulation by [44] and [45] to reject disturbance dynamics, given measurements of the acceleration states. Application of arrays of accelerometers in past works has focused on gyro-free angular *velocity* sensing and estimation, in so-called gyro-free inertial navigation systems (GFINS). Several examples of this have been demonstrated in simulation and hardware, [46] [47] [48] [49]. Apart from sensing angular velocities rather than accelerations, these past efforts differ from

the work presented here in that they implement a set of accelerometers precisely placed at key geometric locations and orientations, so as to provide angular velocity estimates with the minimum number of sensor measurements. Conversely, in this work, cues are taken from biology, implementing a highly redundant sensor set distributed at arbitrary locations and orientations. Here it is useful to harness the fact that the mapping from acceleration states to forces and torques is a linear function of static sensor parameters, including position and orientation. The development of an automatic calibration technique presented herein, allows for the biologically-inspired arbitrary placement of sensors while still producing accurate force and torque estimates by means of static estimation. Combined with an analog source of acceleration measurement, as might be provided by the cantilever structures in [42] and [43], the static estimation of body acceleration detailed in this work provides a framework for a fully analog implementation of force and torque sensing.

1.4   Multimodal Sensor Fusion

As stated previously, along with analog sensing and feedback mechanisms, multimodal sensor fusion is a key to the robust and complex behaviors seen in flying insects. The fusion of fully analog implementations of the two sensing modalities detailed in this work could provide the extremely robust and highly scalable stabilization and disturbance rejection characteristics needed for micro-scale flight in highly variable environments. This is made possible by the analog-implementable nature of these two sensing modalities, due to their static linear estimation mech-

9

anisms. Furthermore, these two sensing modalities could be fused with an analog implementation of wide-field integration of optic flow based on the insect visual system as detailed in [50] [51] [52]. Such as system would form a truly scalable, sensing and estimation architecture, capable of navigational control, flight stabilization, and disturbance rejection.

1.5   Thesis Contributions and Organization

The technical contributions from this work are listed below:

1. A model of the ocelli in flying insects and a method of static linear estimation of the pitch and roll rates from its outputs was developed.

2. A method for the static linear estimation of force and torque from a spatially distributed array of acceleration measurements was developed

3. A fully analog sensor was designed and fabricated to replicate the response of the ocellar visual system, producing static estimates of pitch and roll rate.

4. An array of arbitrarily placed linear accelerometers was constructed, static linear estimation of the acceleration states was implemented in hardware, and an automatic calibration algorithm was developed.

5. Stabilizing rate feedback from an analog ocellar sensor on a sUAS was demonstrated in the presence of disturbances.

6. Disturbance rejection was demonstrated on a sUAS with feedback from the spatially distributed accelerometer array.

Chapter 2 formulates the analytical framework and discusses the simulation modeling of both the ocelli and distributed acceleration sensing modalities. This section includes methods for performing static linear estimation on the raw sensor outputs to produces estimates of rotational velocity and 6-DOF accelerations, respectively. Chapter 3 details the design, fabrication, and characterization of both sensing modalities. Chapter 4 presents the methods for vehicle integration, control design, and closed loop control response results for a quadrotor sUAS in flight, subject to disturbance impulses. Chapter 5 draws conclusions from the work in total and outlines the technical contributions made. Chapter 6 outlines potential directions for future work that may expand on the topics discussed herein.

Chapter 2:   Modeling

Section 2.1.1 briefly details an analytical geometric model for rotational ego-motion sensing. Section 2.1.2 details the empirical simulation modeling of the ocelli in a cluttered 3-D environment and a method for static estimation of pitch and roll rates. Section 2.2.1 details the analytical framework for estimating forces and torques from spatially distributed acceleration measurements. The response of the distributed accelerometer array is characterized for various values of measurement noise a position error in Section 2.2.2.

2.1   Ocelli

2.1.1   Analytical Modeling

The functionality of ocelli in flying insects have been studied and speculated on from behavioral and physiological perspectives [6] [20] [21] [22]. As a part of the visual sensory system it is clear that they encode information about either the visual environment or state of the insect in flight. Due to their physiological properties, specifically their wide and disparate fields of view, defocused retinal image, and rapid response rate, it is often suggested that they provide information

about the rotational state of the insect. Such information is presumed to play a role in stabilization of the insect body or head as part of a flight motor or proprioceptive feedback mechanism.

Assuming this function within the insect visuomotor system we simplified analytical model of the response of the ocelli based on their geometric properties is used. This analytical model will provide a reference for a full 6-degree of freedom Monte Carlo simulation detailed in Section 2.1.2.

Given the primarily phasic response measured in ocellar electrophysiological studies when exposed to luminance stimuli, [16] [19] [21], we are interested in analytically expressing the luminance *rate*, that is the time rate of change of the luminance, $\dot{I}$ as a function of the body rates $\boldsymbol{\omega}$. For our simplified model of the ocelli, shown in Figure 2.1, we assume the environment luminance field f is projected onto a unit viewing sphere, centered at the origin of the ocellar body frame, with spatial gradient ∇f. It is defined that the ith ocellus has an arbitrary but fixed pointing direction in the body frame, indicated by the unit vector $\hat{\boldsymbol{e}}_i$. By inspection, the luminance rate for this i^{th} ocellus $\dot{I}_i$ is given by the following

$$\dot{I}_i = (\hat{\boldsymbol{e}}_i \times \nabla f) \cdot \boldsymbol{\omega} \tag{2.1}$$

The typical outdoor environment has a source of maximum luminance at the zenith, with a monotonically decreasing luminance field toward the zenith. It is assumed that the spatial gradient ∇f is constant and aligned with the longitudinal lines from the environment nadir to the zenith, and that the cross product between the
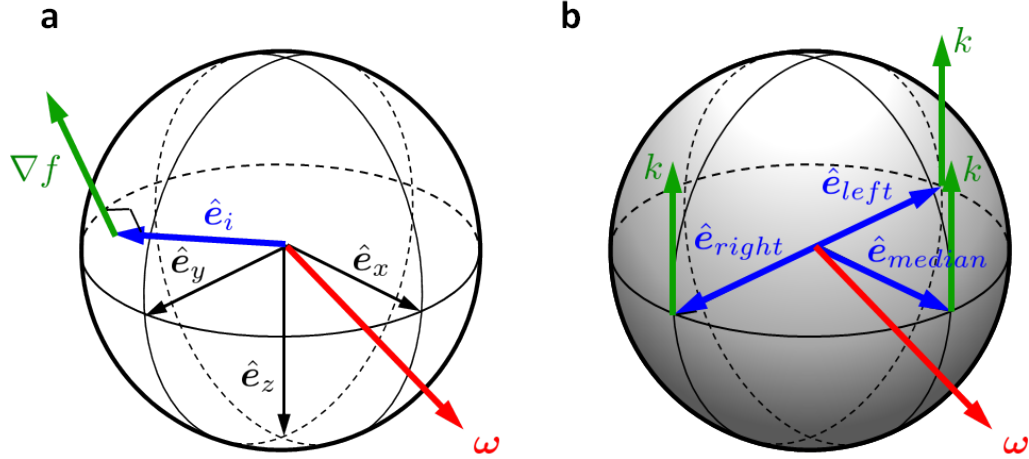
Figure 2.1: Analytical ocellar model geometry for (a) general case and (b) simplified case subject to assumptions (2.2), (2.3), and (2.4)

pointing direction $\hat{e}_i$ and the spatial gradient has constant magnitude across the entire field of view of a single ocellus.

$$||\nabla f|| \equiv k \tag{2.2}$$

$$(\hat{e}_i \times \nabla f) \cdot \begin{bmatrix} 0 & 0 & 1 \end{bmatrix}^T \equiv 0 \tag{2.3}$$

This second result produces invariance in the luminance rates to yaw rate r, which is intuitive as sensing rotations about the axis toward the luminance source would not be possible with this sensing mechanism. For three ocelli, aligned respectively with the body x-axis and $\pm y$-axis, i.e.

$$\hat{e}_{median} \equiv \begin{bmatrix} 1 & 0 & 0 \end{bmatrix}^T \tag{2.4}$$
$$\hat{e}_{right} = -\hat{e}_{left} \equiv \begin{bmatrix} 0 & 1 & 0 \end{bmatrix}^T$$

the measurement matrix relating the luminance rates to the body rates simplifies to

$$\boldsymbol{y} = k \begin{bmatrix} 0 & 1 \\ -1 & 0 \\ 1 & 0 \end{bmatrix} \begin{bmatrix} p \\ q \end{bmatrix} \equiv C\boldsymbol{x} \tag{2.5}$$

where

$$\boldsymbol{y} \equiv \begin{bmatrix} \dot{I}_{median} & \dot{I}_{right} & \dot{I}_{left} \end{bmatrix}^T \tag{2.6}$$

Applying the optimal linear least-squares static estimation to these outputs $\boldsymbol{y}$ yields estimates of the pitch rate and roll rate states

$$\hat{\boldsymbol{x}} = M\boldsymbol{y} \tag{2.7}$$

where the estimation matrix M is the inverse of C (2.5), or the pseudo-inverse for non-square C

$$M = (C^T C)^{-1} C^T \tag{2.8}$$

$$M = m \begin{bmatrix} 2 & 0 & 0 \\ 0 & -1 & 1 \end{bmatrix} \tag{2.9}$$

with $m = (2k)^{-1}$ [53] [54]. This result illustrates that rotational velocities p and q are linearly encoded in the outputs of the ocelli subject to the assumptions in (2.2), (2.3), and (2.4).

This provides a useful reference for the simulation modeling to follow. This simulation will demonstrate the stringency of the stated assumptions. It will also illustrate if any vehicle states, other than angular velocities, are encoded in the ocellar outputs and cannot be modeled with the above methods.

2.1.2   Simulation Modeling

Simulation modeling of the ocelli was performed to characterize their response to vehicle motions in a clutter 3D environment(Figure 2.4a-b). To this end, Monte Carlo simulation and system identification methods were used to empirically determine the contributions of the vehicle state to the outputs of the ocellar system. Although it is generally thought that ocelli encode only information about rotational motion states, [6] [20] [21] [22], this empirical modeling method allows for identification of contributions from translational states in the ocellar response as well.

2.1.2.1   Ocellus Bio-Inspired Simulation Model

To estimate a relationship between the kinematic states of the insect and the ocellar outputs, a simulation model of the ocelli was developed based on the functional operation of ocelli in flying insects. The simulation model for a single ocellus is shown schematically in Figure 2.4d, based on simulated cameras on a mobile airframe coordinate system as in Figure 2.4c. The stages of the model convert raw camera imagery to a normalized scalar filtered luminance, I', that is characteristical-

ly consistent with the response of ocelli descending neurons, as described in [11], [12], and [16]. The RGB imagery from a wide field of view camera ($115° \times 115°$) is converted to a grayscale image. A circular mask was applied to the rectangular camera image to crop out the image corners to match the biological field of view. The grayscale values at each pixel location within the entire image are summed to a single scalar intensity value, and normalized by the image size and maximum possible intensity, yielding ocellar luminance I. The normalization accounts for image size and range of possible intensities, producing a luminance $I = 1$ for an ocellus with its entire field of view maximally illuminated and luminance $I = 0$ for an entirely dark field of view. This luminance value is then high pass filtered by $G_{HPF}(s)$, approximating the time differentiation of the luminance signal, to produce filtered luminance I'. This high-pass filtering is supported in biological findings of the primarily phasic response of some ocellar pathways to luminance changes [16] [19] [21]. These filtered luminances are the final output of each of the three ocellar simulation models.

Using a 3-D simulation environment developed in the Autonomous Vehicle Laboratory at the University of Maryland, simulated sensor outputs were collected as the simulated flight vehicle underwent open-loop maneuvers. Figure 2.4a-c depicts the cluttered simulation environment and example camera frames indicating their orientation in the visual field. Figure 2.2 displays the right ocellar luminance I_{right} for several different flight paths through the simulated urban environment for the same predefined attitude egomotions at each time instant. In the presence of obstacles that distort the assumed luminance field f specified by (2.2) and (2.3),

such as buildings, vegetation, clouds, and textured surfaces, absolute detection of the zenith/horizon is corrupted. The large disparities in luminance output for a consistent attitude are predominantly at low frequencies and are due to translation through the anisotropic environment. By filtering out these low frequencies, the luminance rate approximation I' is much more consistent across these different flight paths, Figure 2.3. Therefore, the focus of further modeling and sensor design assumes a defined ocellar sensor output vector given by

$$\boldsymbol{y} \equiv \begin{bmatrix} I'_{median} & I'_{right} & I'_{left} \end{bmatrix}^T \tag{2.10}$$
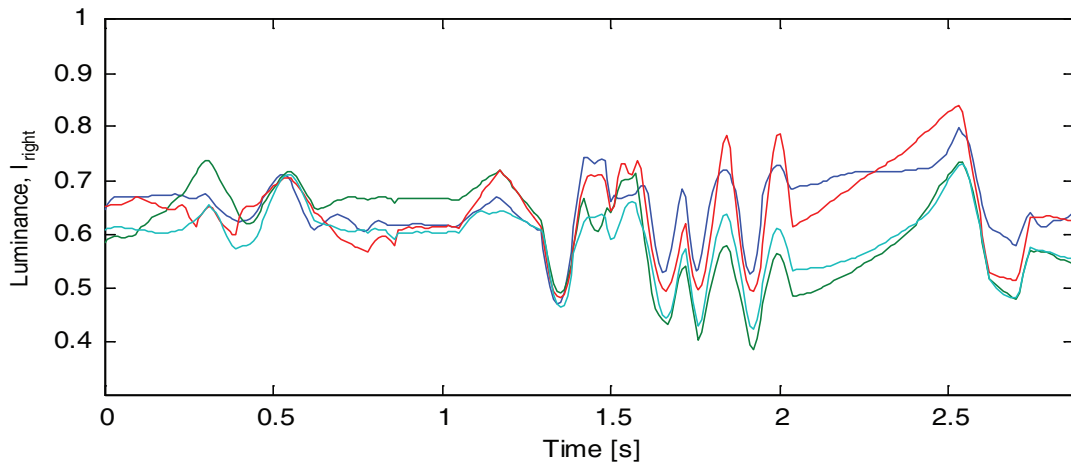
Figure 2.2: Right ocellar luminance I_{right} for various flight paths

18
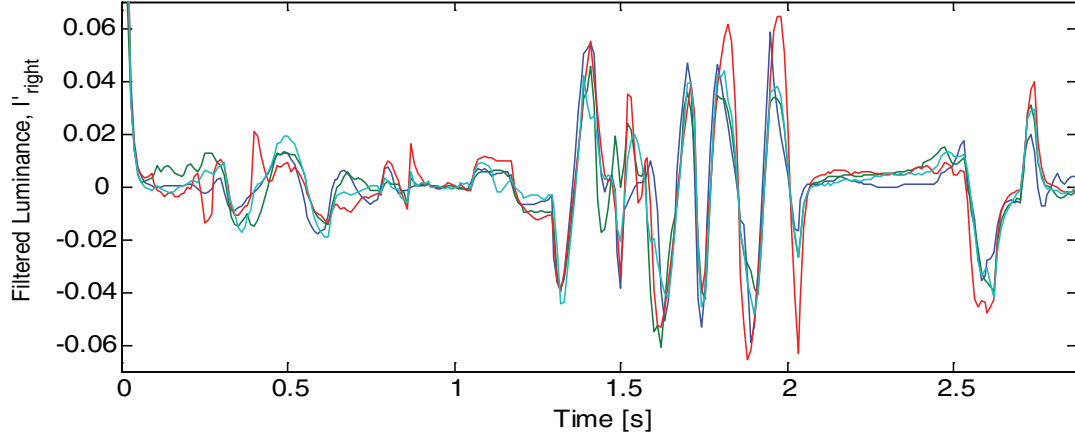
Figure 2.3: Filtered right ocellar luminance I'_{right} for various flight paths
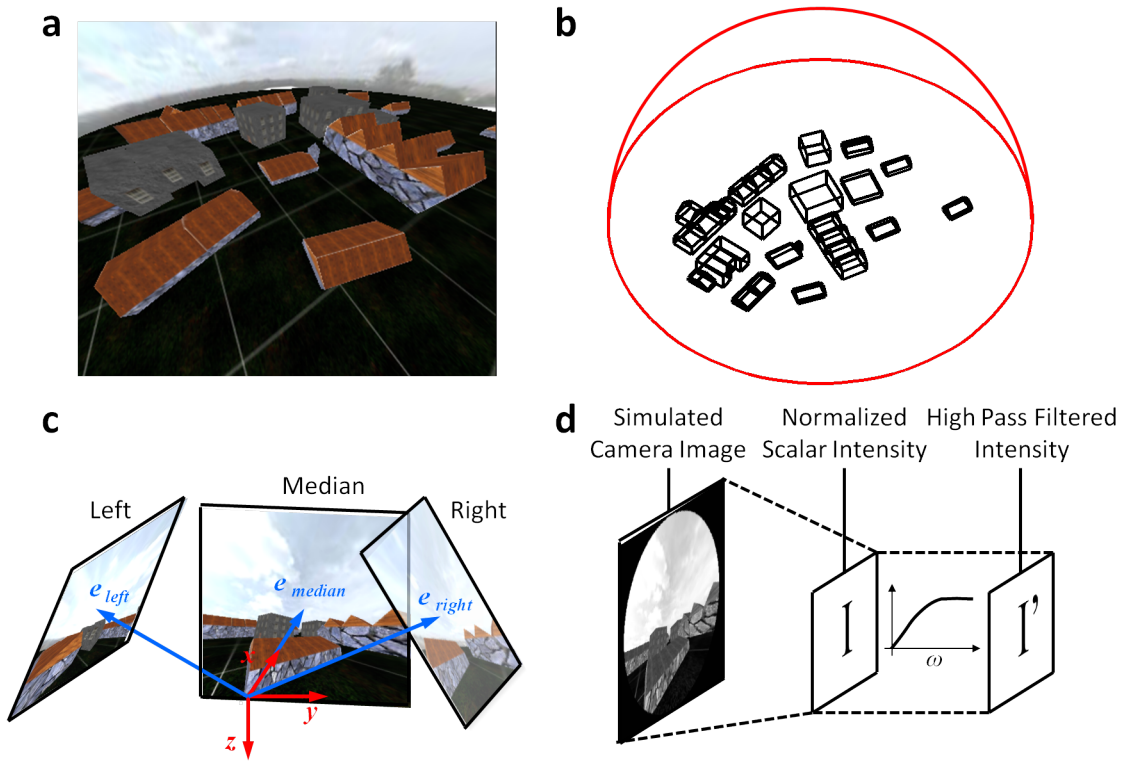
Figure 2.4: (a) Image of simulation environment, (b) layout of buildings (black) and hemispherical environment boundary (red), (c) ocelli sensor orientations with central axes (blue) and body-fixed coordinate system (red), and (d) ocellar simulation model

We seek to estimate a linear measurement matrix, C, that relates the kinematic

states $\boldsymbol{x}$ to the ocellar outputs $\boldsymbol{y}$ by

$$\boldsymbol{y} = C\boldsymbol{x}. \tag{2.11}$$

where

$$\boldsymbol{x} \equiv \begin{bmatrix} u & v & w & p & q & r & \phi & \theta \end{bmatrix}^T \tag{2.12}$$

with body-fixed forward, lateral, and heave velocities, u, v, and w; body-fixed roll, pitch, and yaw rates, p, q, and r; and roll and pitch Euler angles, ϕ and θ, respectively. While a more complex or analytical model relating states to outputs may be more accurate, this type of linear measurement model is useful in that it allows for application of static estimation and linear control techniques. Such a linear model is also easily implementable in analog circuitry, and thus highly scalable for micro-air vehicle applications.

2.1.2.2   Monte Carlo Modeling

The linear parameters that constitute C, which relate a state of $\boldsymbol{x}$ to an output of $\boldsymbol{y}$, were estimated using system identification techniques. Specifically, each state in $\boldsymbol{x}$ was independently excited with a unit amplitude sine function, meaning the sinusoidal maneuver occurred in only one of the states for each parameter identification. This was done to prevent coupling in the outputs of the ocelli that might occur when several states are excited simultaneously. An output prediction error

20

minimization method relating the jth state, x_j, to the ith ocellar output, y_i, was used to identify the parameter $c_{i,j}$ that produces the minimum output error e_{y_i} as defined in 2.13-2.14

$$\hat{y}_i = c_{i,j} x_j \tag{2.13}$$

where

$$e_{y_i} = |y_i - \hat{y}_i| \tag{2.14}$$

This approach allowed for identification of one-to-one linear relationships between each state and the three ocellar outputs. Using this methodology, of exciting a single state and estimating an optimal linear parameter relating the state to a single output, all 24 elements of the matrix, C can be determined. However, due to the non-isotropic characteristic of the cluttered simulation environment, it is necessary to perform this estimation across multiple locations and orientations within the environment. Therefore, to produce estimates of C that robustly encode state information in the outputs of the ocelli, a Monte-Carlo simulation technique was employed. A random set of 100 positions and heading orientations were generated throughout the hemispherical simulation environment, indicated in Figure 2.5. The single-state excitation and parameter estimation technique described previously was performed at each of these positions.

For each of the simulations, an optimal filter was calculated to best satisfy the relationship $I' \approx \dot{I}$ by performing an output error minimization between the true time derivative of the ocellar input luminance, $\dot{I}$, and the high-pass filtered
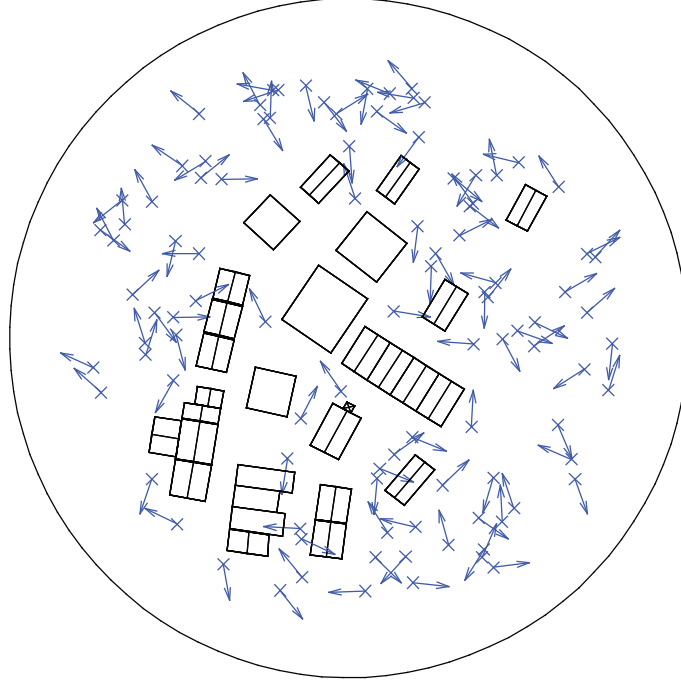
Figure 2.5: Diagram of Monte-Carlo simulation position/orientation

luminance, I'.

$$\bar{C} = \begin{bmatrix} 0.030 & 0.0029 & \mathbf{-0.24} & 0.045 & \mathbf{8.4} & 0.024 & -0.14 & -26 \\ -0.0002 & 0.017 & \mathbf{-0.23} & \mathbf{-8.2} & 0.099 & 0.020 & 28 & -0.56 \\ -0.0036 & -0.017 & \mathbf{-0.25} & \mathbf{8.4} & -0.016 & -0.066 & -26 & -0.23 \end{bmatrix} (2.15)$$

The mean value of each entry in C was taken across the 100 positions to form an averaged measurement matrix, $\bar{C}$ (2.15). This matrix suggests that there is throughput from every state to every output. However, by examining certain metrics of these parameter estimates, it it possible to discriminate those parameters that do not robustly relate states to outputs across the non-isotropic environment. Figure 2.6 displays the values of $c_{i,j}$ for each state-output relationship against all random simulation positions. The variation in scale of each plot is due to the variation in

22

output response magnitude for unit amplitude sinusoidal motions across all eight states. The values of the parameters associated with the states u, v, and r have a mean near zero and vary in sign from position to position. This implies, for example, that there is a deterministic *positive* relationship between u and the median ocellar output I'_{median} at one position within the environment and a deterministic *negative* relationship between them at another position. Therefore from Figure 2.6, it is clear that the states u, v, and r are not encoded robustly in the outputs of the ocelli in a cluttered environment, and their respective entries in the C matrix should be excluded based on variability across position. This may be quantified with a metric of relative variance, σ^2_{rel}

$$\sigma^2_{rel}(c_n) \equiv \frac{1}{N} \sum_{n=1}^{N} \left(\frac{c_n}{\bar{c}} - 1\right)^2, \tag{2.16}$$

where N=100. The values of $\sigma^2_{rel} > 1$ are thresholded, eliminating these three states, u, v and r.

$$R = \begin{bmatrix} 3.3 & 250 & \mathbf{0.25} & \mathbf{0.0090} & \mathbf{0.0044} & 690 & \mathbf{0.038} & \mathbf{0.0045} \\ 26000 & 7.4 & \mathbf{0.22} & \mathbf{0.0068} & 19 & 1500 & \mathbf{0.0088} & 5.8 \\ 180 & 7.0 & \mathbf{0.24} & \mathbf{0.0082} & 650 & 130 & \mathbf{0.0089} & 33 \end{bmatrix} \tag{2.17}$$

The matrix R, (2.17), presents the values for σ^2_{rel} for all elements of $\bar{C}$, with acceptable entries shown in bold.

The goodness of fit of the parameters associated with the remaining states, w, p, q, ϕ, and θ, can be tested using the partial F-ratio (2.18). This quantifies
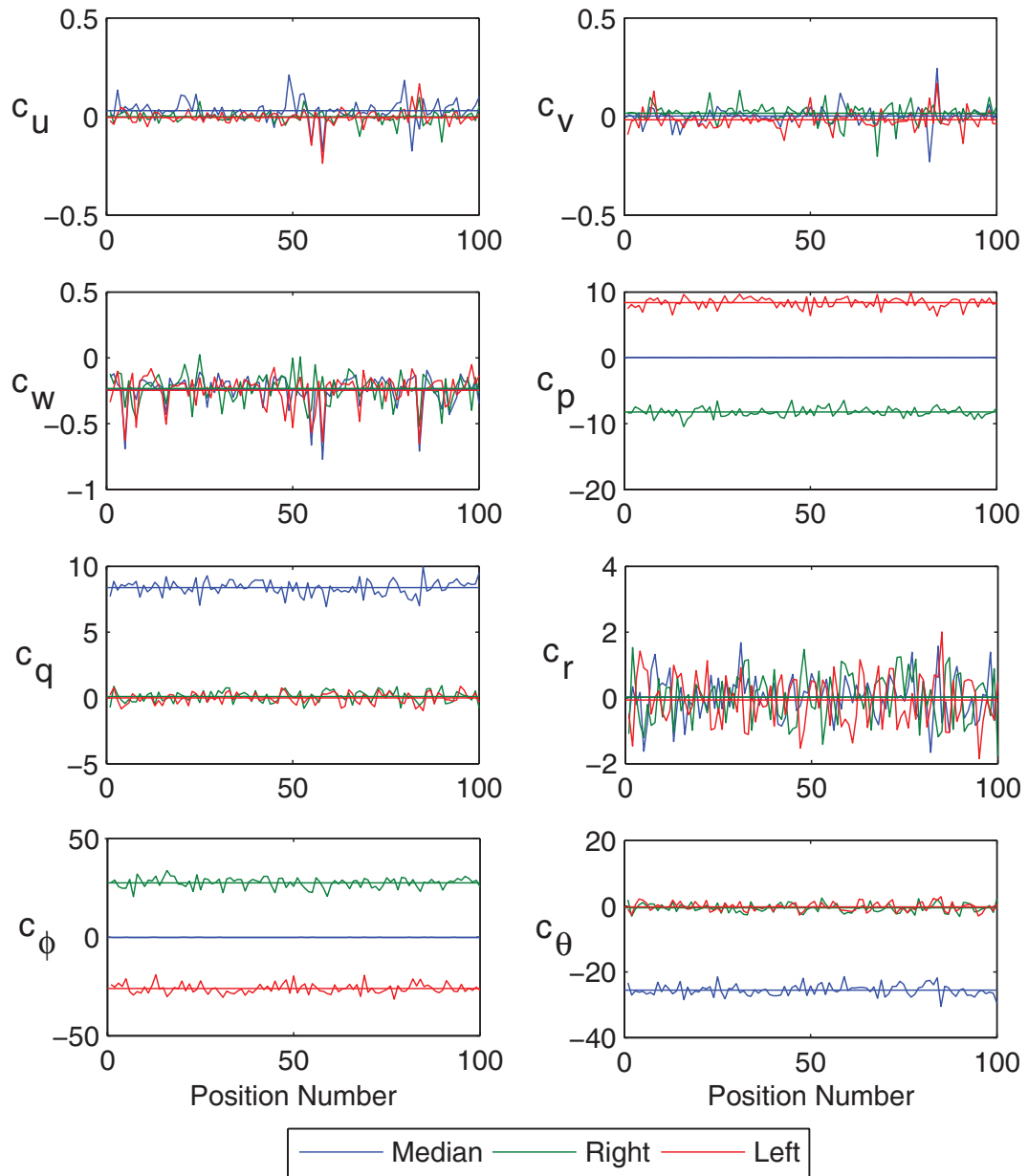
Figure 2.6: Measurement model parameter values for each state-output pair across all random positions (mean value indicated with horizontal line)

the degree to which the estimated output $\hat{y}_n$ agrees with the true output y_n, where

$$\hat{y}_n = c_n x_n.$$

$$F_n = \frac{c_n^2}{s_n^2}, \tag{2.18}$$

with the estimated fit error, s_n^2, given by

$$s_n^2 = \frac{1}{T} \int_0^T [y_n(t) - \hat{y}_n(t)]^2 dt, \tag{2.19}$$

for a simulation of duration T. Despite having low relative variance, the partial F-ratios for the parameter estimates associated with attitude states ϕ and θ were very low. This means the estimated outputs, $\hat{I}'$, resulting from the identified parameters c_ϕ and c_θ, do not correlate with the corresponding true outputs, I', for a given simulation. Parameters with a corresponding $F_n < 1$ were eliminated from the measurement model. The matrix P, (2.20), presents the values for F_n for all elements of $\bar{C}$, with acceptable entries shown in bold.

$$P = \begin{bmatrix} \mathbf{430} & \mathbf{610} & \mathbf{1300} & \mathbf{360} & \mathbf{1500} & \mathbf{140} & 0.46 & 0.49 \\ \mathbf{760} & \mathbf{690} & \mathbf{1200} & \mathbf{420} & \mathbf{6.3} & \mathbf{180} & 0.51 & 0.074 \\ \mathbf{750} & \mathbf{630} & \mathbf{1100} & \mathbf{700} & \mathbf{3.5} & \mathbf{220} & 0.48 & 0.056 \end{bmatrix} \tag{2.20}$$

Applying the metrics in (2.16) and (2.18) suggests that only the roll rate, p, pitch rate, q, and to a lesser degree, heave rate, w, are robustly encoded in the ocellar outputs. The bolded elements in (2.15) indicate parameters that satisfy these metrics. This supports the assertion that pitch and roll rotation rates are encoded by the varying luminance input to the ocelli. However, the empirical estimation tech-

nique used has shown that it is possible for ocellar outputs to encode translational state information, in the form of heave velocity, w. The methodology described above allows us to state that a sensor that functions similarly to the ocelli of several species of flying insects, as in Figure 2.4d, can only encode a linear relationship to the states w, p, and q in a cluttered environment.

The parameters relating p with I'_{right}, and I'_{left} are then constrained to be equal and opposite. The assumption implicit in this constraint is that maneuvers resulting in symmetrical changes in the orientation of respective ocellar visual fields should yield symmetrical ocellar outputs. The components relating to heave velocity, w, are omitted as they require large magnitude heave velocity excitations to elicit ocellar responses comparable to pitch and roll motions. This yields the final measurement matrix C for three ocellar outputs (2.21),

$$
C = \begin{bmatrix} 0 & 8.34 \\ -8.33 & 0 \\ 8.33 & 0 \end{bmatrix}.
\tag{2.21}
$$

The static estimation needed to reconstruct the desired state estimates $\hat{p}$ and $\hat{q}$ from the ocellar filtered luminances, I', can be calculated by inverting (2.21). Since the C matrix is non-square, a pseudo inverse is used to determine the estimation matrix M (2.22),

$$
\hat{\boldsymbol{x}} = M\boldsymbol{y} = (C^T C)^{-1} C^T \boldsymbol{y},
\tag{2.22}
$$

where $\hat{\boldsymbol{x}} = [\hat{p} \ \hat{q}]^T$ and $\boldsymbol{y} = [I'_{median} \ I'_{right} \ I'_{left}]^T$. This pseudo inverse calculation

26

yields the final estimation matrix M (2.23). This is the linear least squares estimator [53] [54]. Applying this linear combination to the three ocellar outputs of a sensor similar to the simulation model will produce estimates of the body-fixed pitch and roll rate states. Therefore, this simple estimator can provide useful feedback information and is implementable in analog circuitry.

$$M = \begin{bmatrix} 0.12 & 0 & 0 \\ 0 & -0.060 & 0.060 \end{bmatrix}. \tag{2.23}$$

The parameter values identified in (2.21) and (2.23) are influenced by specific factors of the simulation. For example contrast between the sky and ground of the simulated environment directly affects the magnitude of the filtered luminance I' in response to a given state motion. Therefore, the most useful characteristics taken from simulation modeling are the relative magnitudes the parameters in C and M. Thus these quantities may be more simply represented as

$$C = k \begin{bmatrix} 1 & 0 \\ 0 & -1 \\ 0 & 1 \end{bmatrix}. \tag{2.24}$$

and

$$M = m \begin{bmatrix} 2 & 0 & 0 \\ 0 & -1 & 1 \end{bmatrix}. \tag{2.25}$$

27

where $m = (2k)^{-1}$. This corresponds to the analytical findings in (2.5). The relation in (2.25) is used to guide the design of a hardware ocellar sensor, described in Section 3.1.

Using a bio-inspired ocellar model, in conjunction with system identification and Monte Carlo simulation techniques, it was shown that ocelli can robustly encode body rate and heave velocity states throughout a cluttered 3-D environment. Furthermore, a simple linear combination of the ocellar outputs can be used to extract estimates of the body-fixed rotation rate states.

2.2   Distributed Acceleration

2.2.1   Analytical Modeling

2.2.1.1   Force and Torque Model

For a moving body as shown in Figure 2.7 with body-fixed coordinate system O', the position of body O' with respect to the inertially-fixed frame O is defined as $\boldsymbol{r}_{O'/O}$, where the notation of [55] is used. The center of mass of body O' has translational acceleration $\boldsymbol{a}$. The body has angular velocity $\boldsymbol{\omega}$ and angular acceleration $\boldsymbol{\alpha}$. The total force, $\boldsymbol{F}$, and torque, $\boldsymbol{\tau}$, applied to the rigid body are functions of mass, m, and inertia, I, as well as the previously defined motion states as

$$\boldsymbol{F} = m\boldsymbol{a}$$
$$\boldsymbol{\tau} = I\boldsymbol{\alpha} + \boldsymbol{\omega} \times I\boldsymbol{\omega} = I\frac{d}{dt}(\boldsymbol{\omega}) + \boldsymbol{\omega} \times I\boldsymbol{\omega}$$

(2.26)
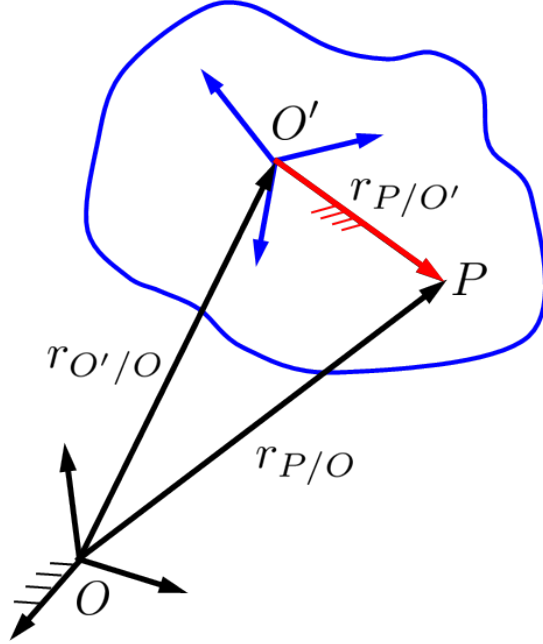
Figure 2.7: Diagram of body O' in motion with respect to inertial frame O. P is a point rigidly fixed to the body and offset from the body-fixed coordinate frame O' by constant position vector $\boldsymbol{r}_{P/O'}$

where the following quantities are expressed in the body-fixed frame

$$\boldsymbol{F} = \begin{bmatrix} F_x \\ F_y \\ F_z \end{bmatrix}, \boldsymbol{\tau} = \begin{bmatrix} \tau_x \\ \tau_y \\ \tau_z \end{bmatrix}, \boldsymbol{a} = \begin{bmatrix} a_x \\ a_y \\ a_z \end{bmatrix}, \boldsymbol{\alpha} = \begin{bmatrix} \dot{p} \\ \dot{q} \\ \dot{r} \end{bmatrix}, \text{ and } \boldsymbol{\omega} = \begin{bmatrix} p \\ q \\ r \end{bmatrix} \quad (2.27)$$

and the inertia tensor is

$$I = \begin{bmatrix} I_x & -I_{xy} & -I_{xz} \\ -I_{yx} & I_y & -I_{yz} \\ -I_{zx} & -I_{zy} & I_z \end{bmatrix} \quad (2.28)$$

The force-torque vector is related linearly by matrix E to the state vector $\boldsymbol{x}_{accel}$ via

$$\begin{bmatrix} \boldsymbol{F} \\ \boldsymbol{\tau} \end{bmatrix} = E\boldsymbol{x}_{accel} \tag{2.29}$$

where the defined state vector $\boldsymbol{x}_{accel}$, as a function of $\boldsymbol{a}$, $\boldsymbol{\alpha}$, and $\boldsymbol{\omega}$, is

$$\boldsymbol{x}_{accel} \equiv \begin{bmatrix} a_x & a_y & a_z & \dot{p} & \dot{q} & \dot{r} & p^2 & q^2 & r^2 & pq & pr & qr \end{bmatrix}^T \tag{2.30}$$

The matrix $E = f(m, I)$ is a linear function of mass, m, and inertia, I.

$$E = \begin{bmatrix} m & 0 & 0 & 0 & 0 & 0 & 0 & 0 & 0 & 0 & 0 & 0 \\ 0 & m & 0 & 0 & 0 & 0 & 0 & 0 & 0 & 0 & 0 & 0 \\ 0 & 0 & m & 0 & 0 & 0 & 0 & 0 & 0 & 0 & 0 & 0 \\ 0 & 0 & 0 & I_x & -I_{xy} & -I_{xz} & 0 & -I_{zy} & I_{yz} & -I_{zx} & I_{yx} & (I_z - I_y) \\ 0 & 0 & 0 & -I_{yx} & I_y & -I_{yz} & I_{zx} & 0 & -I_{xz} & I_{zy} & (I_x - I_z) & -I_{xy} \\ 0 & 0 & 0 & -I_{zx} & -I_{zy} & I_z & -I_{yx} & I_{xy} & 0 & (I_y - I_x) & -I_{yz} & I_{xz} \end{bmatrix} \tag{2.31}$$

An approximate CAD model was created (Figure 2.8), with each included component having a mass assigned as measured from the actual component. From this

30
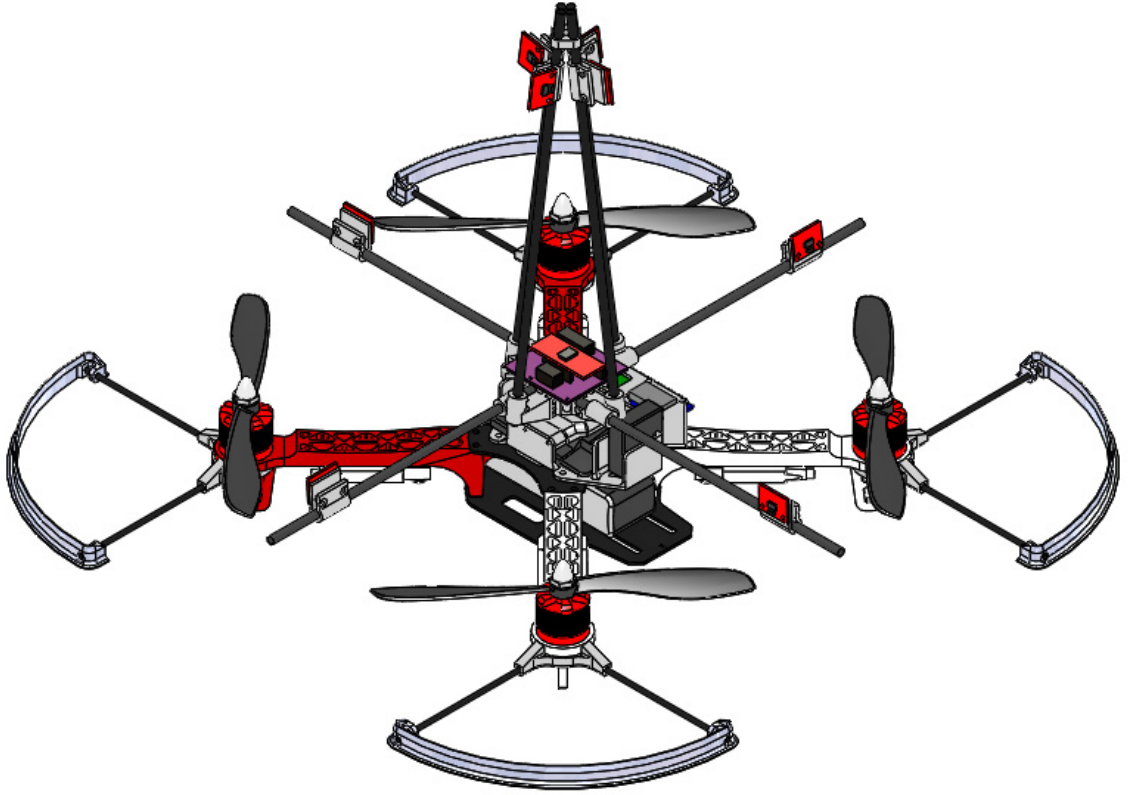
Figure 2.8: CAD model of quadrotor vehicle with distributed accelerometer array

model an estimated inertia tensor was calculated as

$$I = \begin{bmatrix} 2984.3 & -1.915 & -0.180 \\ -1.915 & 3794.8 & -11.751 \\ -0.180 & -11.751 & 2987.0 \end{bmatrix} \times 10^{-6} \text{ kg m}^2 \qquad (2.32)$$

which may be approximated as

$$I \approx \begin{bmatrix} I_o & 0 & 0 \\ 0 & 1.27I_o & 0 \\ 0 & 0 & I_o \end{bmatrix} \text{ with } I_o \approx 2985 \text{ kg m}^2 \qquad (2.33)$$

This simplifies the matrix E (2.31) to yield

$$E \approx \begin{bmatrix} m & 0 & 0 & 0 & 0 & 0 & 0 & 0 & 0 & 0 & 0 & 0 \\ 0 & m & 0 & 0 & 0 & 0 & 0 & 0 & 0 & 0 & 0 & 0 \\ 0 & 0 & m & 0 & 0 & 0 & 0 & 0 & 0 & 0 & 0 & 0 \\ 0 & 0 & 0 & I_o & 0 & 0 & 0 & 0 & 0 & 0 & 0 & -0.27I_o \\ 0 & 0 & 0 & 0 & 1.27I_o & 0 & 0 & 0 & 0 & 0 & 0 & 0 \\ 0 & 0 & 0 & 0 & 0 & I_o & 0 & 0 & 0 & 0.27I_o & 0 & 0 \end{bmatrix} \qquad (2.34)$$

2.2.1.2 Acceleration Estimation

For the point P (Figure 2.7) , displaced relative to the center of mass of O' by vector $\boldsymbol{r}_{P/O'}$, the acceleration with respect to the inertial frame O is given by

$$\boldsymbol{a}_{P/O} = \boldsymbol{a}_{O'/O} + \boldsymbol{a}_{P/O'} + \boldsymbol{\alpha} \times \boldsymbol{r}_{P/O'} + 2\boldsymbol{\omega} \times \boldsymbol{v}_{P/O'} + \boldsymbol{\omega} \times (\boldsymbol{\omega} \times \boldsymbol{r}_{P/O'}) \qquad (2.35)$$

where $\boldsymbol{a}_{O'/O}$ is the translational acceleration of the moving frame origin O' with respect to O, $\boldsymbol{a}_{P/O'}$ is the translational acceleration of P with respect to O', $\boldsymbol{\alpha} \times \boldsymbol{r}_{P/O'}$ is the Euler acceleration of body O', $2\boldsymbol{\omega} \times \boldsymbol{v}_{P/O'}$ is the Coriolis acceleration of O',

and $\boldsymbol{\omega} \times (\boldsymbol{\omega} \times \boldsymbol{r}_{P/O'})$ is the centripetal acceleration of O' (Figure 2.7). For the case that point P is rigidly positioned with respect to O', the vector $\boldsymbol{r}_{P/O'}$ is constant when expressed in the body-fixed frame, implying that

$$\boldsymbol{v}_{P/O'} = \frac{d}{dt}\left(\boldsymbol{r}_{P/O'}\right) = 0 \tag{2.36}$$

and

$$\boldsymbol{a}_{P/O'} = \frac{d}{dt}\left(\boldsymbol{v}_{P/O'}\right) = 0 \tag{2.37}$$

This yields the simplification of (2.39),

$$\boldsymbol{a}_{P/O} = \boldsymbol{a}_{O'/O} + \boldsymbol{\alpha} \times \boldsymbol{r}_{P/O'} + \boldsymbol{\omega} \times (\boldsymbol{\omega} \times \boldsymbol{r}_{P/O'}) \tag{2.38}$$

which reduces (2.39) from a differential equation in $\boldsymbol{r}_{P/O'}$ to a linear function of the constant $\boldsymbol{r}_{P/O'}$.

Now considering n such points, positioned rigidly with respect to the body center of mass by vector $\boldsymbol{r}_i$, where $i = 1, ..., n$, the acceleration, $\boldsymbol{a}_i$, experienced at the ith point is

$$\boldsymbol{a}_i = \boldsymbol{a} + \boldsymbol{\alpha} \times \boldsymbol{r}_i + \boldsymbol{\omega} \times (\boldsymbol{\omega} \times \boldsymbol{r}_i), \tag{2.39}$$

with body-fixed position vector

$$\boldsymbol{r}_i = \begin{bmatrix} x_i \\ y_i \\ z_i \end{bmatrix} \tag{2.40}$$

33

where $\boldsymbol{\alpha} \times \boldsymbol{r}_i$ is the Euler acceleration, and $\boldsymbol{\omega} \times (\boldsymbol{\omega} \times \boldsymbol{r}_i)$ is the centripetal acceleration of the rigid body. For notational simplicity the subscript references to the frames O, O', and P have been omitted. Furthermore, the acceleration, $\boldsymbol{a}_i$ (2.39), is related to the defined state vector, $\boldsymbol{x}_{accel}$ (2.30), by the matrix $H_i = f(\boldsymbol{r}_i)$, which is a linear function of $\boldsymbol{r}_i$, expressed in the body frame as

$$\boldsymbol{a}_i = H_i \boldsymbol{x}_{accel} \tag{2.41}$$

where

$$H_i = \begin{bmatrix} 1 & 0 & 0 & 0 & z_i & -y_i & 0 & -x_i & -x_i & y_i & z_i & 0 \\ 0 & 1 & 0 & -z_i & 0 & x_i & -y_i & 0 & -y_i & x_i & 0 & z_i \\ 0 & 0 & 1 & y_i & -x_i & 0 & -z_i & -z_i & 0 & 0 & x_i & y_i \end{bmatrix} \tag{2.42}$$

The ith triaxial accelerometer affixed rigidly to the moving body, aligned with the body fixed coordinate system, would produce outputs proportional to $\boldsymbol{a}_i$. Correspondingly, the ith *uniaxial* accelerometer affixed rigidly to the vehicle airframe, located at position $\boldsymbol{r}_i$, will produce measurement z_i related to $\boldsymbol{a}_i$ as

$$z_i = \kappa_i \boldsymbol{\zeta}_i^T \boldsymbol{a}_i + b_i \tag{2.43}$$

with constant gain, κ_i, bias, b_i, and orientation vector, $\boldsymbol{\zeta}_i^T$. The orientation vector represents the scalar projection of $\boldsymbol{a}_i$ onto the sensitivity axis of the uniaxial accelerometer, which may be arbitrarily oriented with respect to the body-fixed co-

ordinate frame and can be expressed by azimuth and elevation angles, γ_i and β_i, with respect to the body x-axis by

$$\boldsymbol{\zeta}_i^T \equiv \left[\begin{array}{ccc} \cos \gamma_i \cos \beta_i & \sin \gamma_i \cos \beta_i & -\sin \beta_i \end{array} \right] \tag{2.44}$$

Therefore, seven constant characteristic parameters, $\boldsymbol{\rho}_i \equiv \left[\begin{array}{ccccccc} \kappa_i & b_i & \gamma_i & \beta_i & x_i & y_i & z_i \end{array} \right]$, completely characterize the relationship between $\boldsymbol{x}_{accel}$ and z_i

$$z_i = \kappa_i \boldsymbol{\zeta}_i^T H_i \boldsymbol{x}_{accel} + b_i = \boldsymbol{c}_i^T \boldsymbol{x}_{accel} + b_i \tag{2.45}$$

where

$$\boldsymbol{c}_i^T \equiv \kappa_i \boldsymbol{\zeta}_i^T H_i = f(\boldsymbol{\rho}_i) \tag{2.46}$$

For n such uniaxial accelerometers distributed at distinct positions and orientations on the rigid airframe, the measurement vector $\boldsymbol{z}$ is

$$\boldsymbol{z} = \begin{bmatrix} z_1 \\ z_2 \\ \vdots \\ z_n \end{bmatrix} = \begin{bmatrix} \boldsymbol{c}_1^T \\ \boldsymbol{c}_2^T \\ \vdots \\ \boldsymbol{c}_n^T \end{bmatrix} \boldsymbol{x}_{accel} + \begin{bmatrix} b_1 \\ b_2 \\ \vdots \\ b_n \end{bmatrix} = C\boldsymbol{x}_{accel} + \boldsymbol{b} \tag{2.47}$$

Defining the unbiased measurement vector, $\boldsymbol{y}$, as

$$\boldsymbol{y} \equiv \boldsymbol{z} - \boldsymbol{b} \tag{2.48}$$

35

yields the relationship

$$\boldsymbol{y} = C\boldsymbol{x}_{accel} \tag{2.49}$$

where the matrix $C = f(\boldsymbol{\rho})$ is of dimension $n \times 12$. Using the pseudo-inverse of C, denoted as M, the static state estimate is

$$\hat{\boldsymbol{x}}_{accel} = M\boldsymbol{y} = (C^T C)^{-1} C^T \boldsymbol{y} \tag{2.50}$$

from the n-dimensional unbiased measurement vector and knowledge of the characteristic parameters of all n accelerometers. This is the linear least squares estimator [53] [54]. To calculate this pseudo-inverse it is required that the quantity $(C^T C)$ be invertible, and thus it is required that $n \geq 12$. Applying the static linear mapping E from (2.29) to this state estimate then yields an estimate of the force-torque vector as

$$\begin{bmatrix} \hat{\boldsymbol{F}} \\ \\ \hat{\boldsymbol{\tau}} \end{bmatrix} = E\hat{\boldsymbol{x}}_{accel} = EM\boldsymbol{y} \tag{2.51}$$

Thus with known physical properties of a vehicle and measurements from n distributed accelerometers, the total forces and torques applied to the vehicle can be directly, statically estimated.

2.2.2 Simulation Modeling

Based on the analytical modeling of the array of accelerometers in Section 2.2.1 a simulation model is formed. Open loop motions in all 6 degrees of freedom are generated for a simulated flight vehicle. Sensor position and orientations, $\boldsymbol{r}_i$ and $\boldsymbol{\zeta}_i^T$, are defined by the user, and may be deterministically or randomly generated. Based on these parameters and prescribed vehicle motions, simulated sensor outputs, $\boldsymbol{y}$, are generated based on (2.49). Static offset errors, $\boldsymbol{\Delta r}_i$ are added to the position vectors $\boldsymbol{r}_i$ in the calculation of H_i, from which C is derived (2.45), as

$$\tilde{H}_i = f(\tilde{\boldsymbol{r}}_i) = f(\boldsymbol{r}_i + \boldsymbol{\Delta r}_i) \tag{2.52}$$

Gaussian noise, $\boldsymbol{\nu}$, is also added to the analytically calculated sensor outputs as

$$\tilde{\boldsymbol{y}} = \boldsymbol{y} + \boldsymbol{\nu} \tag{2.53}$$

Using this simulation model the translational and angular acceleration estimates are compared for various cases of sensor noise, $\boldsymbol{\nu}$, position error, $\boldsymbol{\Delta r}$, and sensor array size, n. Figure 2.9 depicts such a comparative plot for the actual and estimated roll angular acceleration, $\dot{p}$, for the simulated sensor array. Comparing Figures 2.9a-b it is clear that for a *nearly* minimum array size ($n = 14$) increasing noise $\boldsymbol{\nu}$ so as to decrease the signal-to-noise ratio (SNR) magnitude from 50 to 5 results in a significant increase in estimate noise. Figure 2.9c illustrates that for

the same level of noise $\boldsymbol{\nu}$ (SNR=5), increasing the number of sensor measurements from 14 to 36 reduces the estimate noise to approximately the same levels seen in Figure 2.9a. Figure 2.9d depicts the effect of adding an error, $\boldsymbol{\Delta r}$, with a maximum magnitude that is 10% of the maximum magnitude of the sensor position vectors $\boldsymbol{r}$, that is $||\boldsymbol{\Delta r}||_\infty = 0.1||\boldsymbol{r}||_\infty$.
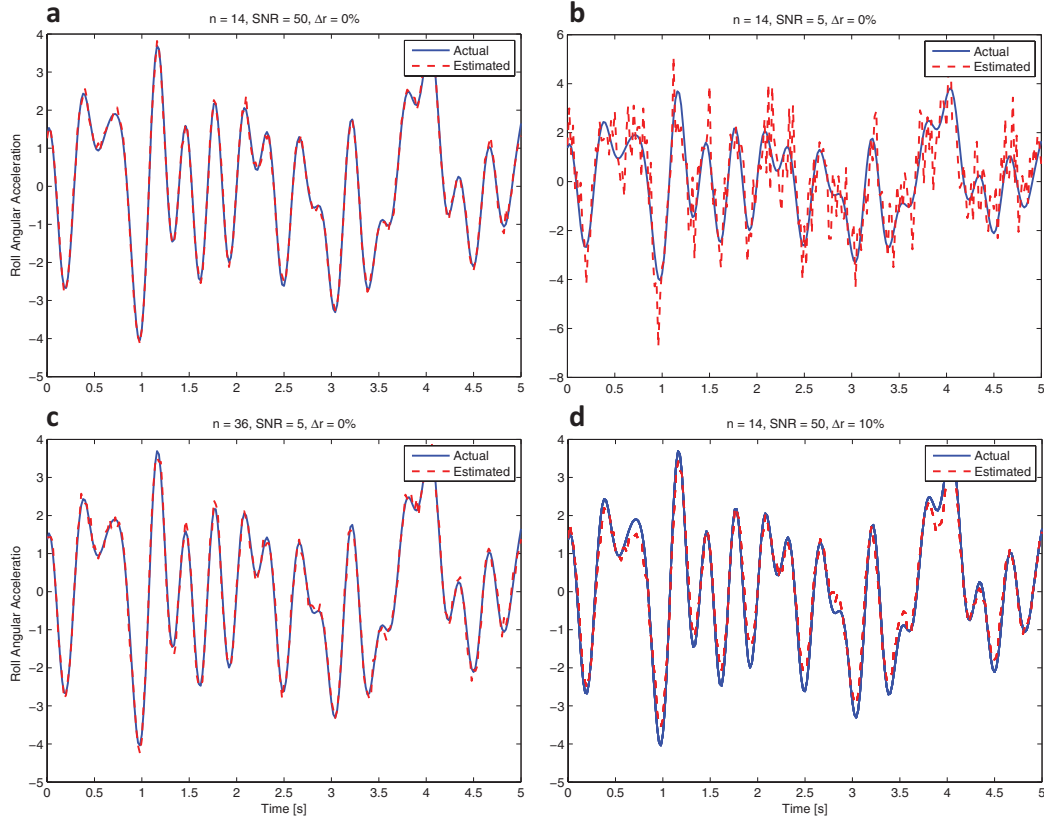
Figure 2.9: Comparison plot of actual and estimated roll angular acceleration, $\dot{p}$: (a) Estimate for sensor array with n=14 measurements, SNR=50 (magnitude), and (b) SNR=5, a significant increase in measurement noise $\boldsymbol{\nu}$, and (c) the same noise level (SNR=5), with nearly triple the number of measurements (n=36); (d) Estimate with the same conditions as (a), but with sensor position error $||\boldsymbol{\Delta r}||_\infty = 0.1||\boldsymbol{r}||_\infty$

Similar simulations were generated for various values of array size n and sensor noise $\boldsymbol{\nu}$. To quantify the accuracy of the simulated state estimates, $\hat{\boldsymbol{x}}_{accel}$, the

standard estimate error, σ_e, is used and is defined as the standard deviation of the estimate error, represented as the discretely sampled signal of length K, $\boldsymbol{e}[k] \equiv \hat{\boldsymbol{x}}_{accel}[k] - \hat{\boldsymbol{x}}_{accel}[k]$.

$$\sigma_e = \left(\frac{1}{K-1} \sum_{k=1}^{K} \left(\boldsymbol{e}[k] \right)^2 \right)^{1/2} \tag{2.54}$$

This metric of estimate accuracy is plotted in Figure 2.10 for values of n from 14 to 36 and sensor output SNR magnitude from 10 to 2. Figure 2.10a illustrates the observation, quantitatively, that increases in SNR or sensor number n result in decreases in estimate error, and thus a more accurate estimate of the states $\boldsymbol{x}_{accel}$. This trend was seen qualitatively in Figures 2.9a-c. Figure 2.10b depicts a 2-D contour plot of the surface in Figure 2.10a to illustrate a useful design tool. Moving along any of these contour lines produces the same estimate accuracy for varying values of n and SNR. This guides a potential design trade-off where the estimate degradation caused by presumably cheaper and smaller sensors with greater noise can be mitigated by increasing the number of sensors used. Conversely, if the integration of additional sensors becomes infeasible, Figure 2.10b can be used to determine the quality of sensor, via SNR, needed to produce a given estimate accuracy with a reduced set of sensors. A noteworthy trend shown by Figure 2.10b is that as SNR decreases, the contour lines have steeper slope with respect to the x-axis. This implies that as sensor quality decreases, additional sensors must be added *at an even greater rate* to achieve a consistent estimate accuracy.

To similarly quantify the effect of error in the sensor position $\boldsymbol{r}$, simulated state estimates were generated, and corresponding standard estimate errors were

calculated, for various values of sensor array size n and position error $\boldsymbol{\Delta r}$. Figure 2.11 displays the results of this characterization. For this simulation, the sensor SNR value was 50, a considerably lower noise case than is shown in Figure 2.10. The position error values are represented here as fractions of the maximum magnitude of the sensor position vectors, given by

$$\epsilon_r = \frac{||\boldsymbol{\Delta r}||_\infty}{||\boldsymbol{r}||_\infty} \tag{2.55}$$

A linear relationship is shown between position error fraction ϵ_r and standard estimate error σ_e. Similar to the results in Figure 2.10 for sensor noise, increasing the number of sensors in the array reduces the effect of position error on the state estimate accuracy.
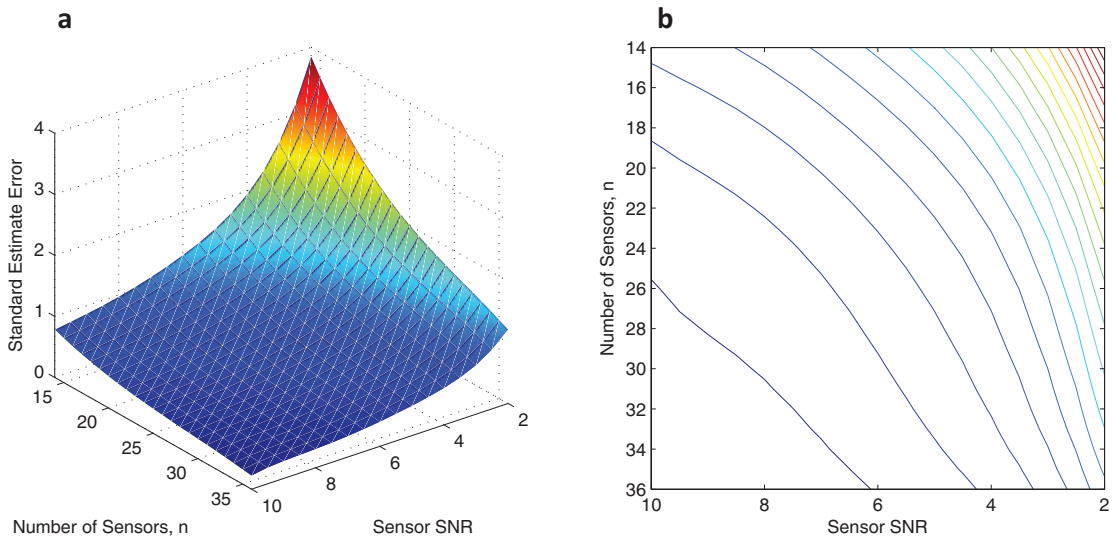
Figure 2.10: (a) Surface and (b) contour plots of the standard estimate error σ_e for varying number of sensors in the distributed array and raw sensor SNR.

40
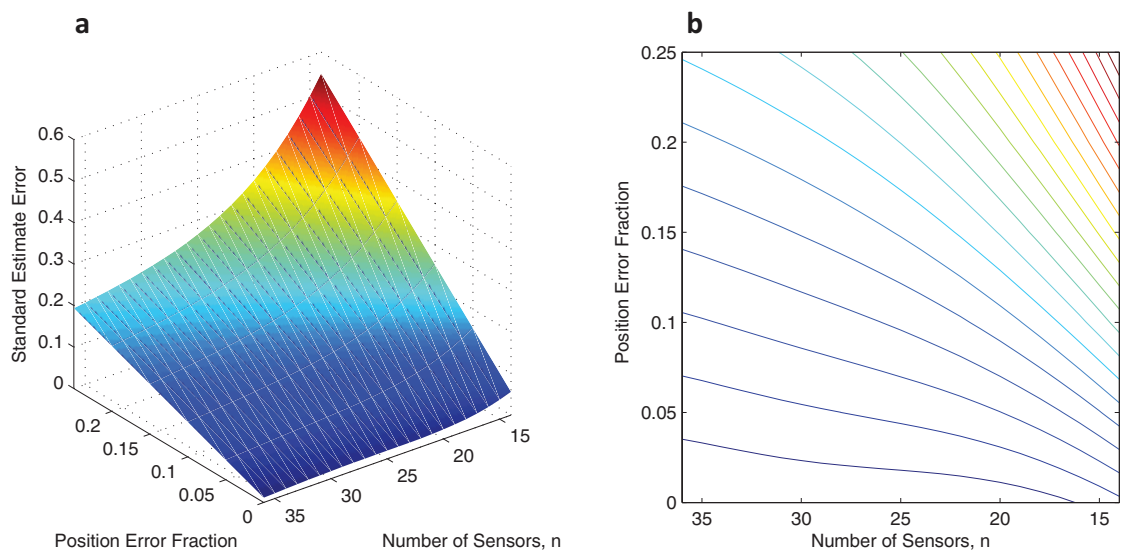
Figure 2.11: (a) Surface and (b) contour plots of the standard estimate error σ_e for varying number of sensors in the distributed array and sensor position error fraction ϵ_r.

Chapter 3:   Sensor Design and Testing

Section 3.1 presents the design and fabrication of an ocelli-inspired analog circuit based on the modeling described in Section 2.1, including static estimation outputs corresponding to pitch and roll rates. Characterization of the open-loop behavior of the sensor is detailed in 3.2, with comparison to alternative attitude rate sensors. Section 3.3 presents the design and automatic calibration methodology for the distributed accelerometer array. The estimate accuracy of the sensor is characterized in Section 3.4.

3.1   Ocellar Sensor Design

The simple structure and function of the ocellar system of flying insects is well suited to fully analog bio-mimetic hardware implementation. An analog implementation could provide near instantaneous feedback if paired with analog actuation, e.g. piezo-electric actuators. This fully analog closed-loop system would be capable of rejecting disturbances of much greater bandwidth than an equivalent digital sensing and actuation architecture. While the work presented here does not investigate a fully analog closed-loop, it demonstrates successful state estimation with an analog ocellar sensor. Furthermore, a performance comparison between this sensor

and other sensing modalities is carried out in open-loop and closed-loop tests.

An analog ocellar sensor design was formulated based on our model simulation of ocellar function (Figure 2.4d) and the resulting estimated measurement matrix C, (2.21), and estimation matrix M, (2.23), to extract pitch rate and roll rate, [56]. The design of this ocellar sensor is shown in Figure 3.1. The stages of the circuit can be segmented as light-to-voltage conversion, high-pass filtering, and static estimation. The initial stage is three TAOS TSL14S light-to-voltage converter-
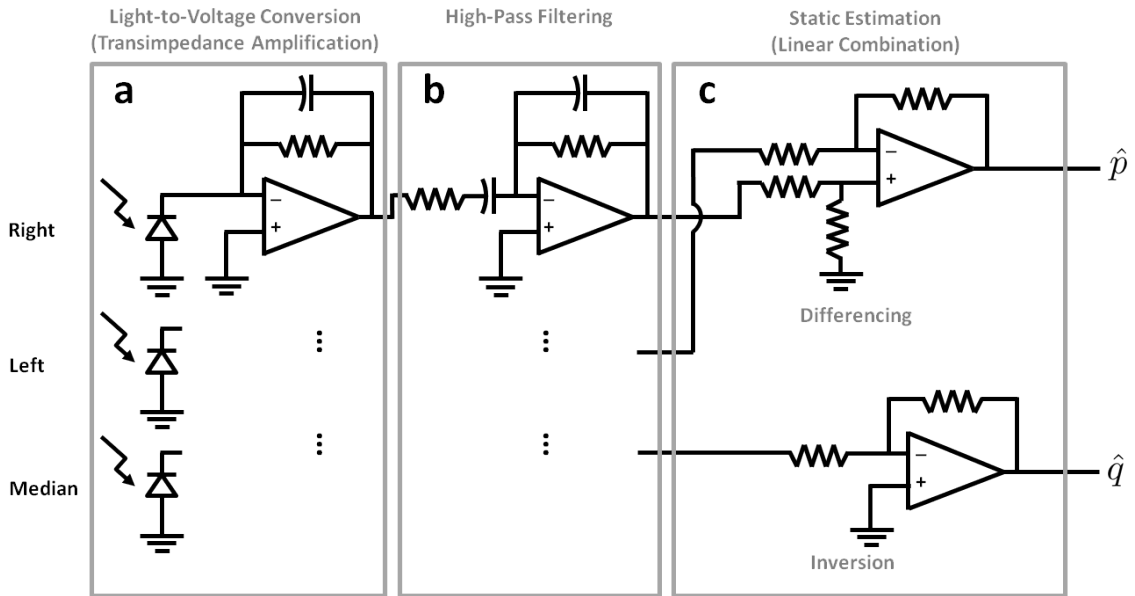
Figure 3.1: Ocellar circuit diagram with (a) light-to-voltage conversion, (b) high-pass filtering, and (c) static estimation stages

s shown in Figure 3.2a. Each of these sensors is comprised of a photodiode with internal transimpedance amplification (Figures 3.1a, 3.2c). It has a peak output for light intensities of wavelength $\lambda_p \approx 640$ nm with a response range of 350 nm to 1050 nm (Figure 3.2b), indicating the sensors peak sensitivity in the red and near-infrared wavelengths. Approximate spectral regions of visible light, ultraviolet
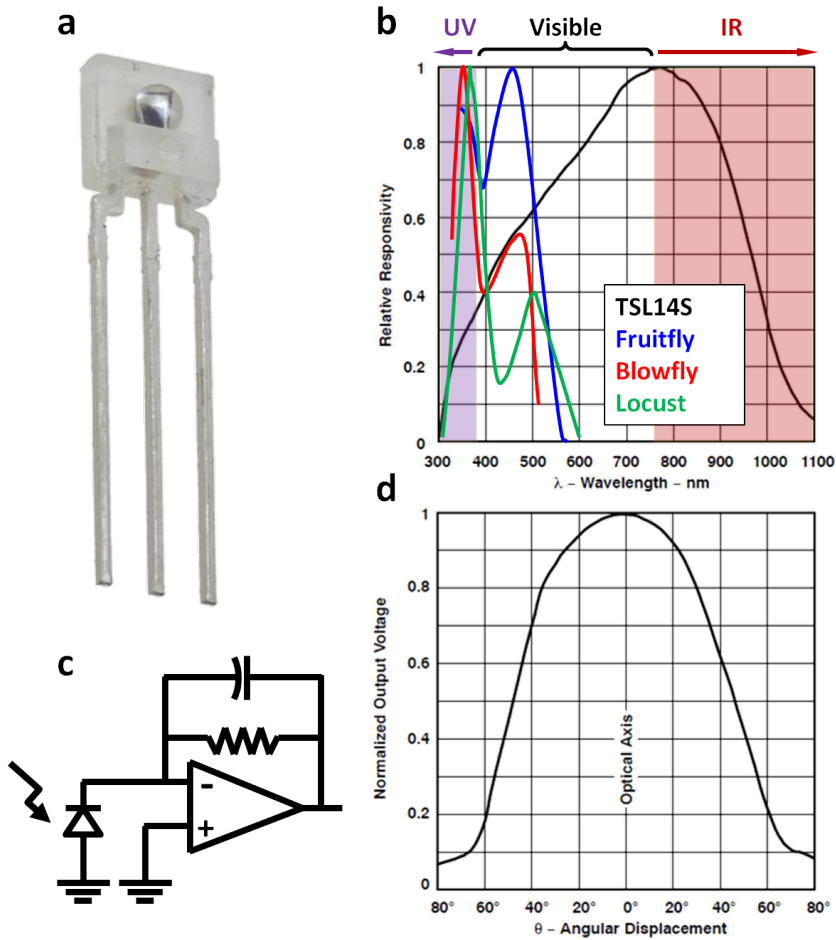
Figure 3.2: (a) TAOS TSL14S light-to-voltage converter, (b) normalized spectral sensitivity for TSL14S and ocelli of various species of flying insects, (c) sensor circuit diagram with transimpedance amplification, and (d) normalized angular sensitivity.

(UV), and infrared (IR) are shown for reference. Comparative aggregate curves of spectral sensitivity are shown for fruit fly, blowfly, and locust species as characterized by [16], [17], and [11], respectively. For each of these species the characteristic bimodal ocellar sensitivity in the UV and blue-green regions of the spectrum is seen. Though the sensor spectral sensitivity is not strictly bio-mimetic, it allowed for development and testing in an indoor laboratory environment, where UV light sources

were not present. Each of these sensors converts the incident input luminance to a proportional output voltage at a rate of 16 mV/(μW/cm^2). This output voltage is the electrical equivalent of the ocellar luminance, I, as shown in Figure 2.4d.

The second stage (Figure 3.1b) performs an inverting high-pass filtering of the photodiode output voltage to produce a voltage approximating the luminance time rate of change, $I' \approx \dot{I}$. The Intersil ISL28208 operational amplifier (op-amp) was used for filtering the analog voltage signals. The output voltage of an ideal differentiator is governed by

$$V_o(t) = -R_F C_S \frac{d}{dt}(V_i(t)) \tag{3.1}$$

However this circuit will amplify high frequency noise within the circuit itself, which must be attenuated. The low-pass filter op-amp circuit has the transfer function

$$\frac{V_o}{V_i} = -\frac{R_F}{R_S + sC_F R_F R_S} \tag{3.2}$$

Combining the ideal differentiator and low-pass filter yields the band-pass filter circuit shown in Figure 3.1b.

$$\frac{V_o}{V_i} = -\frac{sC_S R_F}{s^2 C_F R_F C_S R_S + s(C_F R_F + C_S R_S) + 1} \tag{3.3}$$

The characteristic quantities of this system are the low-pass cutoff frequency ω_L, high-pass cutoff frequency ω_H, unity gain frequency ω_o, and maximum input-output

gain A_V.

$$\omega_L = \frac{1}{R_F C_F}, \quad \omega_H = \frac{1}{R_S C_S}, \quad \omega_o = \frac{1}{R_F C_S}, \quad A_{max} = -\frac{R_F}{R_S} \tag{3.4}$$

For the component values shown in Table 3.1 these characteristic quantities are estimated as $\omega_L = 106$ rad/s, $\omega_H = 909$ rad/s, $\omega_o = 50$ rad/s, $A_{max} = -18.2$. The first two stages perform the operation depicted in the simulation model shown in Figure 2.4d.

The final stage (Figure 3.1c) performs a static estimation of the states $\hat{p}$ and $\hat{q}$ from the analog filtered luminances voltages, analogous to I'. These estimations are equivalent to the linear combinations represented by the rows of (2.23), emphasizing the proportional relationships between the measurements and state estimates. Again, the ISL28208 op-amps were used for the linear combination. The circuit in Figure 3.3a is a differential amplifier with input from the left and right filtered luminances, equivalent to the second row of (2.23). The output voltage of a differential
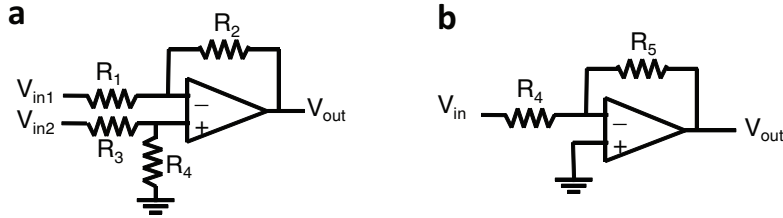
Figure 3.3: Ocellar subcircuits (a) Roll rate estimation differential amplifier, (b) Pitch rate estimation inverting amplifier

amplifier relates to the input voltages and discrete components as

$$V_{out} = \frac{(R_2 + R_1)R_4}{(R_3 + R_4)R_1} V_{in2} - \frac{R_2}{R_1} V_{in1} \tag{3.5}$$

46

Since the right and left ocellar outputs have equal contributions to the estimate of roll rate $\hat{p}$, the values of resistors R_1 through R_4 were chosen to preserve this ratio as given by

$$\frac{(R_2 + R_1)R_4}{(R_3 + R_4)R_1} = \frac{R_2}{R_1}. \tag{3.6}$$

The circuit in Figure 3.3b is an inversion of the median filtered luminance voltage signal. It is equivalent to the first row of (2.23). The output voltage of this subcircuit, the pitch rate estimate $\hat{q}$, is

$$V_{out} = -\frac{R_5}{R_4}V_{in}, \tag{3.7}$$

The inversion is needed to correct the sign change induced by the inverting high-pass filter in Figure 3.2c, which has negative voltage gain, (3.1).

Table 3.1: Ocellar sensor circuit component list

Name/Type	Manufacturer-SN	Value	Fig. 3.1 Label
Photodiode Light-to-Voltage Converter	TAOS-TSL14S		
Operational Amplifier	Intersil-ISL28208		
Resistor		1.1 kΩ	R_{b1}
		20 kΩ	R_{b2}
		1 kΩ	R_{c1}
		1 kΩ	R_{c2}
		1 kΩ	R_{c3}
		1 kΩ	R_{c4}
		1 kΩ	R_{c5}
		1 kΩ	R_{c6}
Capacitor		1 μF	C_{b1}
		0.47 μF	C_{b2}

This sensor design was initially fabricated and tested on a prototyping breadboard. The circuit was comprised of three TSL14S photodiodes, five op-amps, and

24 discrete electronic components. The photodiodes were mounted on a stepper motor for open loop characterization of the roll estimate response. Having tested the sensor prototype in a breadboard circuit, a printed circuit board (PCB) design was developed (Figure 3.4).
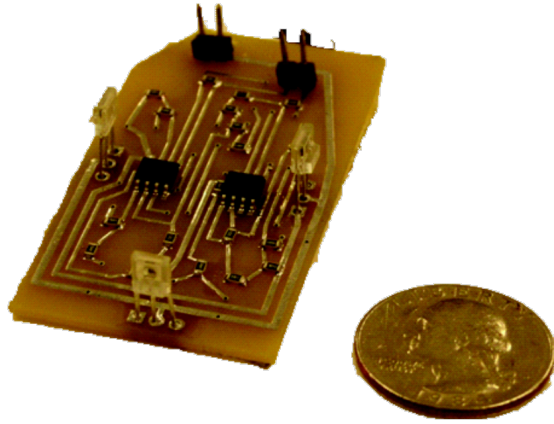
Figure 3.4: Printed circuit board ocellar sensor (US quarter shown for scale)

The final version of the sensor is an analog printed circuit board. The design was modified to have four photodiodes, rather than three, oriented toward the right, left, median, and aft directions (Figure 3.6a). This modification was chosen to correspond with the axisymmetric geometry of the quadrotor sUAS. Correspondingly, the circuitry for the pitch rate sensing was modified to replicate the circuitry for roll rate sensing, using antagonistic filtered luminance measurements between the median and aft photodiodes. The revised circuit diagram for this configuration is shown in Figure 3.5

This symmetric design, though less bio-inspired, allowed for a more simplified sensing and feedback implementation on a quadrotor vehicle, while maintaining
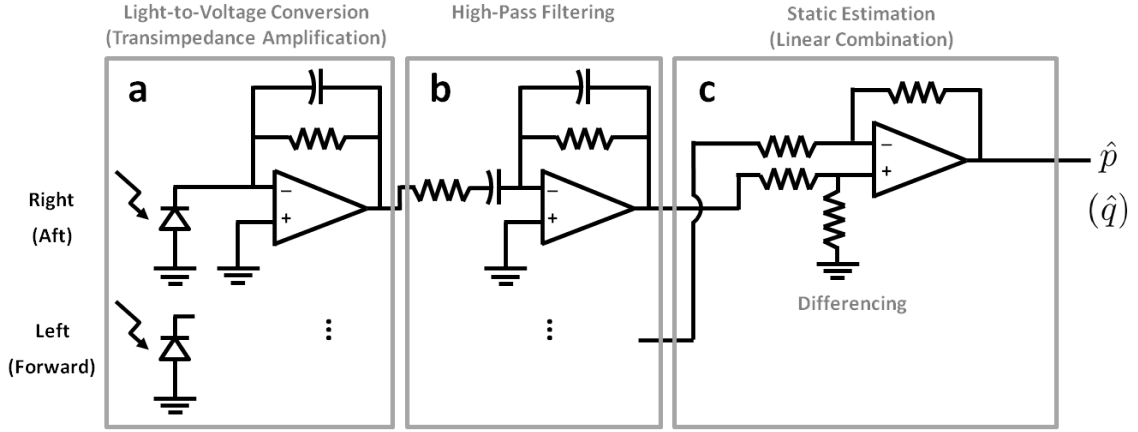
Figure 3.5: Axisymmetric ocellar circuit diagram with (a) light-to-voltage conversion, (b) high-pass filtering, and (c) static estimation stages

the same bio-inspired processing and filtering structure described and modeled in Section 2.1.2.

3.2 Ocellar Sensor Testing and Characterization

The open-loop performance of the ocellar sensor was characterized by comparison to a MEMS gyro, digital optic flow sensors, and an external visual motion capture system, while being subjected to controlled roll rate, p, stimulus motions provided by stepper motor (Figure 3.7). The MEMS gyro used was the Invensense MPU-6000. The digital optic flow sensors used were commercially available Ardu-Eye Aphid Vision Sensors from Centeye, Inc. (Figure 3.6b). Values from each of the three sensor modalities, the ocellar sensor, gyro, and optic flow sensors were queried simultaneously by the avionics board and transmitted to the data acquisition system. Corresponding ground truth measurements of roll rate were recorded with a

Vicon™ Motion Capture System.

The optic flow sensor array consisted of four small cameras, oriented in the same directions as the ocelli photodiodes: right, left, forward, and aft. Each camera processor calculated optic flow along the vertical image direction using a version of the image interpolation algorithm described by [57]. A single vertical component of average optic flow across the camera images was calculated for each camera. As with the ocelli sensor, the quantities from the right and left optic flow sensors were combined differentially to produce an estimate of rotational velocity about the roll axis. This performs a simplified rotational velocity estimation analogous to that performed by the interneurons of the insect visual system as described by [10].
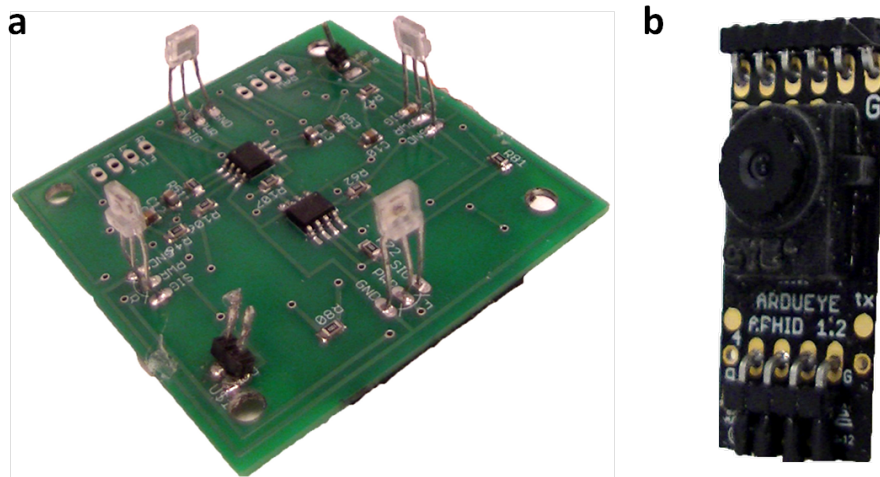
Figure 3.6: (a) Analog ocellar sensor, (b) Centeye, Inc. ArduEye Aphid optic flow sensor

A roll angle chirp stimulus was provided to the sensor suite by a stepper motor to characterize the comparative responses of the sensors across a range of input frequencies, Figure 3.8. The outputs of the sensors were scaled to match the units
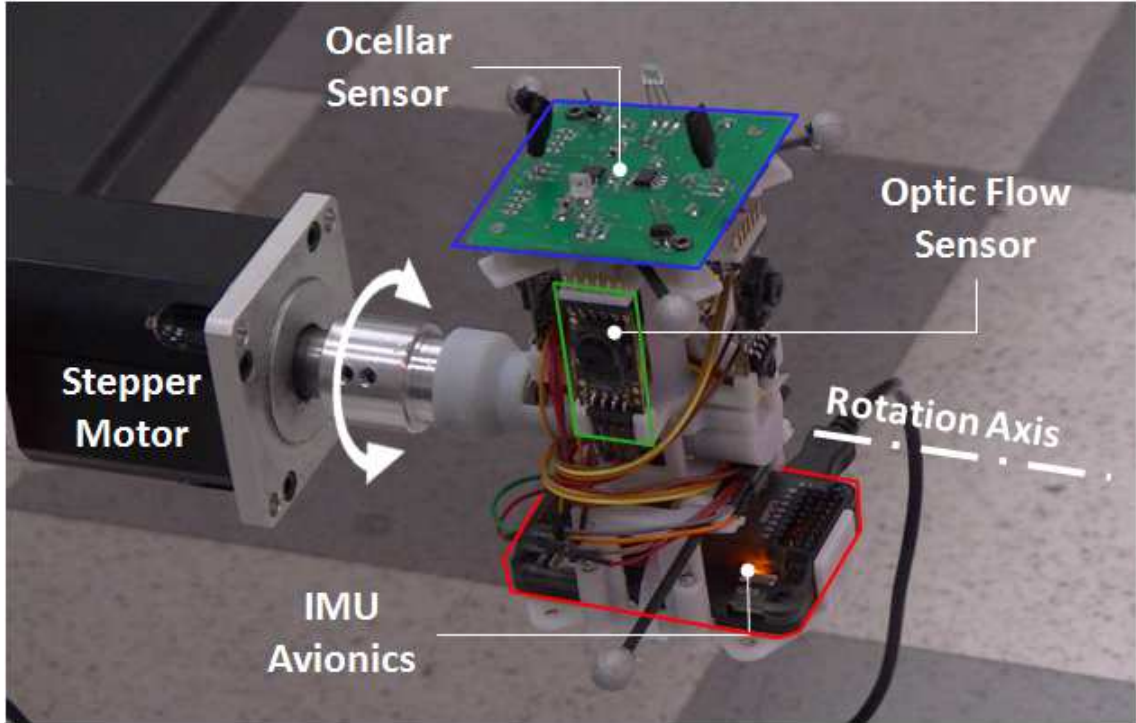
Figure 3.7: Open-loop characterization test apparatus for ocellar (blue), optic flow (green), and inertial (red) sensors

of Vicon™ (rad/s). Segments of the chirp response are displayed for comparison within three frequency ranges for 10, 2, and 1 second durations, respectively. From Figure 3.8, several key features are apparent. The gyro provides a measurement of consistent amplitude across the entire tested frequency range. The optic flow measurement provides an accurate rotation rate estimate at low input frequencies with a high signal-to-noise ratio but attenuates significantly at medium and high range frequencies. The ocellar sensor provides an output consistent in magnitude with Vicon™ measurements across medium and high frequency input ranges but has a very low SNR at low frequencies. The roll off in response of the ocelli at low frequencies is expected from the high-pass filtering stage, which is in agreement with

51

experimental results obtained in flying insects [6]. The noise in the ocellar sensor is due to the fluorescent lights and Vicon™ cameras that strobe at a frequency of 50 Hz and 100 Hz, respectively, which the sensor is able to detect. Testing in an outdoor environment, free from rapid luminance fluctuations, would eliminate this source of noise. However the intensity of natural outdoor lighting, specifically in the infrared wavelength, causes the photodiodes to saturate. Although this makes outdoor testing with the current photodiodes impossible, the results presented in this work would be consistent with components specifically selected for outdoor operation.

Using the Vicon™ roll rate measurement as the system input and the three scaled sensor measurements as system outputs, three transfer function estimates were calculated and are shown in Figure 3.9, with corresponding values of magnitude squared coherence. The magnitude squared coherence indicates that a linear input-output relationship exists at a given frequency. The coherence plot indicates that the transfer function estimates from this chirp stimulus can be trusted over a frequency range of approximately 4 rad/s to 50 rad/s. From the transfer function plots it is clear that the gyro and ocelli have relatively consistent magnitudes across all frequencies when compared to Vicon™. Conversely, the optic flow measurements show a roll off in magnitude as frequency increases. The phase diagram indicates a dilating phase delay between the Vicon™ measurement and all other sensor measurements due to a small time delay between the collection of these two data sets. For this reason, and the consistent scaling between the Vicon™ and gyro measurements across all frequencies, a scaled measurement from the gyro is consid-
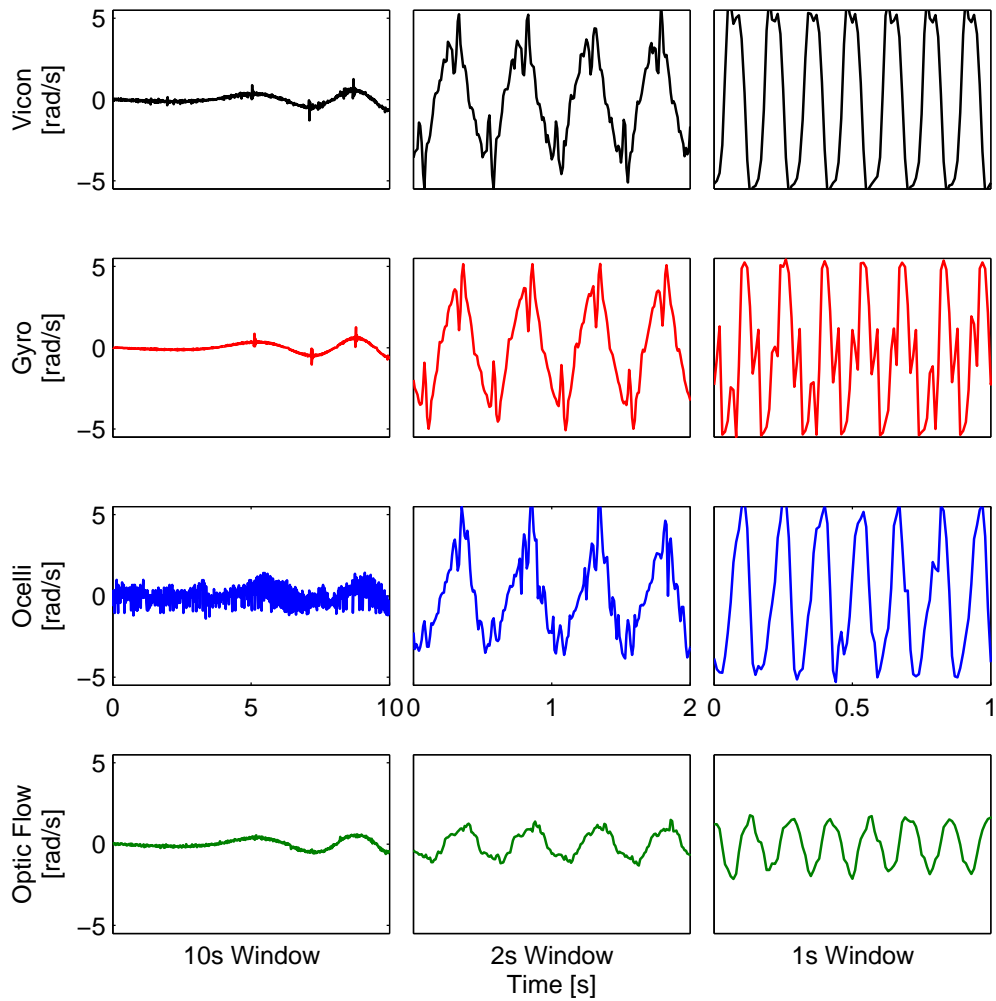
Figure 3.8: Chirp response time history comparison for ocellar, optic flow, and inertial sensors with motion capture ground truth

ered the ground truth measurement for remaining sensor comparisons. A new set of transfer function estimates were calculated for the sensor measurements, scaled to rad/s, with the gyro as the system input and the optic flow and ocellar sensors as the system outputs. Figure 3.10 displays these estimated transfer functions and the corresponding magnitude-squared coherence. This figure more clearly demonstrates

the complementary responses of the ocelli, which approach a gain of 0 dB, with respect to the gyro, at high frequencies with attenuation at low frequencies, while the optic flow has an approximate gain of 0 dB at low frequencies with attenuation at high frequencies. Furthermore, at low frequencies there is almost no phase lag between the gyro and the other sensor measurements, while at high frequencies the optic flow measurement is phase-delayed relative to the gyro by approximately 70° and the ocelli is phase-advanced relative to the gyro by approximately 50°.

A more thorough characterization of the response of the ocelli for varying amplitudes of angular rotation, using the MEMS gyro as the ground truth measurement was desired. The stepper motor was used to excite the sensors with a sinusoidal input to roll *angle*, ϕ, across a range of frequencies, 0.6 rad/s to 125 rad/s, and a range of angular amplitudes, 1° to 45°. For each pair of excitation frequency and amplitude the gyro-to-ocelli gain and phase were calculated. These values are shown in Figure 3.11 as a Bode surface plot to display variation of excitation amplitude. The black curve on each of these surfaces indicates the operational envelope of the stepper motor. Beyond this envelope, the output amplitude of the stepper motor does not match the desire amplitude and is attenuated to some degree. This data is also depicted in Figure 3.12 where the mean transfer function across input amplitude is shown in black. The noise in the transfer function estimate is effectively only in cases of both low frequency and low amplitude angular displacements, which is an expected failure mode of the sensor given its high-pass filter characteristics and the low visual resolution of the photodiodes. From Figures 3.11 and 3.12 it is noteworthy that for the majority of the operations envelope of the motor the magnitude and
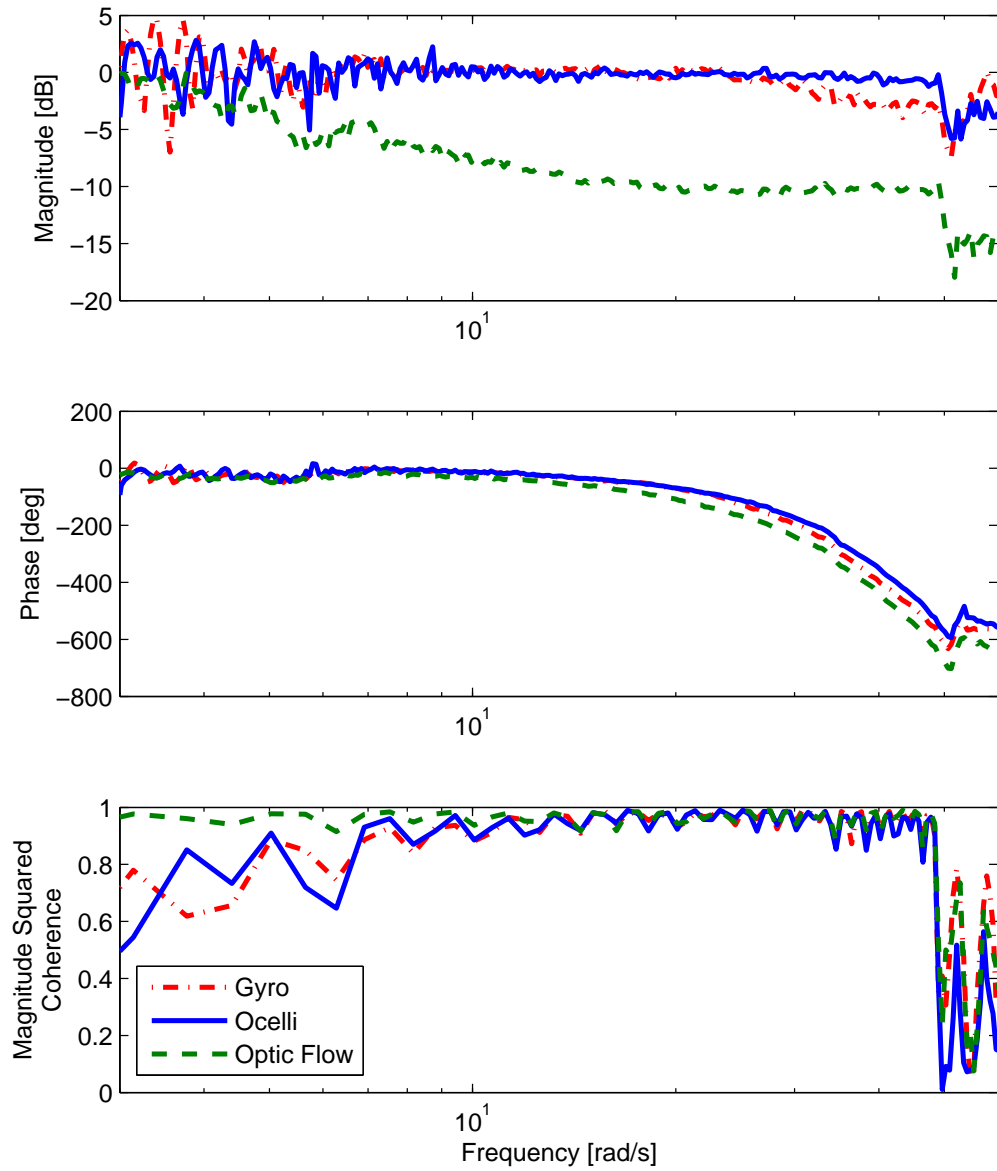
Figure 3.9: Transfer function estimate Bode and coherence plots from motor motion input, as measured by Vicon™, to output from visual and inertial sensors

phase relationship between the gyro and ocellar sensor are approximately constant across frequency. This is a favorable characteristic of the ocellar sensor which is de-
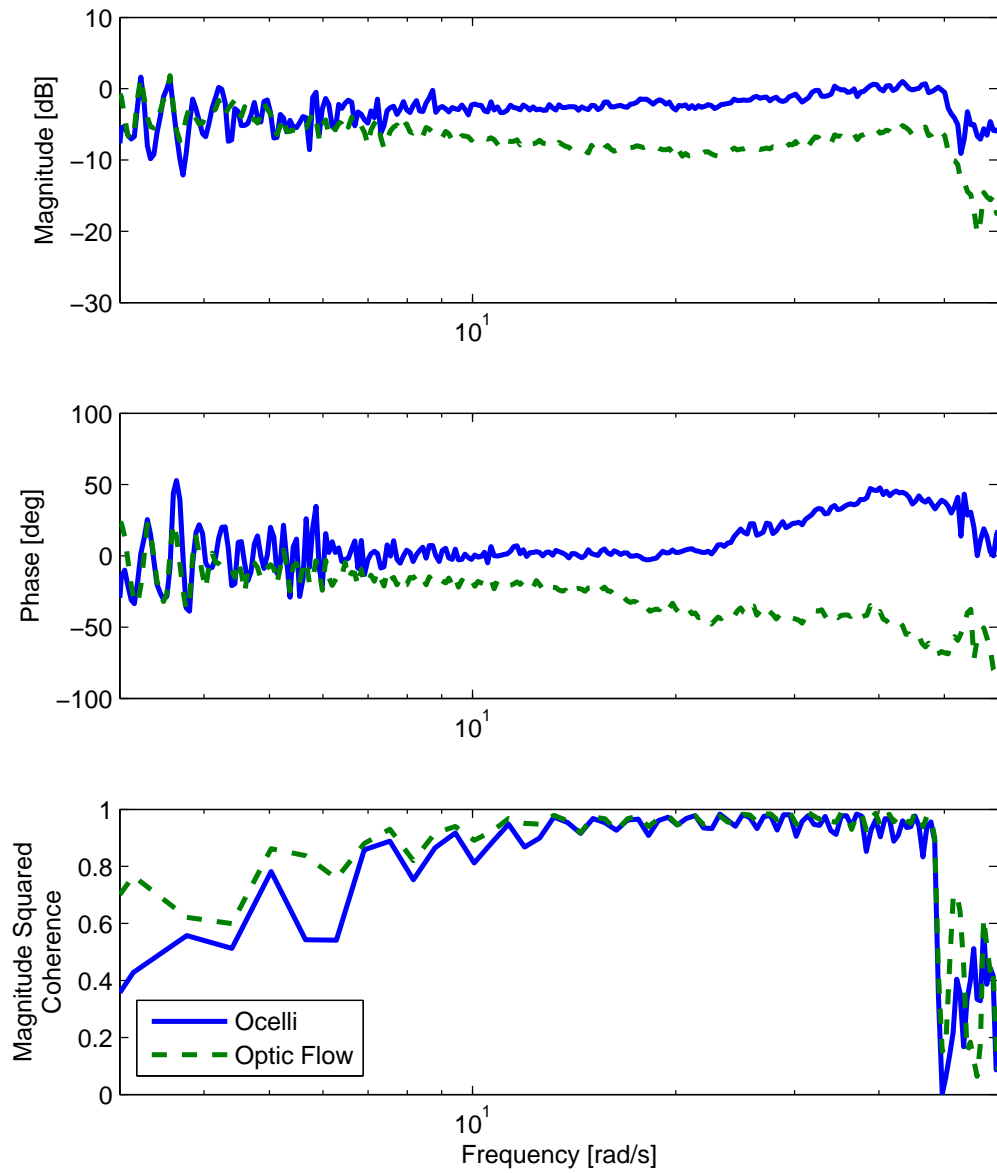
Figure 3.10: Transfer function estimate Bode and coherence plots from motor motion input, as measured by gyro, to output from visual sensors

signed to act as a visual rate gyro. This result suggests the ocellar sensor presented here is well-suited to provide rotation rate information over a large bandwidth of

excitation frequencies.
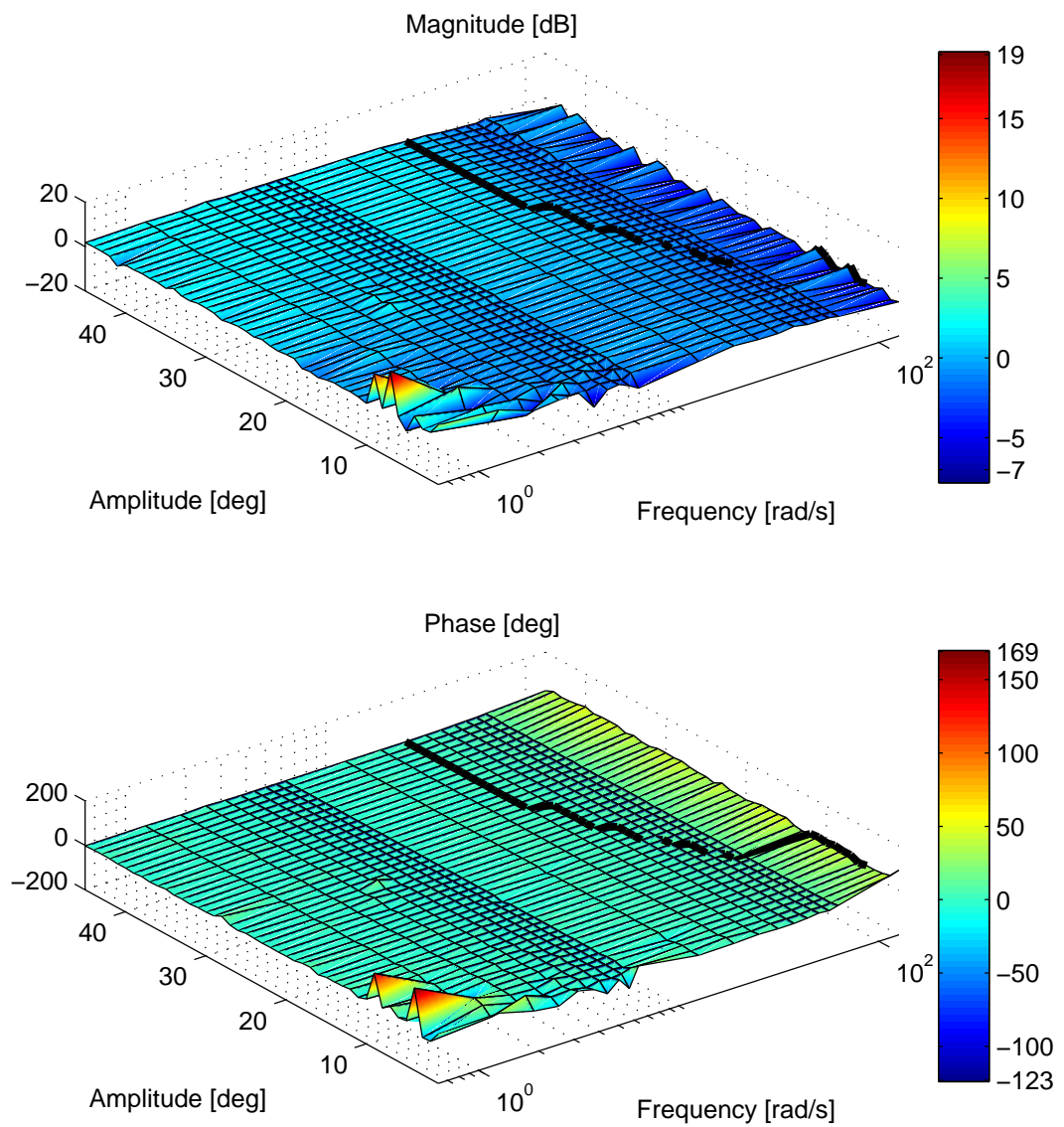
Figure 3.11: Bode plot of gyro-ocelli transfer function across varying input amplitudes, with stepper motor operational envelope shown (black)

It was shown in [18] through intracellular recordings that each descending neuron of fly ocelli is sensitive to rotations about a preferred axis. The fly ocelli were

57
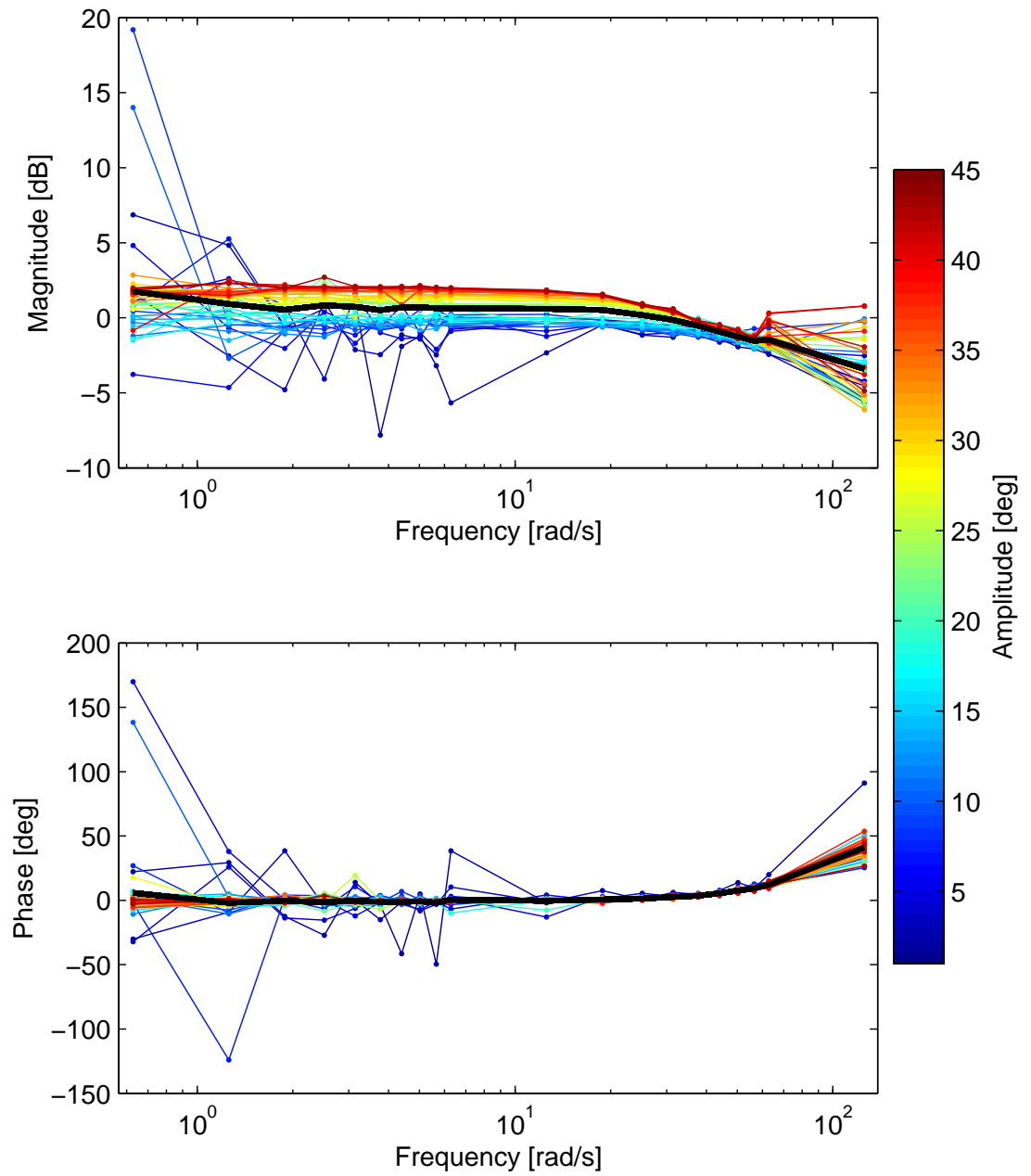
Figure 3.12: Bode plot of gyro-ocelli transfer function across varying input amplitudes, with mean transfer function (black)

subjected to sawtooth luminance stimuli that simulated rotation of the insect head about axes of varying azimuth angle. Plotting the normalized amplitude of the resulting intracellular response against this stimulus azimuth angle, they fit a cosine function and determined the direction of the axis that yielded maximal response. This was the direction of the preferred axis (PA), with these axes consistently distributed at azimuth angles of $0°$ and $\pm45°$ when measured for all descending neurons. The azimuth angle of the stimulus rotation axis, i.e. the stepper motor axis, was similarly varied while the response of the ocellar sensor roll rate $\hat{p}$ was recorded, Figure 3.13. Figure 3.14 shows the normalized amplitude of the response against the relative azimuth angle of the excitation axis. A cosine function was fit and the analogous preferred axis of sensitivity for the sensor roll rate output was determined to be $0.26°$. This is expected as the $\hat{p}$ estimate is designed to measure roll rotation rates about an axis with azimuth of $0°$. The broader implication of this finding, is that a sensor based on functional and behavioral models of the ocelli yields a response nearly identical to the electrophysiological response found in the biological analog [18]. This suggests that the sensor developed in this work concurs to a great degree with the insect ocelli in its function.
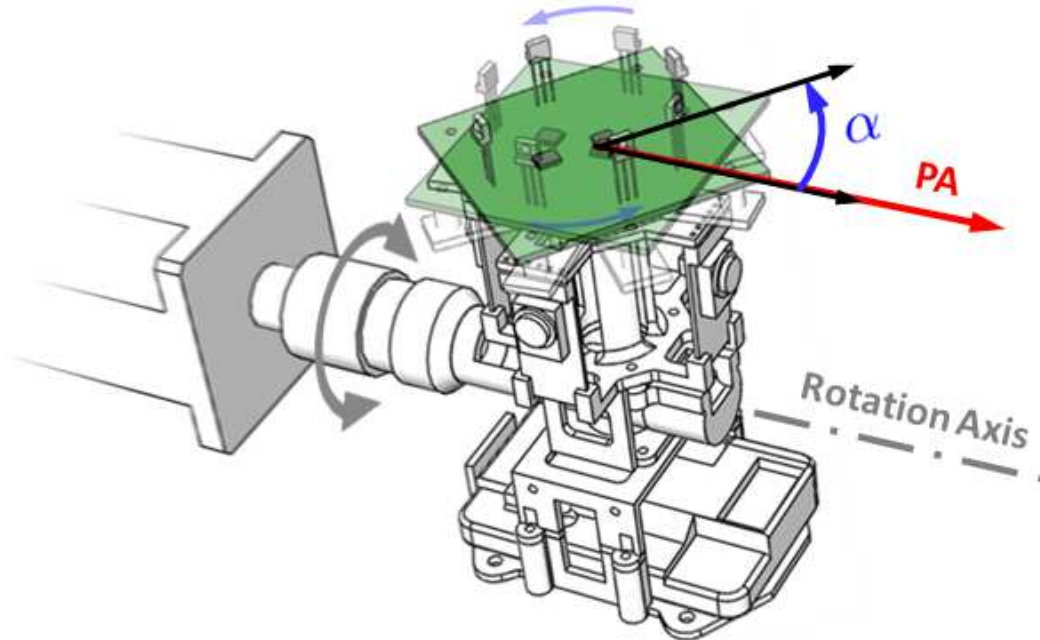
Figure 3.13: Preferred axis test apparatus, with ocellar sensor forward direction (black), stimulus axis angle, α (blue), and preferred axis (PA) of sensitivity (red) indicated

3.3 Distributed Acceleration Sensor Design

A distributed accelerometer sensor array was fabricated and tested for use on a quadrotor sUAS. To mitigate interfacing demands and sensor footprint, triaxial MEMS accelerometers were selected, specifically Analog Devices ADXL345. Each of these digital sensors provide three 10-bit measurements corresponding to three approximately mutually orthogonal sensitivity axes, with ± 4g range. A total of eight of the sensors were integrated into the sensor array, providing 24 total measurements as described in (2.43). The sensor measurements were collected and processed on an ArduPilot Mega avionics package, which was integrated on a quadrotor sUAS. The sensors were affixed to the vehicle at arbitrary locations, distributed away from
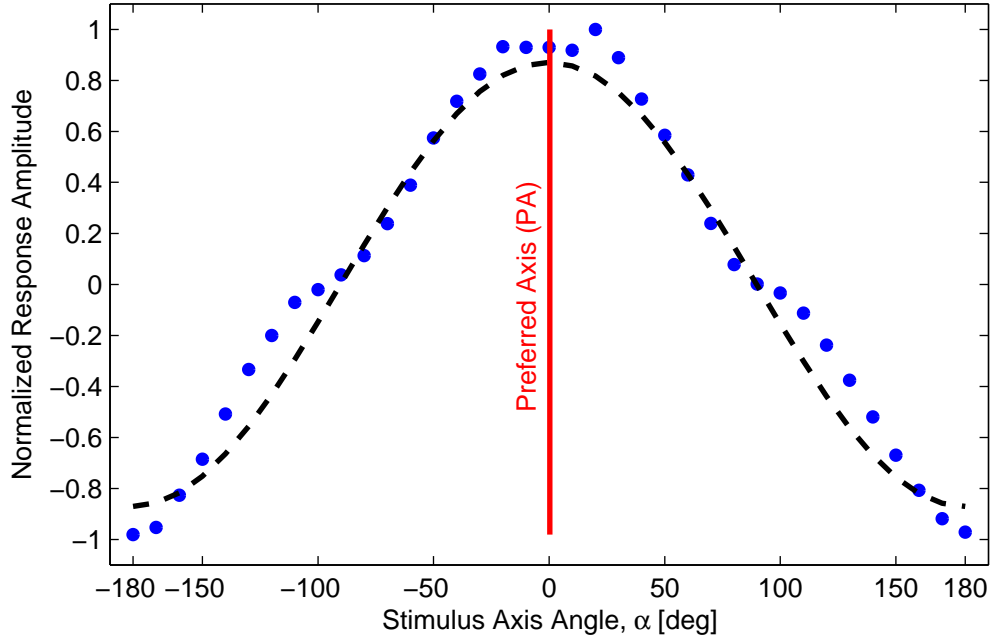
Figure 3.14: Normalized response amplitude for varying excitation azimuth angles, with cosine function fit (black) and preferred axis of sensitivity (red).

the vehicle center of mass, as shown in Figure 3.15.

To perform the static estimation described in (2.50) it is necessary to estimate the characteristic parameters, $\boldsymbol{\rho}_i$, for all n sensors, thereby calibrating the sensor array for any given arrangement. Directly measuring these quantities with precision is prohibitively difficult, particularly sensor orientation, $\boldsymbol{\zeta}_i^T$. Thus a method of automatic calibration was developed to estimate the values in $\boldsymbol{\rho}_i$. Using a Vicon™ visual motion capture system, the pose of the quadrotor airframe, and attached sensor array, are tracked while undergoing 6-DOF motions. Simultaneously, all 24 sensor measurement outputs, z_i, are recorded for the duration of the calibration sequence. Linear least-squares regression is used to fit the 12-dimensional linear
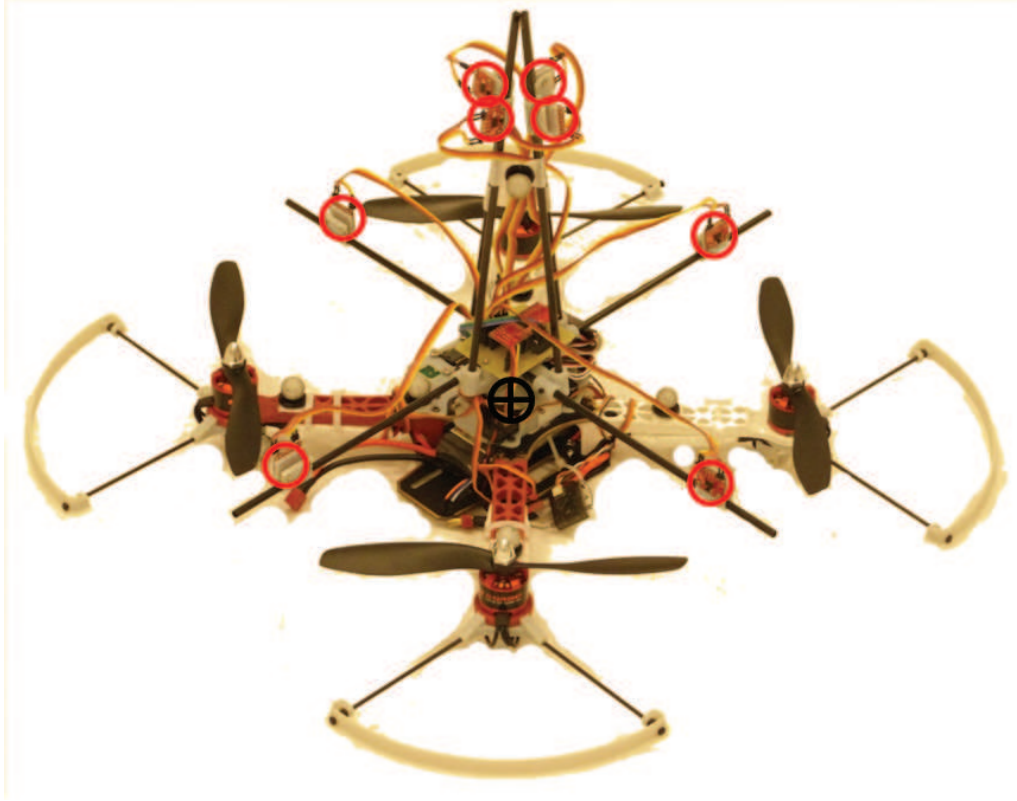
Figure 3.15: Distributed accelerometer array (red) integrated on a quadrotor vehicle.

parameter vector $\boldsymbol{\mu}_i^T$ and scalar bias b_i as

$$z_i(t) = \boldsymbol{\mu}_i^T \boldsymbol{\xi}(t) + b_i \tag{3.8}$$

where $z_i(t)$ is the time history of the output of the ith sensor for the entire calibration

sequence, and

$$\boldsymbol{\xi}(t) = f(\boldsymbol{x}(t)) \equiv [a_x(t) \quad a_y(t) \quad a_z(t) \quad \cdots$$

$$\cdots \quad -(q(t)^2 + r(t)^2) \quad (p(t)q(t) + \dot{r}(t)) \quad (p(t)r(t) - \dot{q}(t)) \quad \cdots$$

$$\cdots \quad (p(t)q(t) - \dot{r}(t)) \quad -(p(t)^2 + r(t)^2) \quad (q(t)r(t) + \dot{p}(t)) \quad \cdots$$

$$\cdots \quad (p(t)r(t) + \dot{q}(t)) \quad (q(t)r(t) - \dot{p}(t)) \quad -(q(t)^2 + p(t)^2)]^T$$

$$(3.9)$$

is the defined time history vector, which is a function of the time history of the acceleration state vector, that is $\boldsymbol{x}_{accel}(t)$. Given (2.45), (3.8), and the definitions of $\boldsymbol{x}_{accel}$, $\boldsymbol{\xi}$, and C, several useful relationships between $\boldsymbol{\mu}_i^T$ and $\boldsymbol{\rho}_i$ are noted.

$$[\mu_{i,1} \quad \mu_{i,2} \quad \mu_{i,3}] = \kappa_i [\cos\gamma_i \cos\beta_i \quad \sin\gamma_i \cos\beta_i \quad -\sin\beta_i] \qquad (3.10)$$

$$= \frac{1}{x_i} [\mu_{i,4} \quad \mu_{i,5} \quad \mu_{i,6}] \qquad (3.11)$$

$$= \frac{1}{y_i} [\mu_{i,7} \quad \mu_{i,8} \quad \mu_{i,9}] \qquad (3.12)$$

$$= \frac{1}{z_i} [\mu_{i,10} \quad \mu_{i,11} \quad \mu_{i,12}] \qquad (3.13)$$

From (3.10) the sensor elevation may be expressed β_i as a function of $\mu_{i,1}$, $\mu_{i,2}$, $\mu_{i,3}$, and β_i itself.

$$\beta_i = \cot^{-1}\left(-\frac{\mu_{i,1}}{\mu_{i,3}}\sec\left(\sin^{-1}\left(-\frac{\mu_{i,2}}{\mu_{i,3}}\tan\beta_i\right)\right)\right) \qquad (3.14)$$

Numerical solvers may be used to solve for β_i, from which values of κ_i and γ_i

clearly result via (3.10). Alternatively if κ_i is known from the sensor datasheet specifications, then β_i can be solved for uniquely in (3.10). The specifications for the ADXL345 indicate the gain κ_i has a nominal value of 13.05 LSB/m/s^2 (256 LSB/g) with relatively low variance (Figure 3.16). The assumption that the gain
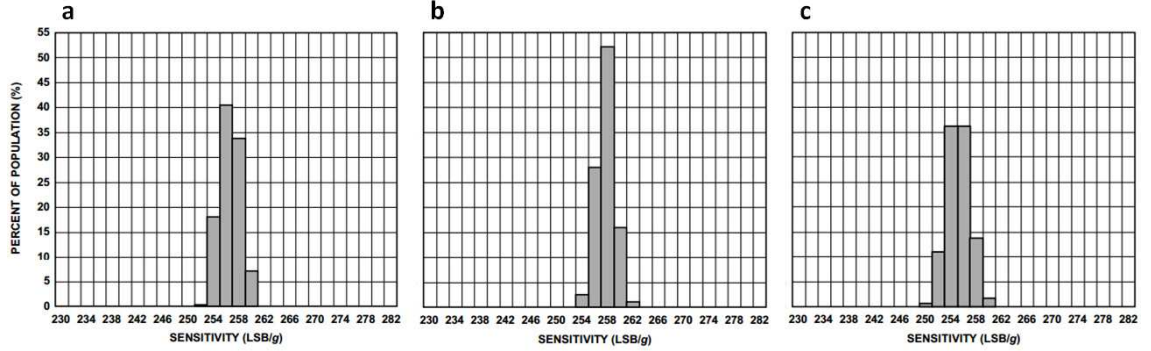
Figure 3.16: Frequency distribution of sensor gain, κ_i, for (a) x-axis, (b) y-axis, and (c) z-axis.

$\kappa_i = 13.05$ allows for direct estimation of the orientation parameters as

$$\beta_i = -\sin^{-1}\left(\frac{\mu_{i,3}}{\kappa_i}\right) \tag{3.15}$$

and

$$\gamma_i = \tan^{-1}\left(\frac{\mu_{i,2}}{\mu_{i,1}}\right) \tag{3.16}$$

Having identified values for κ_i, b_i, γ_i, and β_i, three additional least-squares regressions were performed between the elements of $\boldsymbol{\mu}_i^T$ as described by (3.11)-(3.13) to estimate the parameters x_i, y_i, and z_i. The parameter values $\boldsymbol{\rho}$ found via linear regression are then used as initial values for an output-error estimation algorithm, as described in [58], to refine the values comprising C and $\boldsymbol{b}$ to best fit (2.47).

64

The linear regression must be performed first because output-error estimation is an iterative identification process, which is thus computationally slower than linear regression, and it requires initial parameter estimates near the true value for successful convergence. Performing this two-phase calibration yields the estimated sensor positions and orientations for all 24 sensors, shown in Figure 3.17. The ground truth sensor positions are shown by a red circle as these are approximate values, measured manually with calipers.
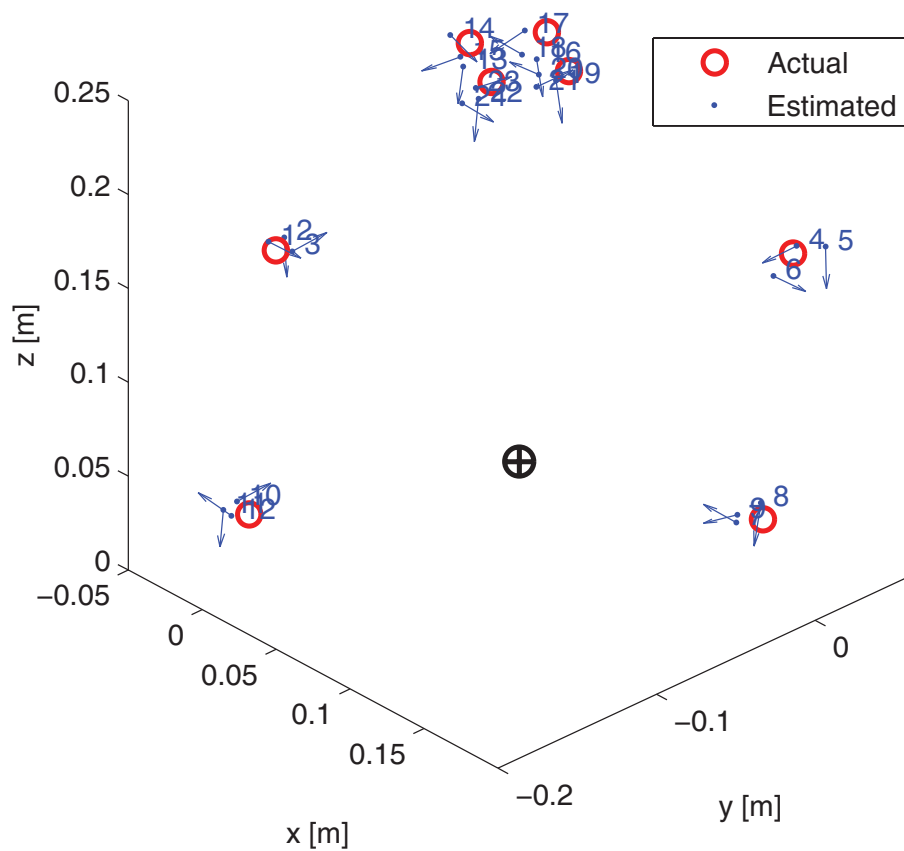
Figure 3.17: Estimated sensor positions and orientations from calibration: red circles indicate approximate ground truth position, blue numbered vectors indicate location and sensitivity direction of each ith sensor.

3.4 Distributed Acceleration Sensor Testing and Characterization

Here it is desirable to illustrate the efficacy of the measurement and estimation scheme described in Section 3.3. Having established a linear method for estimating the states in (2.30), these are compared to a ground truth measurement of the acceleration states.

A comparative plot is provided in Figure 3.18 between the output z_i of a single sensor axis and the output expected for a simulated sensor with the estimated parameter values of $\boldsymbol{\rho}_i$ for a calibration sequence. The accurate estimation of this relationship is the goal of the automatic calibration described in Section 3.3. Similarly, Figure 3.19 displays a comparison between the roll angular acceleration, $\dot{p}$, as measured by Vicon™ and the estimate, $\hat{\dot{p}}$, provided by the distributed sensor network as in (2.50). These two figures were produced for open loop acceleration stimuli induced with manual motion inputs. This illustrates the goodness of fit achieved by the automatic calibration, which can be performed in minutes.

While this provides a qualitative level of accuracy, it is desirable to analyze the estimate accuracy of the calibrated sensor array as a function of number of sensors n. A random subset of n sensors was selected from the 24 total sensors from which we formed the estimate $\hat{\boldsymbol{x}}_{accel}$ (2.50), where n varied from 13 to 24. Using a process similar to the characterization in Section 2.2.2 the state estimate accuracy is quantified via the standard estimate error σ_e (2.54). This process was repeated for 500 such randomly selected sensor subsets. Only 500 subsets were generated as the number of possible unique combinations of sensors p_n for each value of n is given
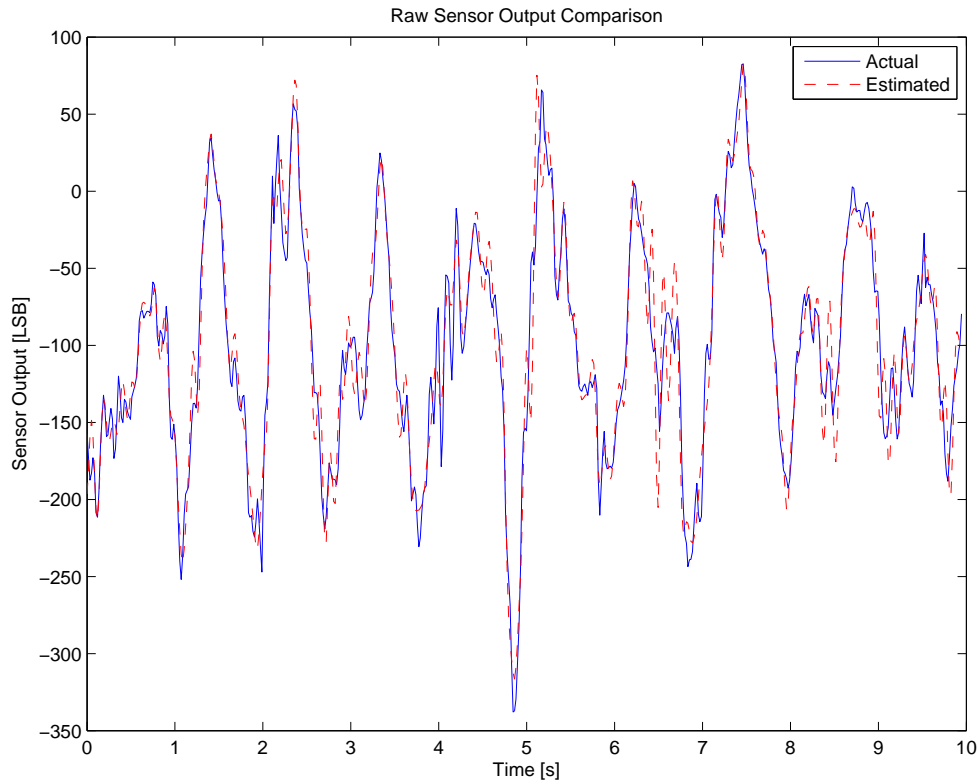
Figure 3.18: Comparison of actual and estimated sensor output for a single axis z_i.

by

$$p_n = \frac{24!}{n!(24-n)!},\tag{3.17}$$

yielding approximately $2.5{\times}10^6$ combinations for $n{=}13$. The mean values of the standard estimate error, and their corresponding standard deviations, across the 500 subsets are presented in Figure 3.20. A curve was fit through the mean values of σ_e given by

$$\sigma_e = \frac{1}{(n-11)^2} + 0.014\tag{3.18}$$
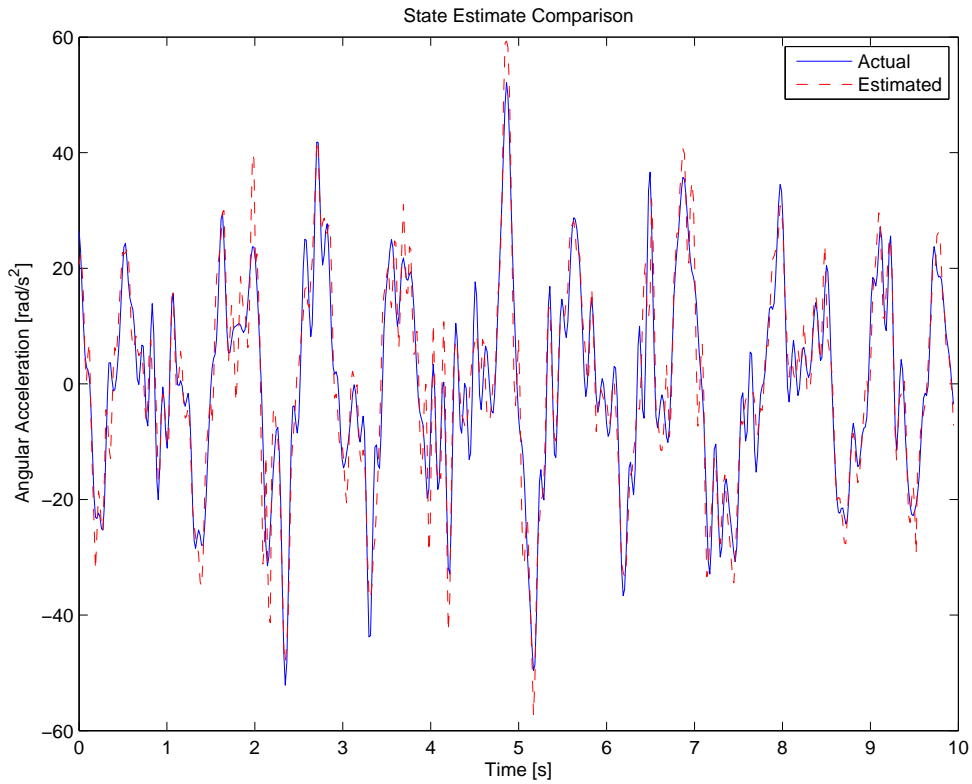
Figure 3.19: Comparison of actual and estimated roll angular acceleration $\dot{p}$.

This result confirms the improvement in estimate accuracy as the number of sensors increases, but with diminishing effect, as seen in Figures 2.10-2.11.

From the above results presented it may be asserted that the distributed acceleration sensing scheme described herein produces reliable and accurate measurements of the acceleration state vector (2.30). This sensor will provide estimates of applied forces and torques for use in disturbance rejection feedback, discussed in Section 4.2.
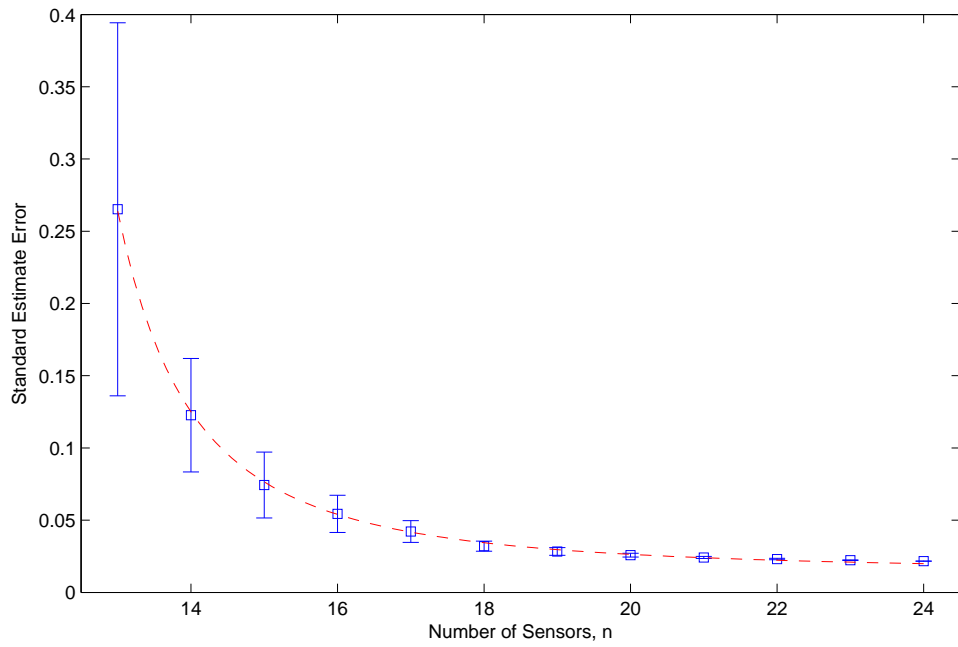
Figure 3.20: Standard estimate error σ_e as a function of the number of sensor measurements n. Mean values and standard deviations shown across 500 randomly selected sensor subsets. Curve (3.18) shown (dashed, red).

Chapter 4:   Closed Loop Implementation

Section 4.1.1 details the integration of the ocellar sensor and optic flow sensor onto the quadrotor sUAS. Section 4.1.2 presents the closed loop response for rate feedback from a gyro, ocellar sensor, or a complementary fusion of ocellar and optic flow measurements. Section 4.2.1 details several possible control strategies for disturbance rejection with distributed acceleration measurements. Section 4.2.2 describes the system identification modeling of the quadrotor sUAS for model-based control The closed loop response of the system is given in Section 4.2.3.

4.1   Ocelli-Based Disturbance Rejection

4.1.1   Control Design and Implementation

The avionics package and sensor suite described in Section 3.2 were integrated onto a DJI FlameWheel 330 quadrotor sUAS (Figure 4.1) to characterize the closed-loop performance of the ocellar sensor in comparison to the other sensing modalities for rejecting exogenous disturbances.

The avionics performs attitude tracking in pitch and roll through PID control with measurements from the onboard MPU-6000 IMU, including accelerometer and

gyro. To test the performance of the ocellar and optic flow sensors, the vehicle was subjected to impulse input roll commands. The impulse inputs were generated by including an additive disturbance to the speed controller command for a small number of inner loop cycles, subsequent to the attitude control computation. To induce a roll disturbance, this additive disturbance was added antagonistically to the right and left pairs of speed controllers. The magnitude of the impulse was the maximum extent of the allowable actuator command. This method of introducing perturbations allows for more precise and repeatable roll disturbances.

The vehicle control was modified so that proportional-integral (PI) control was provided by the IMU while allowing the derivative (D) component of the control to be provided by either the gyro, ocelli, ocelli with optic flow, or be omitted entirely. It is asserted by [59], that for a flapping wing micro-flier three assumptions would support stabilization of the vehicle using only rate feedback, i.e. no proportional attitude feedback. These assumptions are:

- The vehicle motion depends only on the forces and torques averaged over the time period of each wing stroke.

- The aerodynamic drag is equally proportional to the airspeed in the forward and lateral directions.

- The vehicle is symmetric about the $x - z$ plane.

While these assumptions do not necessarily hold for this flight vehicle, they present a solution to overcoming the difficulty of obtaining an absolute attitude estimate from

ocellar outputs, and a possible explanation for the evolution of this visual attitude control system in micro-fliers.

Using the open loop characterization and comparison between the visual and inertial sensors, described in Section 3.2, the derivative gain for each of the visual sensors was selected to normalize their response magnitude with that of the gyro and its corresponding derivative gain (Figure 3.10). More specifically, the ocellar sensor roll rate estimate was normalized by the high frequency gain ratio between its output and that of the gyro. Conversely, the optic flow roll rate estimate output was normalized by the low frequency gain ratio between its output and that of the gyro. This normalization process yielded measurements from both visual sensors that matched the inertial sensor for the frequency regime in which their estimates were of the highest magnitude and quality.

Having normalized the visual sensor to produce rotation rate estimates of the same scale as the inertial sensor nominally used for rate control, these measurements were then fed back in the roll attitude control loop, interchangeably with the gyro measurement. The ocelli-optic flow control was achieved with a complementary combination of the roll rate estimate from the ocelli, $\hat{p}_{ocelli}$, scaled by a factor f_c and the output of the optic flow sensor, $\hat{p}_{OF}$, scaled by the complement of f_c.

$$\hat{p} = f_c \hat{p}_{ocelli} + (1 - f_c)\hat{p}_{OF}, \qquad (4.1)$$

where $f_c = 0.89$. The weighting of the optic flow component in this complementary control had to be kept relatively low for stable closed-loop flight due to the phase lag

introduced by the optic flow measurement in regions of high frequency excitation, Figure 3.10. This simple combination is possible, because (1) both visual sensors were normalized by the ratio of their maximum output gain and the gyro output gain and (2) they demonstrate complementary frequency response magnitudes. As you move across frequencies one visual sensor response attenuates as the other amplifies. Thus, by choosing the complementary scale f_c, we effectively move along the frequency spectrum, simply by selecting the ratio between the two outputs. That is, for a high value of f_c, near 1, the roll rate is predominantly estimated with the ocellar sensor, effectively selecting a mixing in the high frequency regime shown in Figure 3.10. Correspondingly, low values of f_c, primarily weight the optic flow measurement in the roll rate estimate, effectively selecting a sensor mixing from the lower frequency region of Figure 3.10.

4.1.2   Performance Analysis

The response of the vehicle roll angle was recorded with the Vicon™ motion capture system while in free flight. The vehicle was subjected to 10 roll input impulses for each of the four derivative control cases. These cases were denoted as undamped, gyro damped, ocelli damped, and ocelli-optic flow damped. Figure 4.2 displays the aggregate results from these flight tests for the four control cases. The outer bounds of the 10 trajectories are shown as a shaded band and the mean trajectory is shown with a bold line.

Figure 4.1: Ocellar (blue) and optic flow (green) sensors integrated with IMU/avionics (red) sensor suite on a quadrotor vehicle

From the undamped response in black it is clear that the undamped PI control yields a *marginally* stable closed-loop system as indicated by the oscillations that do not attenuate with time, Figure 4.2. Thus, derivative feedback must be included to fully stabilize the system. The response with gyro damping demonstrates consistent performance with a diminished peak response and little noise or oscillation in the steady-state trajectory as shown by the narrowness of the shaded band. The ocelli

Table 4.1: Ocellar sensor impulse response performance metrics

D-Control Case	MSE	MSE_{tr}	MSE_{ss}	σ^2 [deg^2]	$\bar{M}_p$ [deg]	$\bar{t}_s$ [s]
Gyro	0.398	1.51	**0.031**	**0.249**	18.8	28.1
Ocelli	**0.393**	**1.30**	0.093	0.678	**17.6**	48.1
Ocelli-OF	0.565	2.01	0.088	0.902	21.0	**18.9**
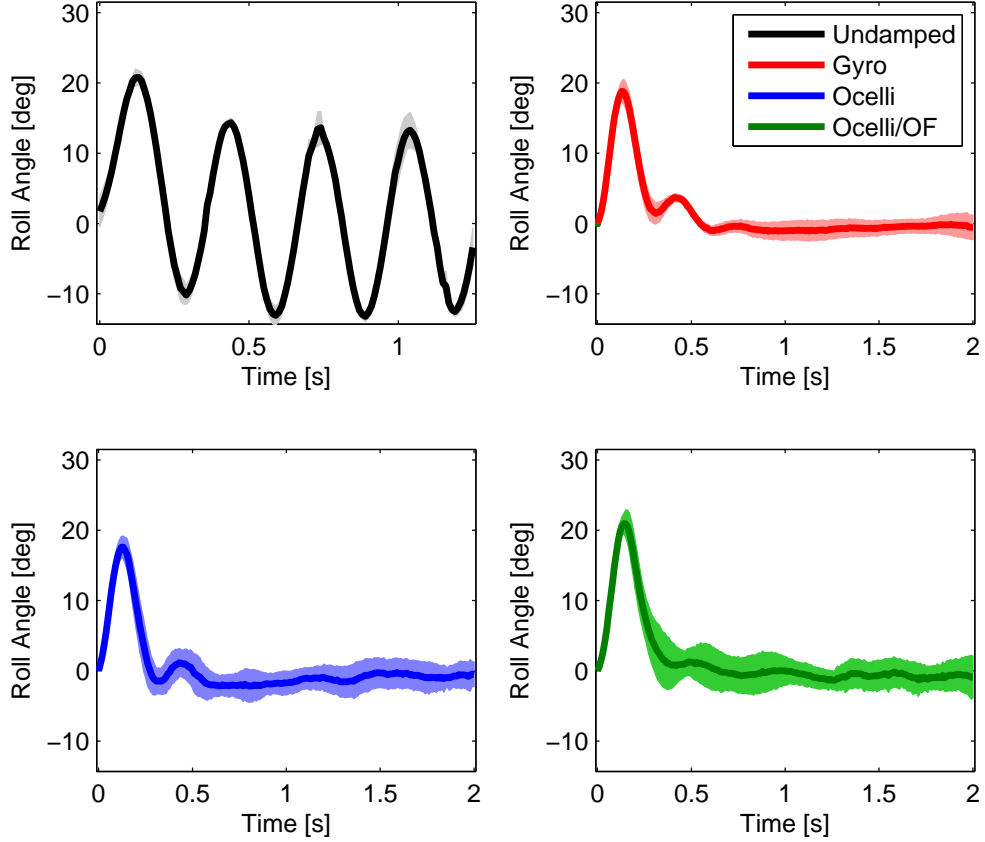
Figure 4.2: Impulse response time history aggregates for gyro, ocellar and ocellar-optic flow based damping feedback for actuator impulse disturbances

damping trajectories exhibit similar response to the gyro but with a higher level of variability in the response, due to the significantly higher levels of noise in the ocellar sensor. This noise is due to the fluctuation of the environment luminance from strobing light sources, such as fluorescent lighting and the Vicon™ system. The complementary ocelli-optic flow damping trajectories also exhibit an increased amount of noise over the set of trajectories than in the gyro damped case. Again, this is due to luminance noise in the ocellar sensor. This case also yields a larger
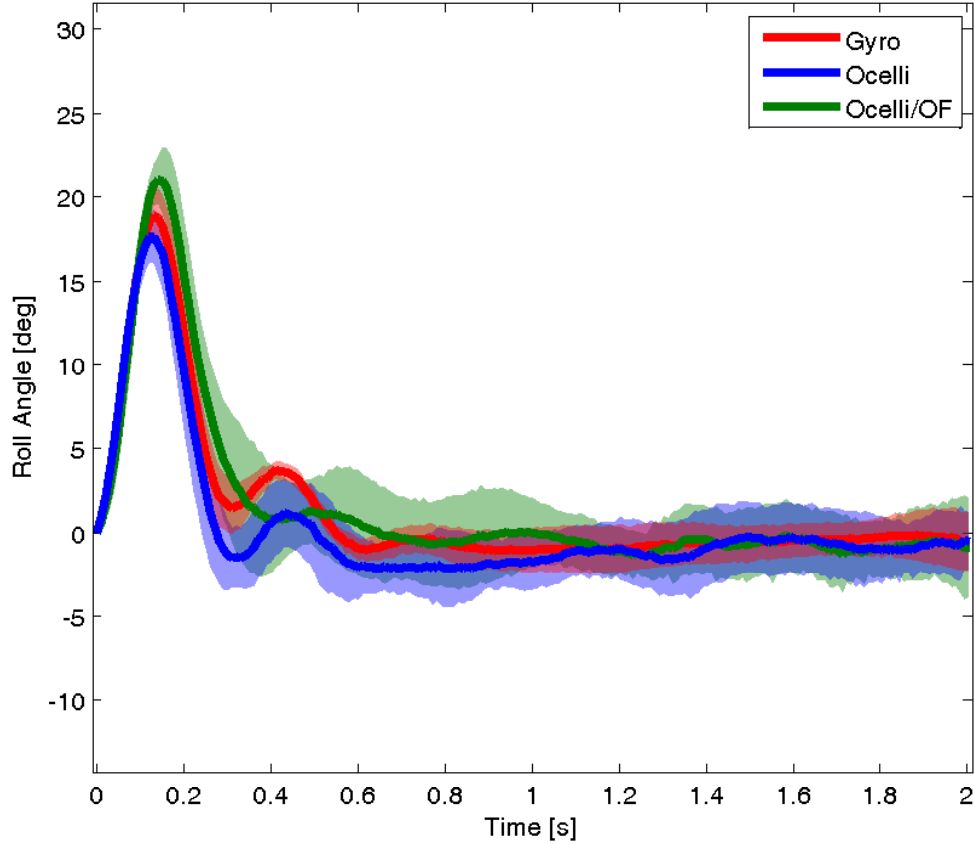
Figure 4.3: Overlaid impulse response time history aggregates for gyro, ocellar and ocellar-optic flow based damping feedback for actuator impulse disturbances

peak response to the impulse than the ocelli damped case. This is attributable to the diminished influence of the ocelli, as described in (4.1), which has a greater response at the high input frequencies imparted by the impulse. The ocelli-optic flow control exhibits a diminished secondary response peak than is seen in the gyro and ocelli damped cases. This is due to the improved low frequency damping provided by the optic flow feedback. Figure 4.3 displays the gyro damped, ocelli damped, and ocelli-optic flow damped response aggregates overlaid for comparison. The trajectory

extrema are displayed with thin lines and the mean trajectories with bold lines.

To quantify the energy of the response, the mean-squared error (MSE) for each of the four mean trajectories was calculated and is shown in Table 4.1. Also shown are the MSE values for the transient portion of the response, designated the transient error MSE_{tr}, and for the steady-state portion of the response, designated the steady-state error MSE_{ss}. This division illustrates that the ocelli damped response had a slightly better transient response and the gyro damped response had the best steady-state response. The ocelli-optic flow damped system also outperformed the ocelli damped system in steady-state response. The variance, σ^2, of the trajectories relative to the mean was calculated and shown in Table 4.1. This metric quantifies the greater consistency of the response of the gyro due to lower noise. The peak response of the mean trajectory, $\bar{M}_p$, was calculated for each case, illustrating that the ocellar feedback was actually better than the gyro at rejecting the initial transients caused by the impulse. The settling time of each mean trajectory, $\bar{t}_s$, was calculated for a threshold of $\pm 2°$ ($\pm 10\%$). The values, shown in Table 4.1, reveal that the settling time of the mean trajectory for the ocelli-optic flow control case was superior to both the gyro and ocelli cases.

This ocellar sensor design, which is implemented completely in analog circuity, thereby providing high speed loop closure, could be combined with a wide-field analog optic flow sensor, capable of estimating navigational states, to perform both inner and outer loop control using only visual sensing. [60] demonstrated successful autonomous navigation of unknown environments on a ground vehicle utilizing the same sensing, processing, and perception techniques as in the insect compound eye

system. The same bio-inspired visual obstacle avoidance mechanism was successfully extended to a micro air vehicle by [61]. The advantage of fusing analog ocellar sensing with analog optic flow navigational sensing is that a single visual sensor may produce all necessary inner and outer loop state estimates with high speed analog loop closure. This sensor could be miniaturized to an actual insect-scale flight vehicle, illustrating the potential power of the sensing mechanisms described in this work.

4.2 Distributed Acceleration-Based Disturbance Rejection

The evolution of the 6-DOF state of a flight vehicle is governed by the total forces and torques applied to the vehicle. These are typically categorized as gravitational, aerodynamic, actuation, and disturbance forces and torques. The disturbances manifest as error between the desired state of the vehicle and the actual state. Rapid, direct sensing of forces and torques can be used to track desired vehicle accelerations in the presence of these undesired exogenous disturbances.

4.2.1 Control Design

4.2.1.1 Small-Perturbation Theory

The state vector for an aircraft is typically given as

$$\boldsymbol{x} = \begin{bmatrix} u & v & w & p & q & r & \phi & \theta \end{bmatrix}^T \tag{4.2}$$

Using this defined state, the dynamics in (2.26) may be represented as

$$F_x = m(\dot{u} + qw - rv) \tag{4.3}$$

$$F_y = m(\dot{v} + ru - pw)$$

$$F_z = m(\dot{w} + pv - qu)$$

$$\tau_x = I_x\dot{p} - I_{xz}\dot{r} + qr(I_z - I_y) - I_{xz}pq$$

$$\tau_y = I_y\dot{q} + rp(I_x - I_z) + I_{xz}(p^2 - r^2)$$

$$\tau_z = I_z\dot{r} - I_{xz}\dot{p} + pq(I_y - I_x) - I_{xz}qr$$

Small-perturbation theory as outlined in [62] is applied, where any state x, force F, or torque τ may be represented as a steady state trim value plus a deviation, respectively as $x = \bar{x} + \Delta x$, $F = \bar{F} + \Delta F$, and $\tau = \bar{\tau} + \Delta\tau$. Then assuming a reference flight condition, hover in this case, all trim states, forces, and torques may be set to zero, leaving only perturbation states. Furthermore, by assuming the perturbation states Δx are small it is asserted that the products of these, e.g. $\Delta p \Delta q$ or Δp^2 are

negligible, yielding

$$\Delta F_x = m\Delta\dot{u} \tag{4.4}$$

$$\Delta F_y = m\Delta\dot{v}$$

$$\Delta F_z = m\Delta\dot{w}$$

$$\Delta\tau_x = I_x\Delta\dot{p} - I_{xz}\Delta\dot{r}$$

$$\Delta\tau_y = I_y\Delta\dot{q}$$

$$\Delta\tau_z = I_z\Delta\dot{r} - I_{xz}\Delta\dot{p}$$

Expanding each perturbation force or torque as a Taylor series approximation of the perturbation states, controls, and disturbances yields

$$\Delta F_x \equiv \Delta X = \frac{\partial X}{\partial u}\Delta u + \cdots + \frac{\partial X}{\partial u_R}\Delta u_R + \cdots + \frac{\partial X}{\partial d_u}\Delta d_u + \cdots \tag{4.5}$$

where, for example, u_R is the roll actuator input and d_u is the u-velocity disturbance state. Substituting this expansion into (4.5)

$$\frac{\partial X}{\partial u}\Delta u + \cdots + \frac{\partial X}{\partial u_R}\Delta u_R + \cdots + \frac{\partial X}{\partial d_u}\Delta d_u + \cdots = m\Delta\dot{u} \tag{4.6}$$

the stability, control, and disturbance derivatives are defined as

$$X_u = \frac{\partial X}{m\partial u}, \quad X_{u_R} = \frac{\partial X}{m\partial u_R}, \quad X_{d_u} = \frac{\partial X}{m\partial d_u}, \cdots \tag{4.7}$$

80

Substituting these quantities into (4.5), and solving for the state derivative yields

$$\Delta \dot{u} = X_u \Delta u + \cdots + X_{u_R} \Delta u_R + \cdots + X_{d_u} \Delta d_u + \cdots \qquad (4.8)$$

Similarly, for illustration, the roll dynamics yield

$$\Delta \dot{p} = L_u \Delta u + \cdots + L_{u_R} \Delta u_R + \cdots + L_{d_u} \Delta d_u + \cdots \qquad (4.9)$$

4.2.1.2 6-DOF State-Space Formulation

Applying the small-perturbation theory of (4.5)-(4.8) to the dynamic equations in (4.4), the open loop vehicle plant may be represented in linear state space form as

$$\dot{\boldsymbol{x}} \;=\; A\boldsymbol{x} + B\boldsymbol{u} + G\boldsymbol{d} \qquad (4.10)$$

$$\boldsymbol{y} \;=\; C\boldsymbol{x}$$

and may be represented under closed loop control by the block diagram in Figure 4.4
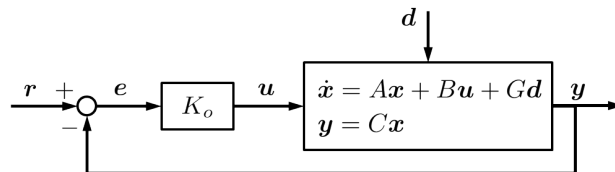
Figure 4.4: State space block diagram with feedback

where the input vector is comprised of the roll, pitch, throttle, and yaw controller commands

$$\boldsymbol{u} = \begin{bmatrix} u_R & u_P & u_T & u_Y \end{bmatrix}^T \tag{4.11}$$

and the disturbance vector is comprised of disturbance states, representing gust disturbances in the six velocity states

$$\boldsymbol{d} = \begin{bmatrix} d_u & d_v & d_w & d_p & d_q & d_r \end{bmatrix}^T \tag{4.12}$$

as is consistent with [63] and [64]. Here typical quantities are assumed for the stability, control, and disturbance derivatives of a quadrotor vehicle, which is often represented as having dynamics decoupled about each axis, i.e. $X_v \approx Y_u \approx L_u \approx M_p \approx \cdots \approx 0$. The typical closed loop controller K_o stabilizes this system

In the case without disturbance, $\boldsymbol{d} = 0$, it is expected that the attitude controller has been designed to generate reference controller commands $\boldsymbol{u}_r$ to drive the vehicle state to a reference $\boldsymbol{x}_r$. For the linear model in (4.10) the inputs $\boldsymbol{u}$ directly affect the state derivative $\dot{\boldsymbol{x}}$ through the linear mapping B, which represents the actuator authority. The state derivatives then propagate to the state $\boldsymbol{x}$ through the system dynamics, represented by A, which includes aerodynamics, gravitational acceleration, and kinematics. The disturbances $\boldsymbol{d}$ are similarly mapped to the state derivative via G. Traditionally, inertial sensing only extracts information from the lower order states, not directly affected by the input commands or disturbances.

This is represented in (4.10) by the mapping C which typically only encodes the low order states, such as p, q, r, ϕ, and θ. The actuation and disturbance forces do not typically appear directly in the inertial sensing scheme, instead these accelerations must propagate through the dynamics in A before they are sensed and used in feedback control. The unique sensing scheme of the distributed accelerometers provides direct sensing of the accelerations in $\dot{\boldsymbol{x}}$ imparted by the actuators and disturbances. This allows for a more effective disturbance rejection by sensing these forces and torques before they propagate to lower order states.

A typical state space model is represented for the 6-DOF system of a quadrotor in the form of (4.10) with the state vector in (4.2) and defined mappings (4.14). Here, the measurement vector is

$$\boldsymbol{y} = C\boldsymbol{x} = \begin{bmatrix} p & q & r & \phi & \theta \end{bmatrix}^{T} \tag{4.13}$$

$$
A \;=\; \begin{bmatrix}
X_u & 0 & 0 & 0 & 0 & 0 & 0 & -g \\
0 & Y_v & 0 & 0 & 0 & 0 & g & 0 \\
0 & 0 & Z_w & 0 & 0 & 0 & 0 & 0 \\
0 & 0 & 0 & L_p & 0 & 0 & 0 & 0 \\
0 & 0 & 0 & 0 & M_q & 0 & 0 & 0 \\
0 & 0 & 0 & 0 & 0 & N_r & 0 & 0 \\
0 & 0 & 0 & 1 & 0 & 0 & 0 & 0 \\
0 & 0 & 0 & 0 & 1 & 0 & 0 & 0
\end{bmatrix}
,\,B \;=\; \begin{bmatrix}
0 & 0 & 0 & 0 \\
0 & 0 & 0 & 0 \\
0 & 0 & Z_T & 0 \\
L_R & 0 & 0 & 0 \\
0 & M_P & 0 & 0 \\
0 & 0 & 0 & N_Y \\
0 & 0 & 0 & 0 \\
0 & 0 & 0 & 0
\end{bmatrix}
$$

$$
G \;=\; \begin{bmatrix}
-X_u & 0 & 0 & 0 & 0 & 0 \\
0 & -Y_v & 0 & 0 & 0 & 0 \\
0 & 0 & -Z_w & 0 & 0 & 0 \\
0 & 0 & 0 & -L_p & 0 & 0 \\
0 & 0 & 0 & 0 & -M_q & 0 \\
0 & 0 & 0 & 0 & 0 & -N_r \\
0 & 0 & 0 & 0 & 0 & 0 \\
0 & 0 & 0 & 0 & 0 & 0
\end{bmatrix}
\tag{4.14}
$$

$$C = \begin{bmatrix} 0 & 0 & 0 & 1 & 0 & 0 & 0 & 0 \\ 0 & 0 & 0 & 0 & 1 & 0 & 0 & 0 \\ 0 & 0 & 0 & 0 & 0 & 1 & 0 & 0 \\ 0 & 0 & 0 & 0 & 0 & 0 & 1 & 0 \\ 0 & 0 & 0 & 0 & 0 & 0 & 0 & 1 \end{bmatrix}, K_o = \begin{bmatrix} K_p & 0 & 0 & K_\phi & 0 \\ 0 & K_q & 0 & 0 & K_\theta \\ 0 & 0 & 0 & 0 & 0 \\ 0 & 0 & K_r & 0 & 0 \end{bmatrix} \qquad (4.15)$$

The values for the parameters of the generic 6-DOF system are given in Table 4.2.

Table 4.2: Generalized quadrotor 6-DOF vehicle model parameters (4.10)

Parameter Name	Parameter Value	Parameter Name	Parameter Value	Parameter Name	Parameter Value
X_u	-0.02	Y_v	-0.02	Z_w	-0.5
L_v	-0.005	M_u	-0.005	N_r	-0.01
L_R	0.02	M_P	0.02	Z_T	0.04
N_Y	0.002	K_p	400	K_q	400
K_ϕ	2000	K_θ	2000	K_r	300

4.2.1.3 Static Force Feedback

The attitude controller K_o is applied to the lower order states (4.13) of the plant, Figure 4.5, to produce stable attitude tracking. Through block diagram manipulation, as detailed in Appendix A, this loop may be represented as in Figure 4.6 where the manipulated control K_M and manipulated plant G_M are given by

$$K_M = H^{-1}PK_o = G^{-1}BK_o \qquad (4.16)$$

85
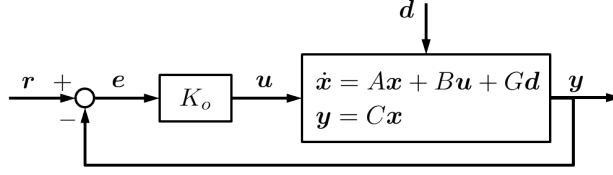
Figure 4.5: State space block diagram with feedback from IMU
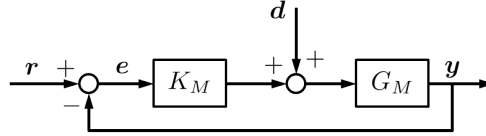
Figure 4.6: Manipulated state space block diagram with feedback from IMU

$$G_M = s^{-1}CH = C(sI - A)^{-1}G \qquad (4.17)$$

and the defined dynamic systems P and H are

$$P \equiv s(sI - A)^{-1}B, \quad H \equiv s(sI - A)^{-1}G \qquad (4.18)$$

The choice of P and H are more fully illustrated in Appendix A.

The loop transfer function L_o, when viewing the system from the output $\boldsymbol{y}$ as is typical, is defined

$$
\begin{aligned}
L_o \quad &\equiv \quad G_M K_M \qquad (4.19) \\
&= \quad s^{-1}CPK_o \\
&= \quad C(sI - A)^{-1}BK_o
\end{aligned}
$$

Correspondingly, the sensitivity transfer function S_o and complementary sensitivity transfer function T_o, are defined as

$$S_o \equiv (I + L_o)^{-1} \tag{4.20}$$

$$T_o \equiv L_o(I + L_o)^{-1} \tag{4.21}$$

where the mapping from reference $\boldsymbol{r}$ to output $\boldsymbol{y}$ is given by T_o, and the mapping from disturbance $\boldsymbol{d}$ to output $\boldsymbol{y}$ is given by $S_o G_M$, that is

$$\boldsymbol{y} = T_o \boldsymbol{r} + S_o G_M \boldsymbol{d} = s^{-1} \left(I + s^{-1}CPK_o\right)^{-1} CPK_o \boldsymbol{r} + s^{-1} \left(I + s^{-1}CPK_o\right)^{-1} CH\boldsymbol{d} \tag{4.22}$$

Introducing feedback from the acceleration state estimates $\hat{\boldsymbol{x}}_{accel}$ (4.23) through the controller K_i to adjust the input to the system plant yields Figure 4.7. The ac-
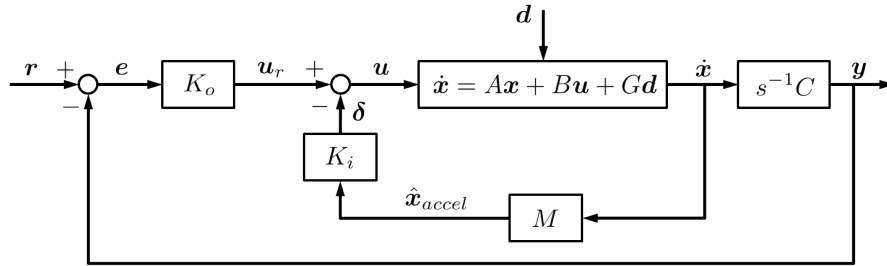
Figure 4.7: State space block diagram with feedback from IMU and distributed accelerometers

celeration state vector generated by the distributed accelerometer array $\boldsymbol{x}_{accel}$, as detailed in Section 2.2.1 (2.30), condenses under the small-perturbation assumptions

87

of a vehicle in hover, i.e. $\Delta q \Delta w \approx \Delta p \Delta q \approx \Delta p^2 \approx \cdots \approx 0$ to

$$\boldsymbol{x}_{accel} \approx M\dot{\boldsymbol{x}} = \begin{bmatrix} \dot{u} & \dot{v} & \dot{w} & \dot{p} & \dot{q} & \dot{r} \end{bmatrix}^T \tag{4.23}$$

where

$$M = \begin{bmatrix} 1 & 0 & 0 & 0 & 0 & 0 & 0 & 0 \\ 0 & 1 & 0 & 0 & 0 & 0 & 0 & 0 \\ 0 & 0 & 1 & 0 & 0 & 0 & 0 & 0 \\ 0 & 0 & 0 & 1 & 0 & 0 & 0 & 0 \\ 0 & 0 & 0 & 0 & 1 & 0 & 0 & 0 \\ 0 & 0 & 0 & 0 & 0 & 1 & 0 & 0 \end{bmatrix} \tag{4.24}$$

Since the disturbances $\boldsymbol{d}$ produces forces and torques that directly affect the acceleration states in $\dot{\boldsymbol{x}}$ through G, (4.10), they can be detected directly via the distributed acceleration scheme. Direct measurements of the translational and rotational accelerations are available from the distributed accelerometers. For this feedback system the input $\boldsymbol{u}$ to the plant is

$$\boldsymbol{u} = \boldsymbol{u}_r - \boldsymbol{\delta} \tag{4.25}$$

where we show just the inner loop acceleration regulation loop in Figure 4.8. Given this feedback, the relations between the reference and disturbance signals and the
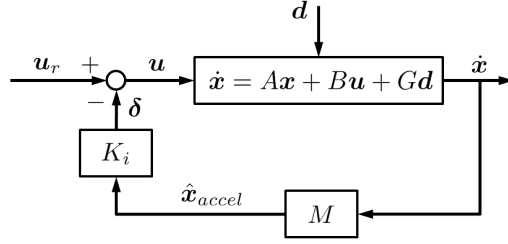
Figure 4.8: State space block diagram of acceleration regulation loop with feedback from distributed accelerometers

system output as previously given in (4.22) are now modified as

$$\boldsymbol{y} = s^{-1}C(I + PK_iM)^{-1}PK_o\left(I + s^{-1}C(I + PK_iM)^{-1}PK_o\right)^{-1}\boldsymbol{r}$$

$$= T_o\boldsymbol{r} \tag{4.26}$$

$$\boldsymbol{y} = s^{-1}\left(I + s^{-1}C(I + PK_iM)^{-1}PK_o\right)^{-1}C(I + PK_iM)^{-1}H\boldsymbol{d}$$

$$= S_oG_{M,d}\boldsymbol{d} \tag{4.27}$$

where the manipulated control in the presence of disturbances $K_{M,d}$ and manipulated plant in the presence of disturbances $G_{M,d}$ are shown in Figure 4.9 and result from block diagram manipulation of Figure 4.7 as detailed in Appendix A Here $S_oG_{M,d}$
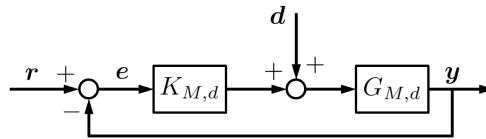
Figure 4.9: Manipulated state space block diagram with acceleration feedback

represents the disturbance sensitivity transfer function, more traditionally written simply as S_oG, as defined in [65], which indicates the effect of exogenous disturbances on the system output.

It is desirable to quantify the performance of our control using the tools of robust analysis. To this end the performance is quantified in terms of the system signals of interest such as the system states, control commands, input disturbances, and noise. As finite energy signals, they therefore belong to the Hilbert space

$$L_2^n(-\infty, \infty) = \{\boldsymbol{f} : (-\infty, \infty) \to \mathbb{R}^n, \int_{\infty}^{\infty} ||\boldsymbol{f}(t)||^2 dt < \infty\} \qquad (4.28)$$

as defined by [66], where the integral in this expression is the L_2 norm. For a stable real rational transfer function G, with input $\boldsymbol{w}$ and output $\boldsymbol{z} = G\boldsymbol{w}$, we may represent the induced norm in L_2^n of G as

$$||G||_{L_2 \to L_2} = \sup_{\boldsymbol{w} \neq 0} \frac{||\boldsymbol{z}||_{L_2}}{||\boldsymbol{w}||_{L_2}} = \sup_{\boldsymbol{w} \neq 0} \frac{||G\boldsymbol{w}||_{L_2}}{||\boldsymbol{w}||_{L_2}} \qquad (4.29)$$

where this expression effectively represents the input energy to output energy gain. The space of stable real rational transfer functions is known as the H_∞ space whose norm is defined as

$$||G||_\infty = \sup_\omega \bar{\sigma}[G(j\omega)] \qquad (4.30)$$

where $\bar{\sigma}$ is the maximum singular value [67]. The induced norm in L_2^n relates to the

H_∞ norm $|| \cdot ||_\infty$ as

$$||G||_{L_2 \to L_2} = ||G||_\infty = \sup_\omega \bar{\sigma}[G(j\omega)] \tag{4.31}$$

where $\bar{\sigma}[G(j\omega)]$ is the maximum singular value of G as a function of frequency ω. Thus the input signal energy to output signal energy gain may be represented via the maximum singular value $\bar{\sigma}$, and may further note that the worst case scenario input energy to output energy gain is given by the H_∞ norm, or equivalently $\sup_\omega \bar{\sigma}$. Therefore when quantifying the performance of a MIMO system in terms of input to output signal energy, e.g. input disturbance signal energy to output signal energy, a small value for $\bar{\sigma}$ is desirable for the transfer function $S_o G$.

Similarly, it is desired that the system output $\boldsymbol{y}$ track the reference $\boldsymbol{r}$ as closely as possible over all frequency at which pilot commands are expected to occur. Therefore, using the same motivation described in the preceding paragraphs, it is desirable that the singular values $\bar{\sigma}$ of transfer function relating $\boldsymbol{r}$ to $\boldsymbol{y}$, i.e. T_o, to be as close to 0 over the expected frequency range of all pilot input commands.

Figure 4.10 displays the simulated response of the 6-DOF system from Section 4.2.1.2 subjected to doublets in roll attitude reference and an impulse gust disturbance, as well as singular value plots of T_o and $S_o G_{M,d}$, for the nominal control (Figure 4.5) and the force feedback control (Figure 4.7). From the singular value plot of $S_o G_{M,d}$ we see improvements in disturbance rejection for high frequency inputs when acceleration feedback is used. This can be seen qualitatively in the time history response where the peak magnitude of the system response to the input

91
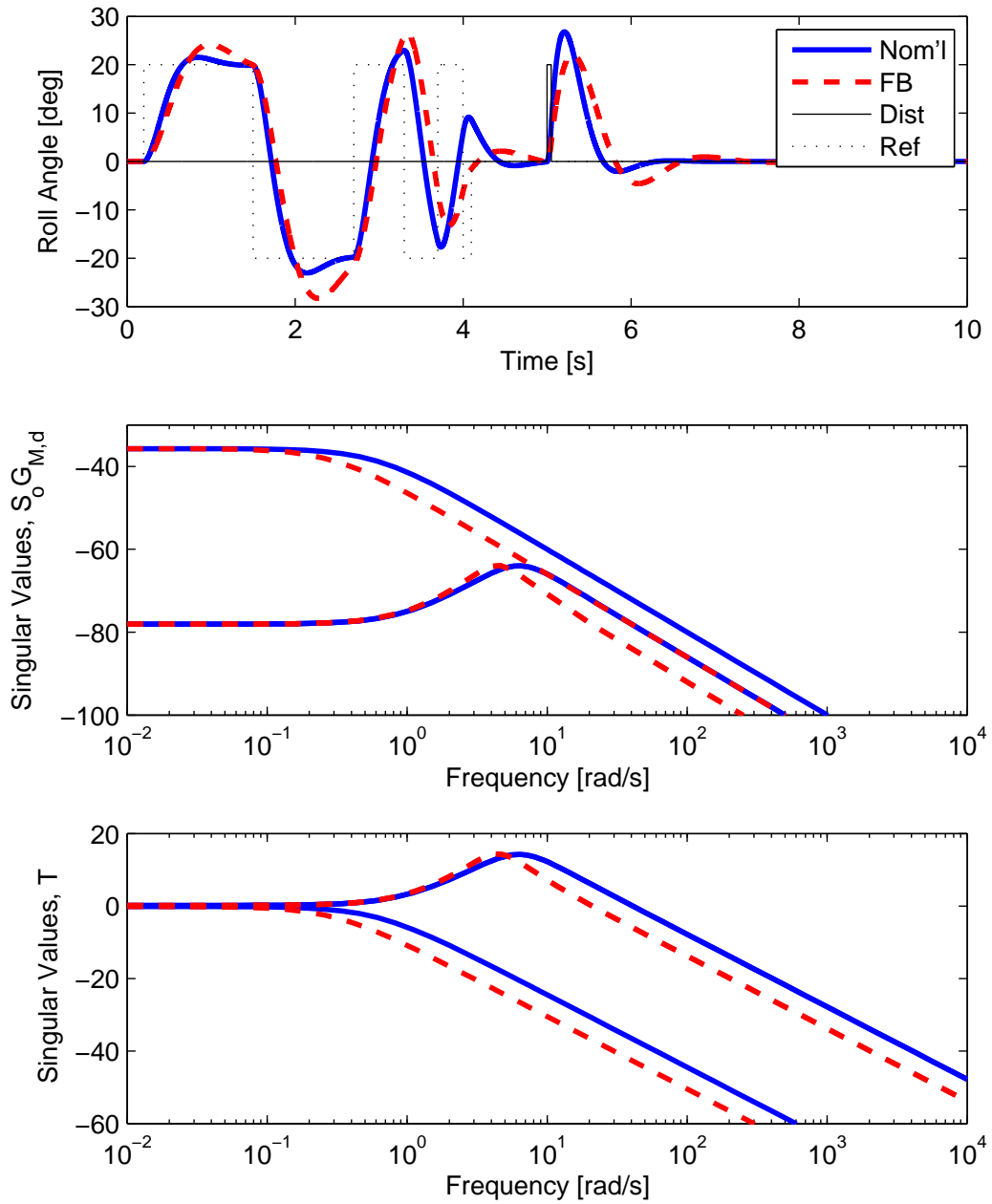
Figure 4.10: Roll response time history for nominal attitude feedback (blue) and force feedback (red), and singular value plots of $S_o G_{M,d}$ and T_o

disturbance is slightly diminished. However, from the tracking response of the step command and the singular value plot of T_o, we see that the closed loop system response to reference commands is slowed for the case of acceleration feedback. This is undesirable in that it yields a less responsive, though only slightly more resilient closed loop system. This characteristic trade-off between disturbance attenuation and system responsiveness was demonstrated with the implementation of this type of control in [68]. This slowed response is expected, as the feedback from the accelerations acts against both unwanted disturbance forces and desired actuation forces. The desired acceleration of the system $\dot{\boldsymbol{x}}_r$ is defined here as the response of the plant to the reference input $\boldsymbol{u}_r$ generated by the attitude controller in the absence of disturbance $\boldsymbol{d}$

$$\dot{\boldsymbol{x}}_r = A\boldsymbol{x} + B\boldsymbol{u}_r \tag{4.32}$$

If it is assumed that the distributed accelerometer array provides the state derivative vector, such that

$$\boldsymbol{x}_{accel} = M\dot{\boldsymbol{x}} \approx \dot{\boldsymbol{x}} \tag{4.33}$$

neglecting the kinematic terms, then substituting this approximation into the closed loop control yields

$$\boldsymbol{u} = \boldsymbol{u}_r - \boldsymbol{\delta} = \boldsymbol{u}_r - K_i M\dot{\boldsymbol{x}} \approx \boldsymbol{u}_r - K\dot{\boldsymbol{x}} \tag{4.34}$$

$$\dot{\boldsymbol{x}} \quad = \quad A\boldsymbol{x} + B\boldsymbol{u} + G\boldsymbol{d} \tag{4.35}$$

$$\approx \quad A\boldsymbol{x} + B(\boldsymbol{u}_r - K_i\dot{\boldsymbol{x}}) + G\boldsymbol{d}$$

$$\approx \quad (I + BK_i)^{-1}(A\boldsymbol{x} + B\boldsymbol{u}_r + G\boldsymbol{d})$$

$$\approx \quad (I + BK_i)^{-1}(\dot{\boldsymbol{x}}_r + G\boldsymbol{d})$$

Thus, while increasing the acceleration feedback K_i attenuates the exogenous distur-
bances, it simultaneously diminishes the desired acceleration response of the system.
The system correspondingly reaches desired states $\boldsymbol{x}_r$ more slowly, thereby produc-
ing a less responsive system. This point is further illustrated by selectively choosing
that $K_i = B^{-1}$, resulting in the closed loop dynamics

$$\dot{\boldsymbol{x}} \quad = \quad A\boldsymbol{x} + B\boldsymbol{u} + G\boldsymbol{d} \tag{4.36}$$

$$\approx \quad A\boldsymbol{x} + B(\boldsymbol{u}_r - B^{-1}\dot{\boldsymbol{x}}) + G\boldsymbol{d}$$

$$\approx \quad A\boldsymbol{x} + B\boldsymbol{u}_r - A\boldsymbol{x} - B\boldsymbol{u} - G\boldsymbol{d} + G\boldsymbol{d}$$

$$\approx \quad B(\boldsymbol{u}_r - \boldsymbol{u})$$

$$\approx \quad B\boldsymbol{\delta}$$

Here it is clear that as the tracking feedback loop tries to drive $\boldsymbol{\delta}$ to zero, and thereby
any disturbances, it also drives the system state derivatives $\dot{\boldsymbol{x}}$ to zero, suppressing
the attitude commands and any desired vehicle motion.

4.2.1.4 Force Adaptive Feedback Design

To compensate for this undesirable behavior of a less responsive system, the acceleration feedback control $\boldsymbol{\delta}$ is redesigned so as not to diminish accelerations induced by the attitude controller command $\boldsymbol{u}_r$. To this end, $\boldsymbol{\delta}$ is reformulated with a feedforward term from the reference command $\boldsymbol{u}_r$ to include a prediction of the actuation force-induced accelerations, mapping it to $\dot{\boldsymbol{x}}$ via B.

$$\boldsymbol{u} = \boldsymbol{u}_r - \boldsymbol{\delta} = \boldsymbol{u}_r - K_i(M\dot{\boldsymbol{x}} - B\boldsymbol{u}_r) \approx \boldsymbol{u}_r - K_i(\dot{\boldsymbol{x}} - B\boldsymbol{u}_r) \qquad (4.37)$$

This control, denoted as force adaptive feedback (FAFB), yields the closed loop dynamics

$$
\begin{aligned}
\dot{\boldsymbol{x}} &\approx A\boldsymbol{x} + B(\boldsymbol{u}_r - K_i(\dot{\boldsymbol{x}} - B\boldsymbol{u}_r)) + G\boldsymbol{d} && (4.38) \\
&\approx (I + BK_i)^{-1}(A\boldsymbol{x} + B\boldsymbol{u}_r + BK_iB\boldsymbol{u}_r + G\boldsymbol{d}) \\
&\approx (I + BK_i)^{-1}(\dot{\boldsymbol{x}}_r + BK_iB\boldsymbol{u}_r + G\boldsymbol{d})
\end{aligned}
$$

Similar to (4.37) the effect of choosing $K_i = B^{-1}$ is illustrated for this case of acceleration feedforward-feedback control.

$$
\begin{aligned}
\dot{\boldsymbol{x}} &\approx A\boldsymbol{x} + B(\boldsymbol{u}_r - B^{-1}(\dot{\boldsymbol{x}} - B\boldsymbol{u}_r)) + G\boldsymbol{d} & (4.39) \\
&\approx A\boldsymbol{x} + B\boldsymbol{u}_r - A\boldsymbol{x} - B\boldsymbol{u} - G\boldsymbol{d} + B\boldsymbol{u}_r + G\boldsymbol{d} \\
&\approx B(2\boldsymbol{u}_r - \boldsymbol{u}) \\
&\approx B(\boldsymbol{u}_r + \boldsymbol{\delta})
\end{aligned}
$$

From this it is clear that as the feedback loop drives $\boldsymbol{\delta}$ to zero, the state dynamics are driven to $\dot{\boldsymbol{x}} = B\boldsymbol{u}_r$. This loop effectively acts to suppress the forces associated with both the system dynamics and disturbances, while passing the actuation forces through to the plant. The control matrix B is not typically square, and thus its inverse must be approximated by the pseudo-inverse $B^{-1} = (B^T B)^{-1} B^T$ when being used for the static control gain matrix K_i. This control strategy is similar to the incremental dynamic inversion control suggested by [44] and [45]. Similarly to these techniques, our proposed control needs only measurement of the accelerations of the vehicle $\hat{\boldsymbol{x}}_{accel}$, a sufficiently high fidelity estimate of the control authority B, and the actuator command generated by the attitude controller $\boldsymbol{u}_r$. The linear dynamic inversion controller presented in [69] is also similar to this, but additionally requires simulation of the system dynamics and therefore a higher fidelity estimate of the dynamic matrix A than is required by the control proposed here.

The block diagram for this inner loop force adaptive control system is depicted in Figure 4.11. This method of adapting the control command with feedback from
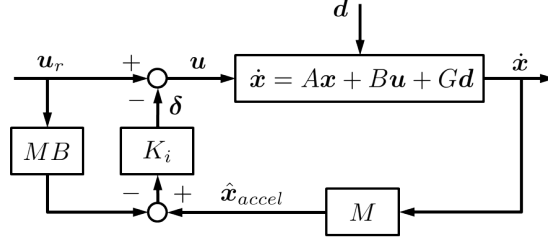
Figure 4.11: State space block diagram of command tracking loop with feedback from distributed accelerometers and feedforward from actuator command

acceleration sensing and feedforward from the command is applied to the 6-DOF system described by (4.14)-(4.14). The assumption (4.33) guided the selection of this control design, however, for the full 6-DOF system this assumption must be relaxed, as the output vector includes attitude states that must be removed from the feedforward control component. The acceleration state estimate provided by the distributed accelerometers is not precisely $\dot{\boldsymbol{x}}$, but is instead given as a function of the output vector, $\hat{\boldsymbol{x}}_{accel} = M\dot{\boldsymbol{x}}$. We must modify the expression for the control command to be dimensionally consistent by replacing B with MB in the feedforward control component, as this is the actual mapping between the input control $\boldsymbol{u}$ and the acceleration state vector $\hat{\boldsymbol{x}}_{accel}$.

$$\boldsymbol{u} = \boldsymbol{u}_r - \boldsymbol{\delta} = \boldsymbol{u}_r - K_i(M\dot{\boldsymbol{x}} - MB\boldsymbol{u}_r) \qquad (4.40)$$

Correspondingly the control gain matrix is chosen as

$$K_i = ((MB)^T MB)^{-1}(MB)^T \qquad (4.41)$$

97

This control loop structure is shown in Figure 4.12.
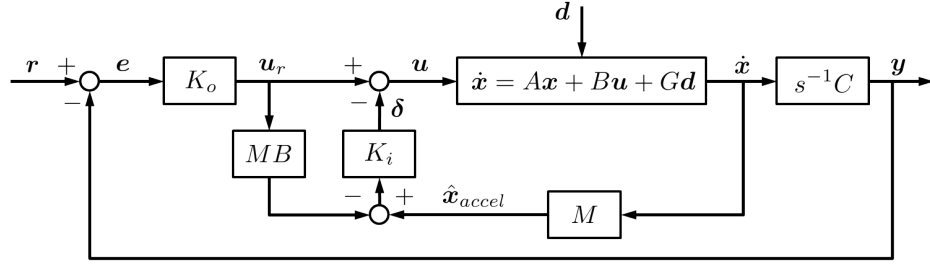
Figure 4.12: State space block diagram of attitude tracking loop with feedback-feedforward from accelerometers

4.2.1.5   Force Adaptive Feedback Robust Analysis

Given this force adaptive feedback with feedforward (FAFB) control structure, block diagram manipulations detailed in Appendix A were performed to transform the system into the form of Figure 4.13. This generic structure was used to develop
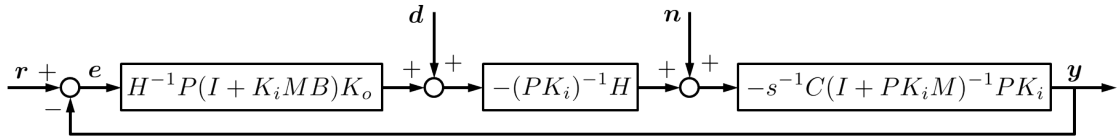
Figure 4.13: Manipulated state space block diagram with force adaptive feedback

typical robust analysis system structures. For the case of a noiseless system subjected to exogenous disturbances, the representation may be simplified as in Figure 4.14 where the transfer functions that comprise the loop are instead defined as

$$K_{M,d} = H^{-1}P(I + K_iMB)K_o \tag{4.42}$$
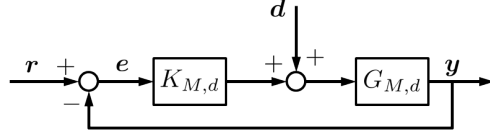
Figure 4.14: Manipulated noiseless state space block diagram with force adaptive feedback

$$G_{M,d} = s^{-1}C(I + PK_iM)^{-1}H \tag{4.43}$$

Using the definitions of L_o, S_o, and T_o from (4.19), (4.20), and (4.21), useful transfer function matrix relationships are calculated. The transfer function T_o that maps references $\boldsymbol{r}$ to outputs $\boldsymbol{y}$ in (4.26) becomes

$$\begin{aligned}
\boldsymbol{y} &= s^{-1}C(I + PK_iM)^{-1}P(I + K_iMB)K_o\left(I + s^{-1}C(I + PK_iM)^{-1}P(I + K_iMB)K_o\right)^{-1}\boldsymbol{r} \\
&= T_o\boldsymbol{r} \tag{4.44}
\end{aligned}$$

Additionally, the transfer function $S_oG_{M,d}$, mapping disturbance $\boldsymbol{d}$ to output $\boldsymbol{y}$ in (4.27) becomes

$$\begin{aligned}
\boldsymbol{y} &= s^{-1}\left(I + s^{-1}C(I + PK_iM)^{-1}P(I + K_iMB)K_o\right)^{-1}C(I + PK_iM)^{-1}H\boldsymbol{d} \\
&= S_oG_{M,d}\boldsymbol{d} \tag{4.45}
\end{aligned}$$

The same conditions of roll reference doublets and a roll gust impulse disturbance were simulated for the 6-DOF system, as in Figure 4.10, now with the FAFB control. The response time history and singular value plots for $S_oG_{M,d}$ and T_o are shown in

Figure 4.15. The downward shift of the singular value plot of $S_o G_{M,d}$ represents attenuation of disturbances across all frequencies, which indicates a very effective disturbance rejection mechanism that is capable of resilience to a very wide class of disturbances. Additionally, the closeness of the singular value plot of T_o of the FAFB control case to the nominal attitude control case indicates that there is no degradation of reference tracking at high frequencies. Furthermore, at low frequencies the singular value plot of T_o is closer to 0 dB for the FAFB case than for the nominal case, indicating an improvement in low frequency reference tracking. From both the response time history and the singular value plots it is clear that the selection of the control adaptation law in (4.40) produces more accurate, responsive tracking of the nominal control commands while simultaneously attenuating exogenous disturbances to a more significant degree.
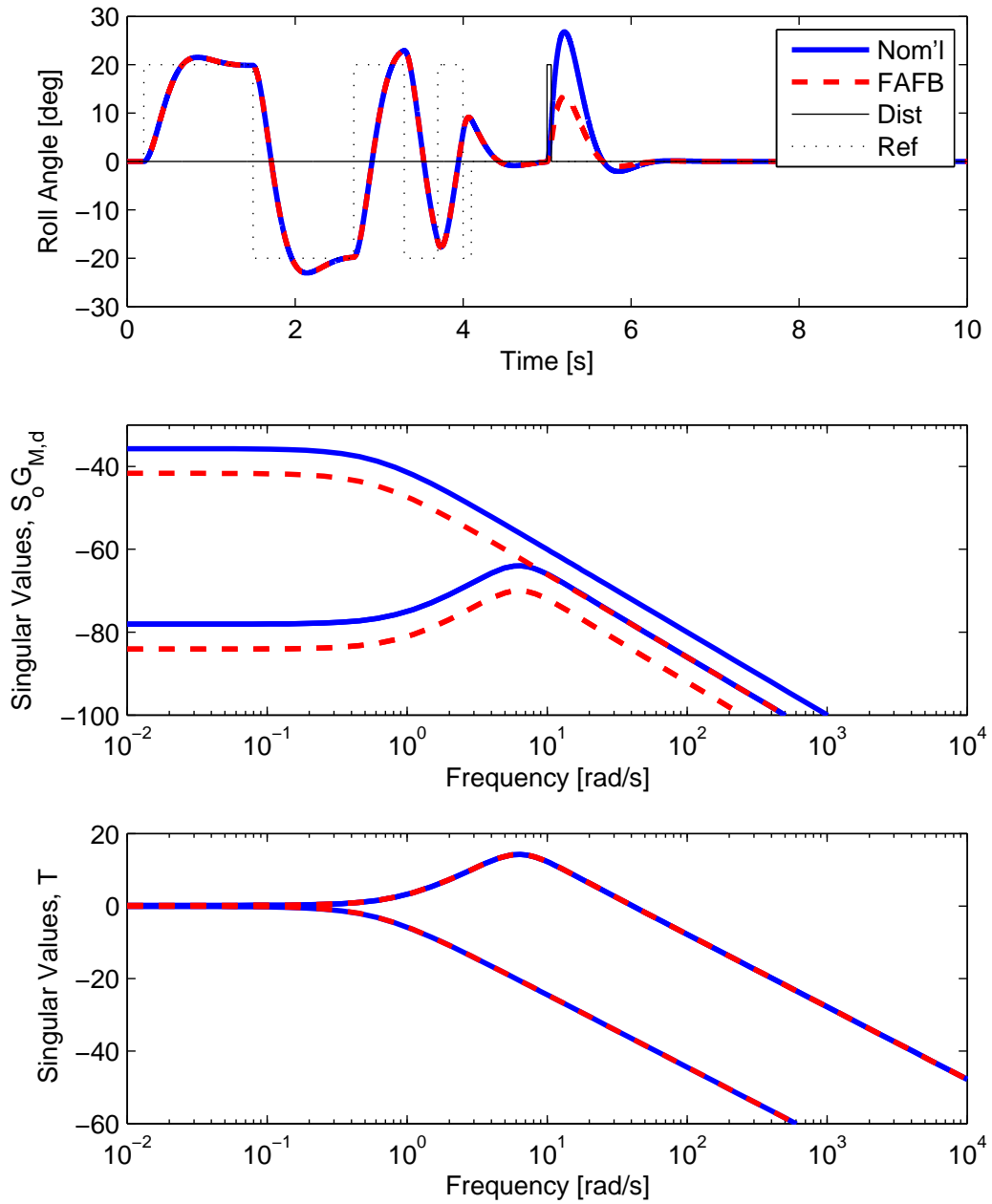
Figure 4.15: Roll response time history for nominal attitude feedback (blue), force-adaptive feedback with feedforward (red) and singular value plots of $S_oG_{M,d}$ and T_o

Loop shaping filters may be also applied to the controller K_i to amplify or attenuate its response for desired regions of the frequency spectrum. Figure 4.16 displays comparative singular value plots for $S_oG_{M,d}$ and T_o the nominal attitude controller and the FAFB control with low-pass and high-pass shaping filters applied to K_i. From this plot it is clear that including dynamic filtering in the controller K_i serves to diminish or improve disturbance rejection over the frequency that is respectively attenuated or amplified by the shaping filter. Specifically, this is shown as the singular value curves for disturbance sensitivity $S_oG_{M,d}$ of the filtered controller transfer functions moves up or down in magnitude relative to the unfiltered FAFB control. It may be also noted that the reference tracking transfer function T_o singular value curves, and thus the tracking performance, is unaffected by the filtering.

This result illustrates that if disturbances to the system are expected to occur over a range of frequencies, then a shaping filter in K_i with amplification at that frequency range and attenuation elsewhere may be a desirable design choice. Bode plots for the respective shaping filters are shown in Figure 4.17. It is noted that both filters in this case have 0dB gains at 5 rad/s, and maximum gains of 10 (20dB).
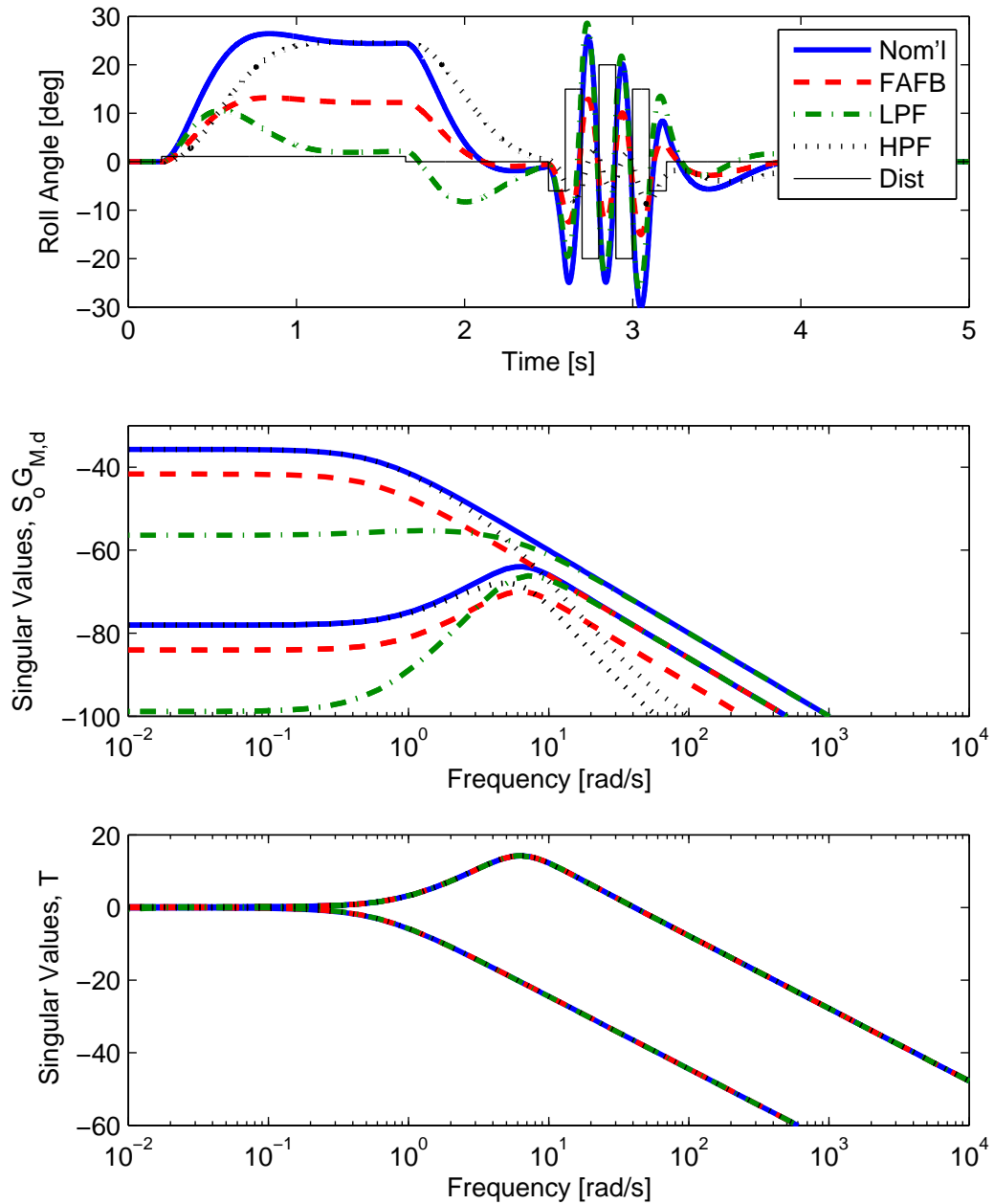
Figure 4.16: Roll response time history for nominal attitude feedback (blue) and (a) force-adaptive feedback with feedforward (red) with (b) low-pass shaping filter (green) and (c) high-pass shaping filter (black), and singular value plots of $S_oG_{M,d}$ and T_o
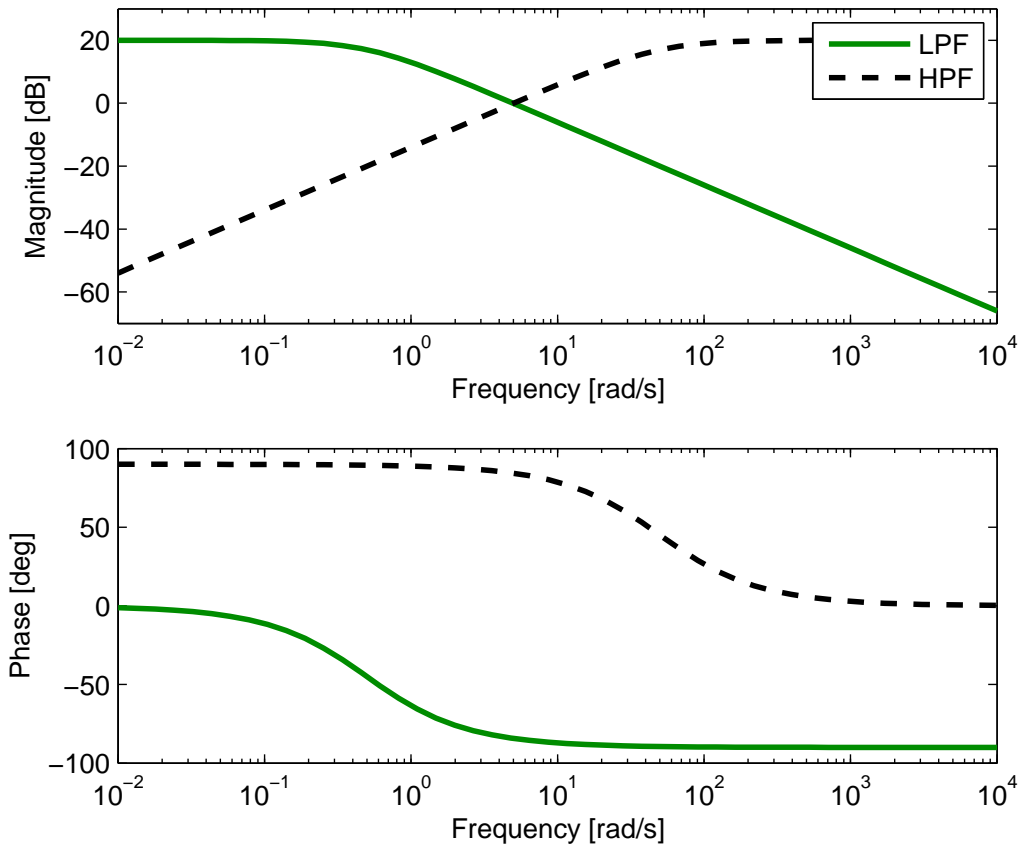
Figure 4.17: Bode plots for low-pass shaping filter (green) and high-pass shaping filter (black) applied to force-adaptive feedback control in simulation for Figure 4.16

Using the manipulated system shown in Figure 4.13, the impact of noise in the acceleration estimate $\hat{\boldsymbol{x}}_{accel}$ may also be analyzed. Assuming a system with such noise, but without an exogenous disturbance $\boldsymbol{d}$, the system may be equivalently represented in the typical robust analysis structure as shown in Figure 4.18
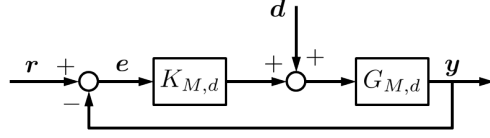
Figure 4.18: Manipulated noiseless state space block diagram with force adaptive feedback

where the transfer functions that comprise the loop are alternatively defined as

$$K_{M,n} = -(PK_i)^{-1}P(I + K_i MB)K_o = -K_i^{-1}(I + K_i MB)K_o \tag{4.46}$$

$$G_{M,n} = -s^{-1}C(I + PK_i M)^{-1}PK_i \tag{4.47}$$

Using the formulation of L_o, S_o, and T_o from (4.19), (4.20), and (4.21), the transfer function relating accelerometer estimate noise $\boldsymbol{n}$ to system output $\boldsymbol{y}$ is defined as $S_o G_{M,n}$ and given by

$$
\begin{aligned}
\boldsymbol{y} &= -s^{-1}\left(I + s^{-1}C(I + PK_i M)^{-1}P(I + K_i MB)K_o\right)^{-1}C(I + PK_i M)^{-1}PK_i \boldsymbol{n} \\
&= S_o G_{M,n} \boldsymbol{n} \tag{4.48}
\end{aligned}
$$

The transfer function relating reference $\boldsymbol{r}$ to output $\boldsymbol{y}$, that is T_o is unchanged by this formulation and remains equivalent to (4.44). Figure 4.19 illustrates the effect of this additive noise in the acceleration estimate from the distributed accelerometers on the roll response is shown, with comparison between the nominal attitude control case and the force-adaptive feedback cases with and without noise. The severity of

105

the noise is also depicted in Figure 4.19. It is clear from the time histories that even without loop shaping filters, the throughput of noise to the roll state is largely attenuated. This qualitative result is confirmed by the singular value plot in Figure 4.19, which shows a roll off in noise at approximately 1 rad/s. These results illustrate the robustness of the force adaptive feedback structure in the presence of exogenous disturbances, as well as measurement noise.
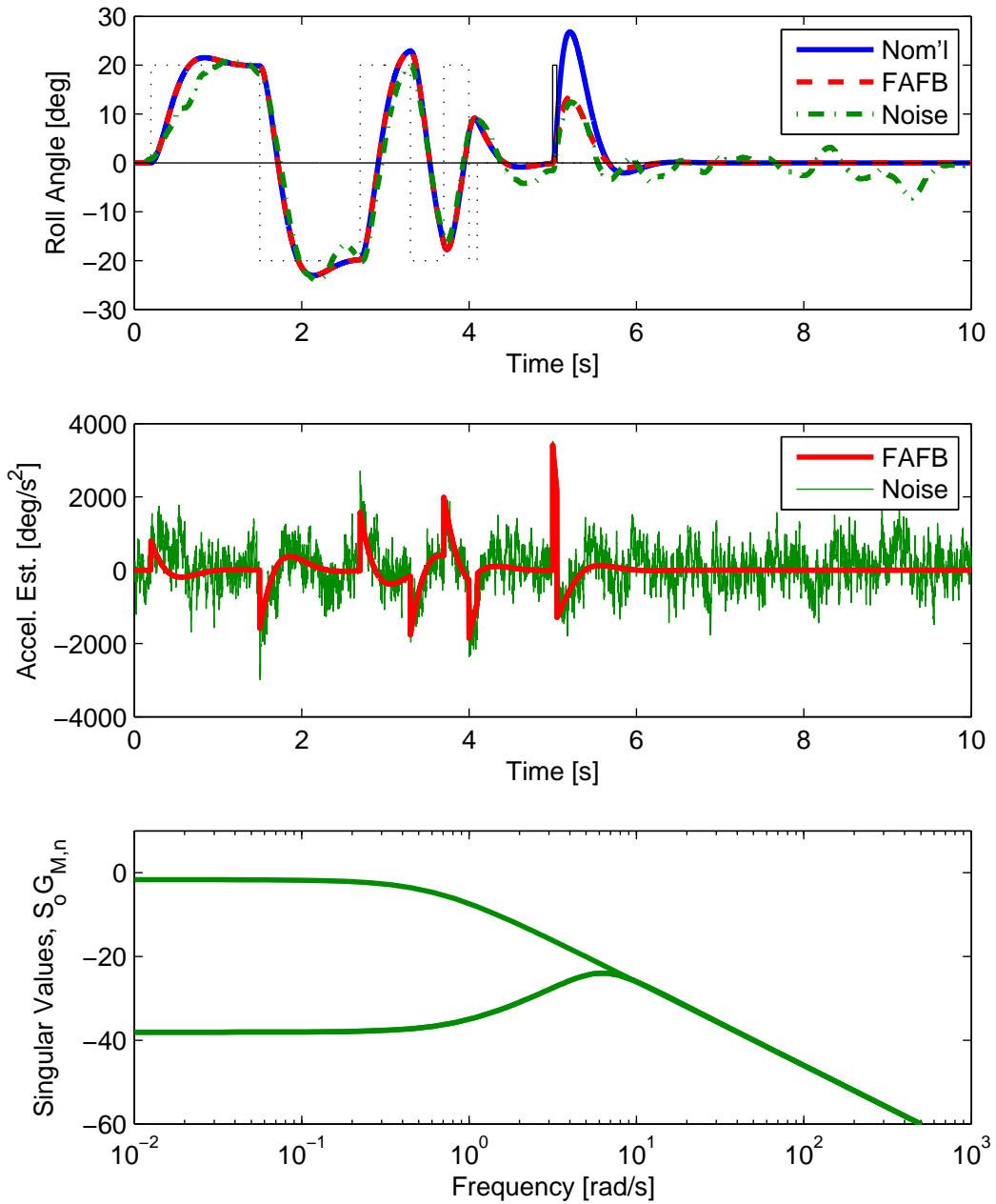
Figure 4.19: (a) Response time history for nominal controller (blue) force adaptive feedback without noise (red) and with noise (green), time history of the estimated roll acceleration state for noiseless (red) and noisy (green) cases, and singular value plot of $S_oG_{M,n}$

Having characterized the robustness of the force adaptive feedback architecture for a prototypical quadrotor 6-DOF model it is desired to test its performance on the DJI FlameWheel 330 described in Section 4.1.1. To perform this characterization and testing, the quadrotor must first be modeled about hover.

4.2.2 Quadrotor System Identification

An extensive literature on system identification techniques exists, including two thorough works on the aircraft system identification [58], [70]. The generalized structure of the system we desire to implement on the quadrotor sUAS is shown in Figure 4.20. Nominally, the existing attitude sensing and control system takes in a pilot reference attitude state x_r and inputs to the IMU sensors from the true attitude state of the vehicle x, and outputs an actuator command u designed to drive x to x_r. The actuator-aero dynamic system encompasses all actuator dynamics and vehicle aerodynamics. The input to this system is the actuator command u and outputs are actuator force and torque. The output of this system is then corrupted by additive disturbance force and torque d, such as a gust or actuator error, yielding a total force and torque, F, τ, that is applied to the vehicle to perform control maneuvers. This total force is the input to the vehicle plant system, which outputs the vehicle state that we desire to control x. The force-adaptive sensing and control system, shown in orange, is introduced to account for the disturbances d by modifying the input to the actuator-aero dynamic system u. This inner feedback loop acts to drive the actual total force and torque to the desired force and torque as commanded by

u, thereby forming a reference tracking loop.
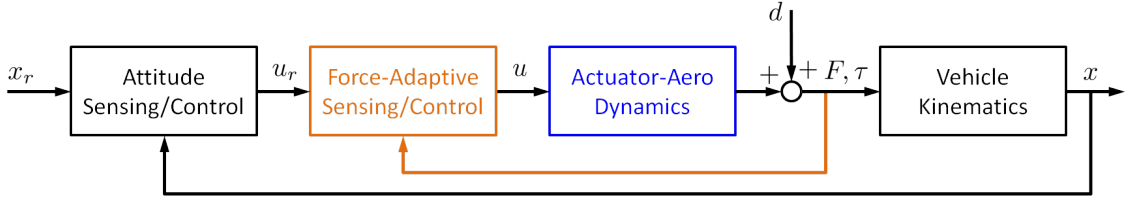
Figure 4.20: Generalized block diagram of quadrotor system, force-adaptive feedback control from distributed acceleration sensor array shown in orange.

4.2.2.1 1-DOF Roll Modeling

As with the disturbance rejection with ocellar sensing described in Section 4.1, the scope of this control design and implementation is limited to a single degree of freedom to demonstrate the disturbance rejection performance without implementing a full 6-DOF MIMO control. Here only the SISO roll degree-of-freedom system is modeled on the quadrotor sUAS (Figure 3.15), leaving other out-of-plane rotational states to be regulated to zero by existing control systems, assuming

$$\theta = \psi \approx 0 \tag{4.49}$$

and therefore $q = r = 0$. Though the out-of-plane states are not physically constrained to be zero, the axisymmetric airframe and actuation architecture of a quadrotor provides largely decoupled dynamics, that is, motions about the pitch and yaw axes do not induce motion about the roll axis. This assumption yields several simplifying results. First, we only need to model the system as a function

of the roll Euler angle ϕ and its derivatives. Correspondingly, from inspection of (2.29), (2.31), and (4.49) the following torque equation is yielded

$$\tau_x = I_x \dot{p} \tag{4.50}$$

Thus, only the roll torque τ_x in (2.26), which is assumed to be a function only of $\dot{p}$, is considered as the input to the vehicle. Given the assumption (4.49), the kinematic relation between ϕ and p, typically expressed as

$$\dot{\phi} = p + q \sin(\phi) \tan(\theta) + r \cos(\phi) \tan(\theta) \tag{4.51}$$

condenses to

$$\dot{\phi} = p \tag{4.52}$$

which yields, with (4.50), the plant transfer function

$$\phi = \frac{1}{I_x s^2} \tau = \frac{1}{I_x s^2} I_x \dot{p} \tag{4.53}$$

The distributed accelerometer array produces estimates of the defined acceleration state vector $\boldsymbol{x}$ (2.30), with the only rotational state not equal to zero being $\dot{p}$. Given (4.50), (4.53), and the fact that the distributed acceleration sensor provides direct estimates of $\dot{p}$, we may simply remove the roll inertia I_x in (4.53), which is effectively a constant scaling factor. Thus, we represent the vehicle plant system

110

G_P, with input $\dot{p}$ and output ϕ, as a simple kinematic relationship

$$G_P(s) = \frac{1}{s^2} \qquad (4.54)$$

It is also practical to model the system in terms of $\dot{p}$ rather than τ, because the Vicon™ motion capture system is capable of directly measuring kinematic states and not torque.

In identifying the quadrotor SISO roll dynamic system, we took advantage of the open source avionics integrated on the vehicle, which allows for direct inspection of the controllers being implemented. This reduces the number of unknown systems and parameters that must be estimated with system identification and thus improves the fidelity of our modeling and the performance of resulting model-based controllers. Through this direct inspection of the flight software, the existing roll attitude control system was reverse-engineered. To identify G_{C_1} and G_{C_2} we compared the measurements of the onboard IMU sensors, provided in integer counts (LSB), to external measurements of ϕ and p, expressed respectively in rad and rad/s, from the Vicon™ system for input open loop vehicle egomotions. The three attitude controller transfer functions G_{C_1}, G_{C_2}, and G_{C_3}, shown in block diagram form in Figure 4.21, were identified to be

$$G_{C_1}(s) = 20439 \equiv K_1, \ G_{C_2}(s) = 5638s \equiv K_2 s, \ \text{and} \ G_{C_3}(s) = 0.15 \equiv K_3 \quad (4.55)$$

The output of G_{C_3} is the actuator command u, so we may represent the attitude

111
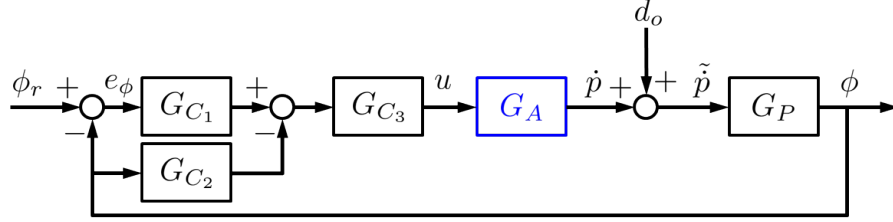
Figure 4.21: Block diagram of identified quadrotor roll SISO system with output angular acceleration disturbance d_o. Unknown actuator-aero dynamic model G_A (blue).

control as a transfer function relating roll angle ϕ and roll angle reference ϕ_r to actuator command as

$$u = 0.15\left(20439(\phi_r - \phi) - 5638s\phi\right) \tag{4.56}$$

The only remaining unidentified component of quadrotor roll dynamic model is the actuator-aero dynamic system G_A, shown in blue in Figure 4.21. As defined, this system maps actuator commands u, in integer counts (LSB), to roll angular acceleration $\dot{p}$, in rad/s². Flight tests were performed to identify this system where vehicle motions were excited via commanded inputs, while the actuator command $\tilde{u}$ was recorded simultaneously with measurements of $\dot{p}$ via the Vicon™ system, where $\tilde{u} = u + d_i$ for input actuator disturbance d_i (Figure 4.22). In order to better identify G_A, the system was excited using inputs at two different points within the system. Input doublet commands were sent alternatively as the roll angle reference ϕ_r and input actuator disturbance d_i. Traditionally only reference inputs, such as ϕ_r, are used to excite the vehicle for system identification. By introducing excitation

inputs in the form of additive actuator disturbance d_i after the control command is computed, the dynamics of G_A are more fully excited. This reduces the effect of the attitude controller to suppress the natural dynamics of G_A, while still allowing for stabilizing flight control. Simply setting the computed control command u to zero with the input disturbance d_i being the only input to G_A produces unstable flight. Therefore, including stabilizing feedback is necessary for system identification flight tests.
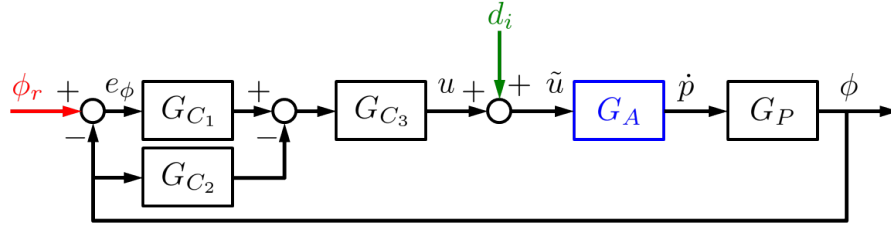
Figure 4.22: Block diagram of identified quadrotor roll SISO system with input actuator disturbance d_i (green) and roll angle reference ϕ_r (red). Unknown actuator-aero dynamic model G_A shown (blue).

With the identified plant and controller dynamic systems in (4.54) and (4.55), and the loop structure in Figure 4.22, we express the input sensitivity transfer function $S_i(s)$ as

$$S_i(s) = \frac{G_P G_A}{1 + G_P G_A G_{C_3}(G_{C_1} + G_{C_2})} = \frac{1}{s^2 G_A^{-1} + K_3(K_1 + K_2 s)} \tag{4.57}$$

with input d_i and output ϕ. Similarly, we express the complementary sensitivity

transfer function $T(s)$ as

$$T(s) = \frac{G_P G_A G_{C_3} G_{C_1}}{1 + G_P G_A G_{C_3}(G_{C_1} + G_{C_2})} = \frac{K_1 K_3}{s^2 G_A^{-1} + K_3(K_1 + K_2 s)} \tag{4.58}$$

with input ϕ_r and output ϕ. The response of the output roll angle ϕ may be fully, explicitly expressed as

$$\phi = T\phi_r + S_i d_i \tag{4.59}$$

Time domain output-error estimation techniques, as described in [58], were implemented to refine the estimated value of coefficients in G_A. Generally, this iterative technique optimizes the free parameters of a modeled system $\hat{G}$ so as to minimize the residual ν between the true output y and the modeled output $\hat{y}$, where $y = Gu$, $\hat{y} = \hat{G}u$, and $\nu \equiv y - \hat{y}$, for input u. This was simultaneously performed for the transfer functions T and S_i. For each iteration, a postulated model $\hat{G}_A$ yields a S_i and T from (4.57)-(4.58), each of which yields a corresponding simulated roll angle, $\hat{\phi}$. These simulated $\hat{\phi}$ are compared to true roll angle measurements ϕ, collected via Vicon™ for each of the test cases depicted in Figure 4.22. The residual signal ν for each of these cases is minimized with subsequent iterations, by varying the parameters in $\hat{G}_A$, until a tolerance is reached. The resulting $\hat{G}_A$ is the model that best fits the true G_A. The output-error parameter identification resulted in the estimated actuator-aero dynamic model

$$\hat{G}_A(s) = \frac{0.486s^3 + 0.403s^2 + 0.201s + 0.0233}{s^4 + 11.0s^3 - 45.8s^2 - 60.3s + 710} \tag{4.60}$$

This system has a pair of unstable complex poles in the right half of the complex plane (RHP), which is consistent with our observation of unstable flight when the feedback control command u is set to zero. Figure 4.23 shows the time history of the true and modeled roll angles, ϕ and $\hat{\phi}$, for the sensitivity transfer function S_i, with doublet inputs to d_i and $\phi_r = 0$. Similarly, Figure 4.24 shows ϕ and $\hat{\phi}$ for the complementary sensitivity transfer function T, with doublet inputs to ϕ_r and $d_i = 0$. These plots illustrate a good time-domain fit between the modeled system and the
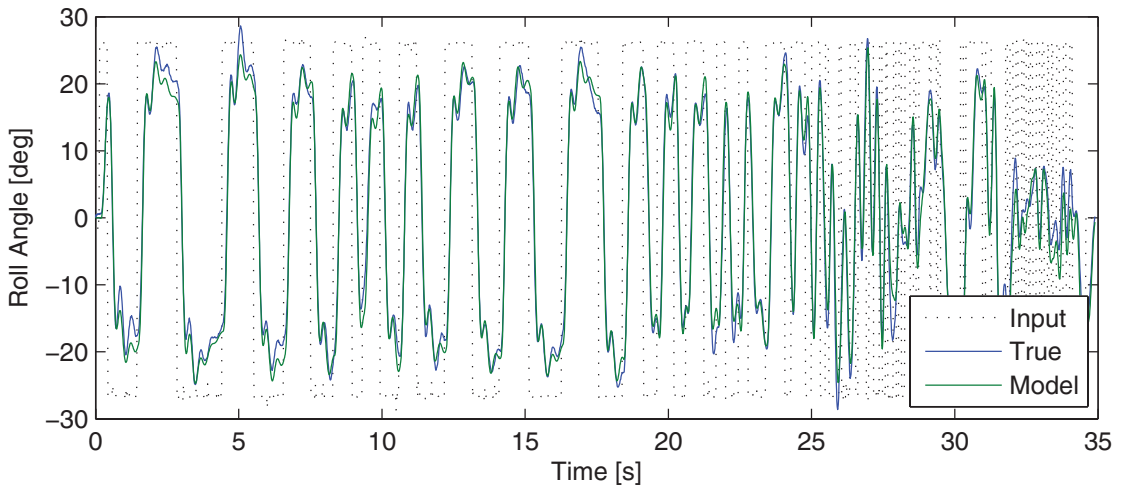
Figure 4.23: Time history comparison for true (blue) and modeled (green) roll angle output ϕ from sensitivity function S_i. Input actuator disturbance d_i shown (black, dotted), with $\phi_r = 0$.

measured output data. The Bode plots for estimated transfer functions S, T, and G_A are shown in Figure 4.25 with corresponding spectral Bode plots. Corresponding magnitude-squared coherence plots are also shown, indicating the frequency regions over which the input-output relationship for the respective transfer function is well represented by a linear system. These indicate the goodness of fit of the estimated model $\hat{G}_A$ (4.60) in the frequency domain. Given the results shown in Figures 4.23-

115
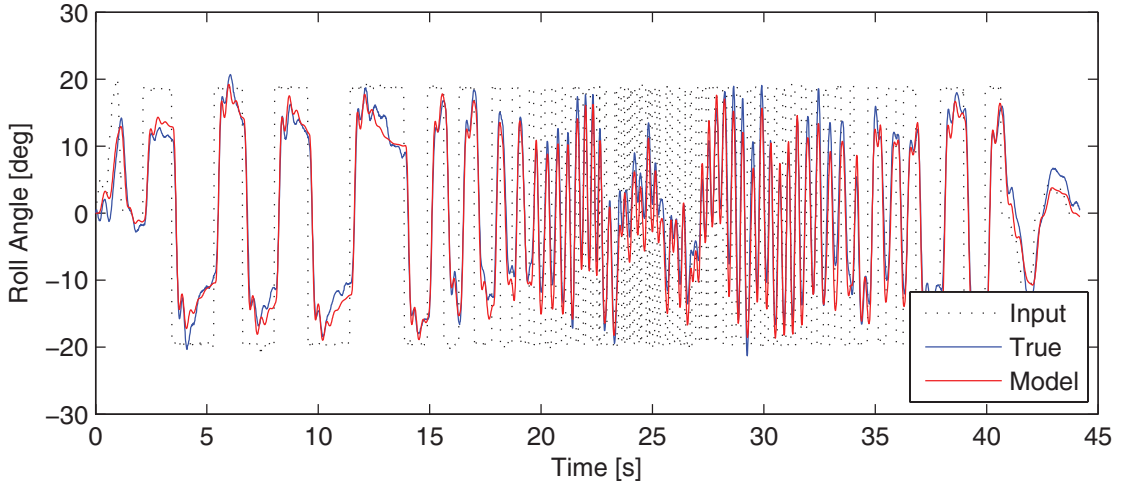
Figure 4.24: Time history comparison for true (blue) and modeled (red) roll angle output ϕ from complementary sensitivity function T. Input roll angle reference ϕ_r shown (black, dotted), with $d_i = 0$.

4.25, it is concluded that the actuator-aero dynamic model identified in (4.60) is a relatively accurate SISO model for the true dynamic system.

4.2.2.2   2-DOF Reduced-Order Modeling

The model identified in Section 4.2.2.1 yields a high fidelity response when compared to the actual flight data. It is desirable to simultaneously reduce the complexity of this single degree-of-freedom model, expand to an additional translational degree of freedom, and put the system into a form conducive with the state space implementation of the force adaptive feedback control detailed in Section 4.2.1.4. To accomplish these goals, a reduced order system identification modeling for the 2-DOF translational and rotational system with state vector $\boldsymbol{x}$, control u,
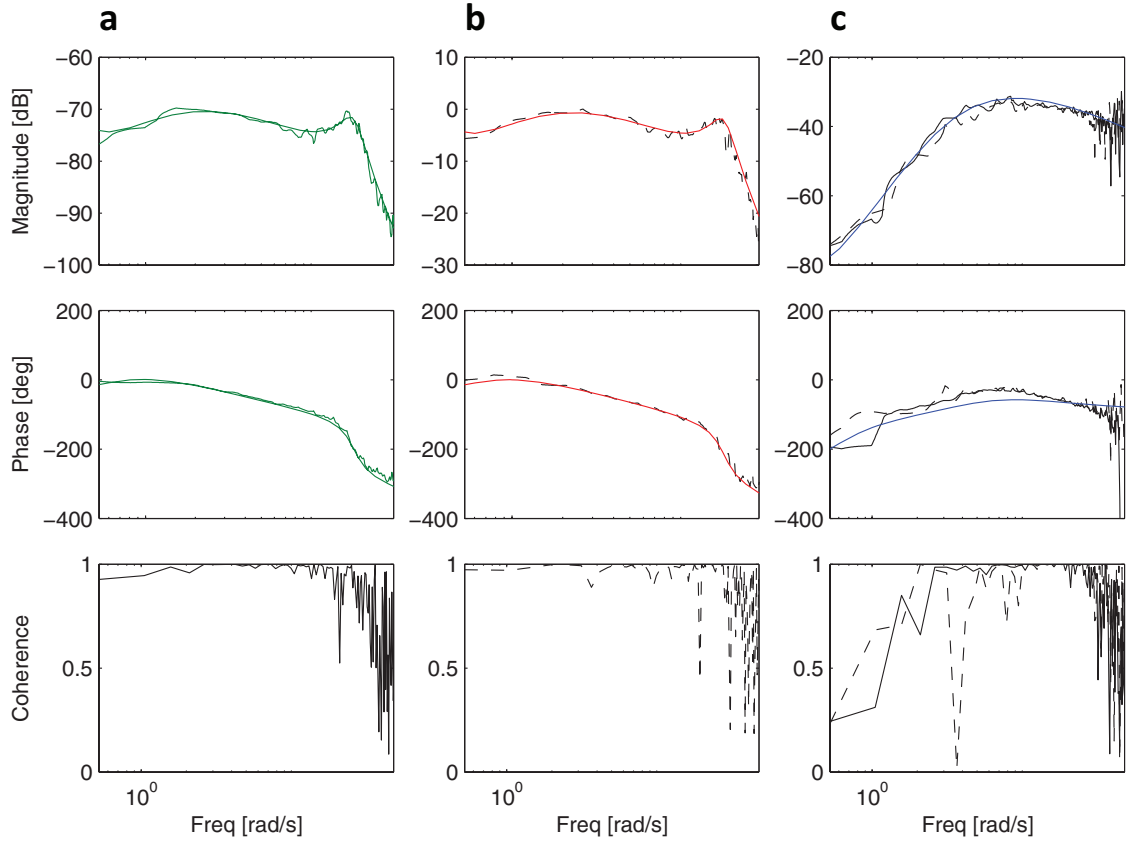
Figure 4.25: Bode and magnitude squared coherence plots of transfer function process and spectral models. (a) process model (green) and spectral model (black) for $S(s)$, (b) process model (red) and spectral model (black, dashed) for $T(s)$, and (c) process model (green) and spectral models for $G_A(s)$ for inputs from d_i (black, solid) and ϕ_r (black, dashed).

and disturbance vector $\boldsymbol{d}$ was performed

$$\boldsymbol{x} = \begin{bmatrix} v & p & \phi \end{bmatrix}, \quad u = u_R, \quad \boldsymbol{d} \begin{bmatrix} d_v & d_p \end{bmatrix} \tag{4.61}$$

The postulated model for this system is of the form

$$\dot{\boldsymbol{x}} = \begin{bmatrix} Y_v & Y_p & g \\ L_v & L_p & 0 \\ 0 & 1 & 0 \end{bmatrix} \boldsymbol{x} + \begin{bmatrix} Y_R \\ L_R \\ 0 \end{bmatrix} u + \begin{bmatrix} -Y_v & -Y_p \\ -L_v & L_p \\ 0 & 0 \end{bmatrix} \boldsymbol{d} \qquad (4.62)$$

As in Section 4.2.2.1, output-error system identification techniques were utilize to estimate the free parameters in (4.62). It is imposed that the gravitational constant g and the kinematic relationship in the last row of the A matrix are fixed values, with all remaining terms free to be modified by the estimation algorithm. Here we assume the negative relationship between the aerodynamic parameters in A and G. Since the open loop dynamics of the quadrotor are unstable we must simulate the closed loop system while performing output-error parameter estimation, utilizing the identified control law (4.56). In Figure 4.26, the comparative plots of the time histories for the true and modeled states v, p, and ϕ. From this plot we see high fidelity alignment between the flight data and the model, especially for a reduced-order model.

For this state space representation, the matrices C and M as presented in Figure 4.12, are given by

$$C = \begin{bmatrix} 0 & 1 & 0 \\ 0 & 0 & 1 \end{bmatrix}, \quad M = \begin{bmatrix} 1 & 0 & 0 \\ 0 & 1 & 0 \end{bmatrix} \qquad (4.63)$$
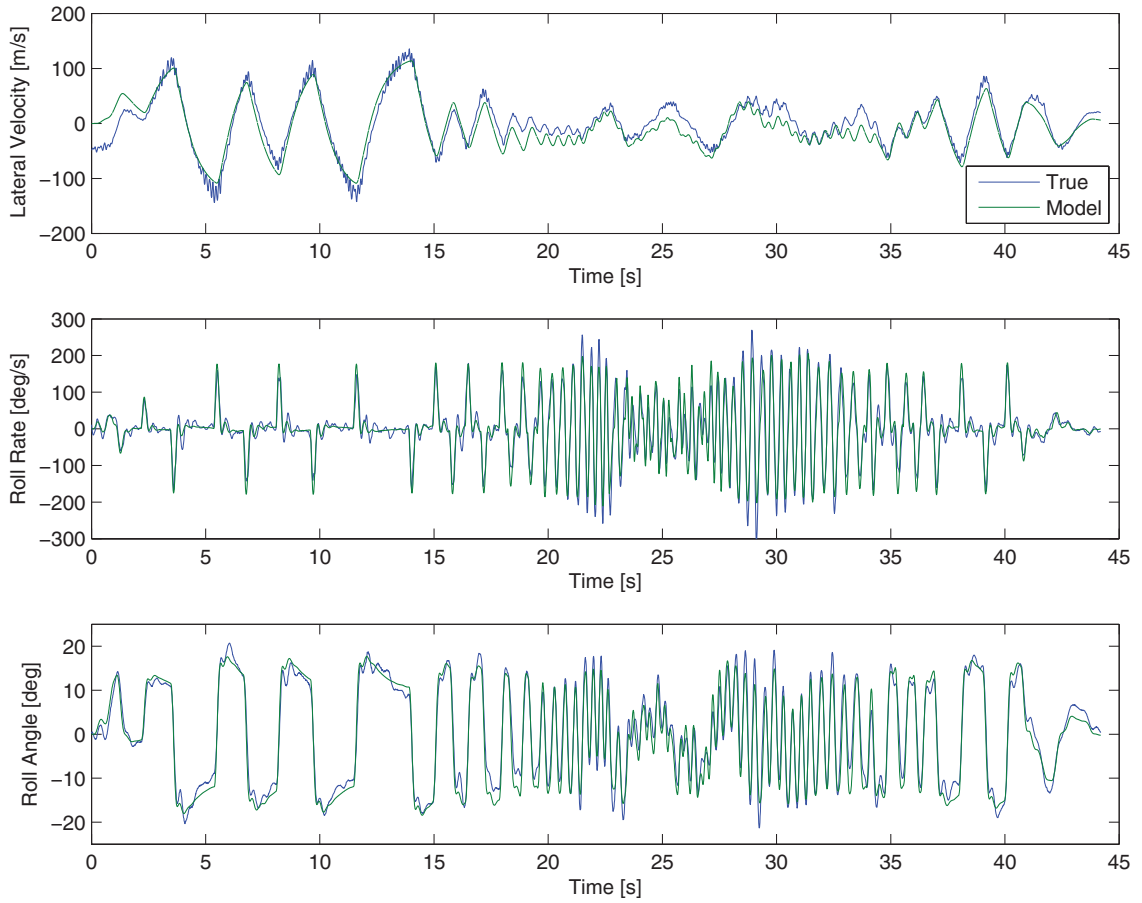
Figure 4.26: Comparison between true and modeled 2-DOF lateral reduced-order model quadrotor system for states v, p, and ϕ

The values for the identified parameters of the 2-DOF system are given in Table 4.3.

Table 4.3: Identified quadrotor 2-DOF lateral reduced-order model parameters (4.62)

Parameter Name	Parameter Value	Cramer Rao Bound ($\times 10^{-3}$)	Units
Y_v	-0.821	0.34	s^{-1}
Y_p	-0.437	2.5	s^{-1}
Y_R	0.000205	0.018	m/s^2/LSB
L_v	-2.52	1.1	s^{-1}
L_p	2.20	0.36	s^{-1}
L_R	0.0184	0.0001	m/s^2/LSB

Converting the parameter L_R from magnitude to dB yields a value of (-34.7dB). This aligns well with the maximum magnitude in the Bode plot of the transfer function $G_A(s)$ in Figure 4.25. Highly accurate estimates of all the parameters in Table 4.3 is not necessary. Rather, it is most important that the parameters that comprise the control authority matrix, B, be most accurate. This is promising, as both Y_R and L_R have the lowest Cramer Rao bounds, and thus can be considered more accurate. To further characterizing the system, the avionics attitude control loop period was identified to be approximately between 12 and 20 ms. The reading of the accelerometer array, estimation of acceleration state vector $\boldsymbol{x}_{accel}$, and computation of the force-adaptive control was estimated to take less than 2 ms within the avionics hardware.

4.2.3 Implementation and Performance Analysis

4.2.3.1 Simulated Performance Analysis

The force adaptive feedback control was then formulated based on this identified system model, (4.41), and Figure 4.12. Given this estimated 2-DOF system and this corresponding control law, the system response may be simulated for reference tracking and disturbance rejection. Figures 4.27 and 4.28 depict this simulated response for the cases of force feedback and force adaptive feedback-feedforward control (FAFB), respectively, as defined in Figures 4.7 and 4.12. The nominal control is shown in these figures in blue, and singular value plots are included to illustrate the improvements in disturbance rejection in the time domain and as a function of signal frequency for each control case. Clearly from these plots, the force-adaptive feedback control with the feedforward component (Figure 4.28) provides superior disturbance attenuation and reference tracking when compare to both the nominal and force feedback only cases (Figure 4.27).
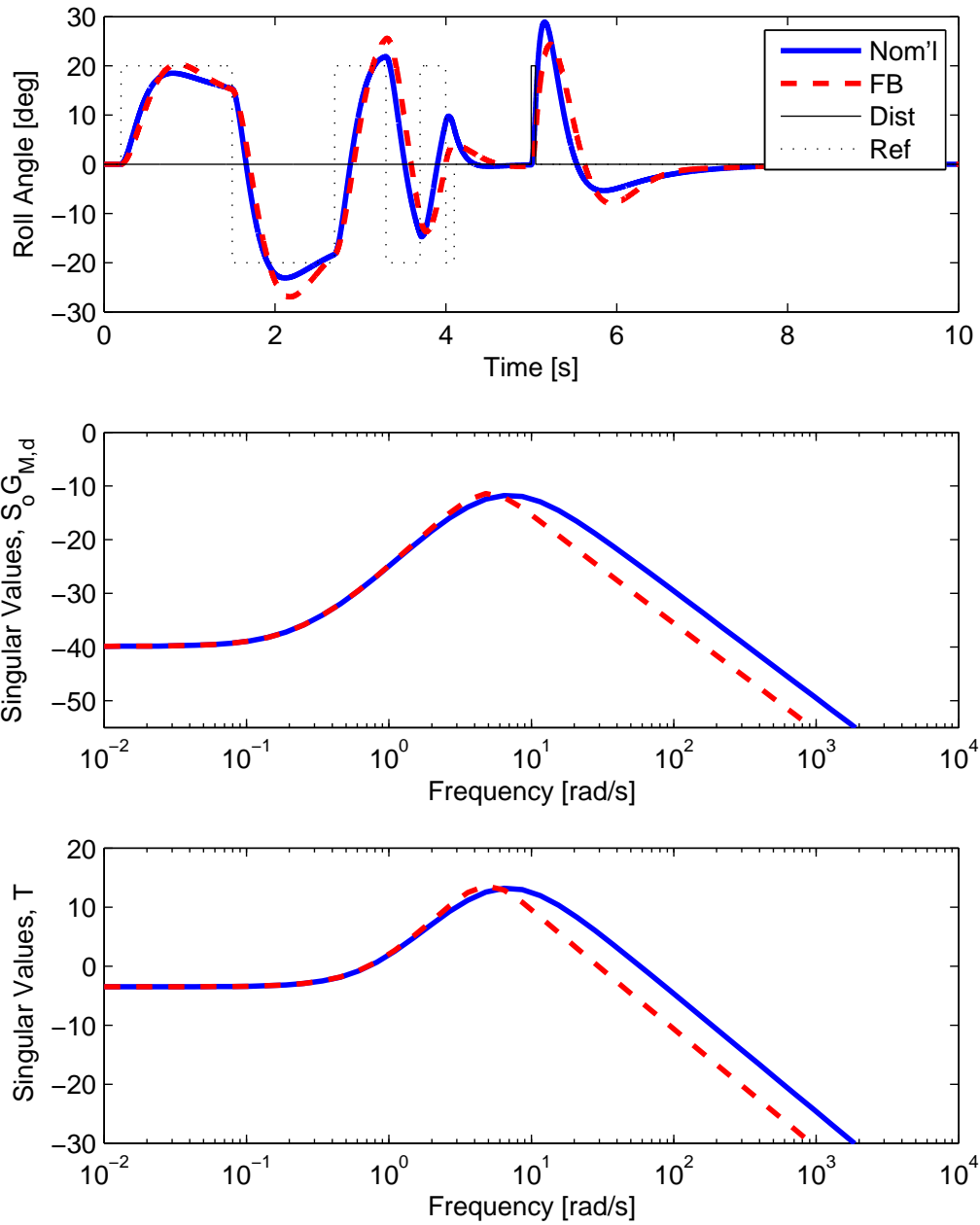
Figure 4.27: Simulated roll response time history for nominal attitude feedback (blue), force feedback (red) and singular value plots of $S_oG_{M,d}$ and T_o
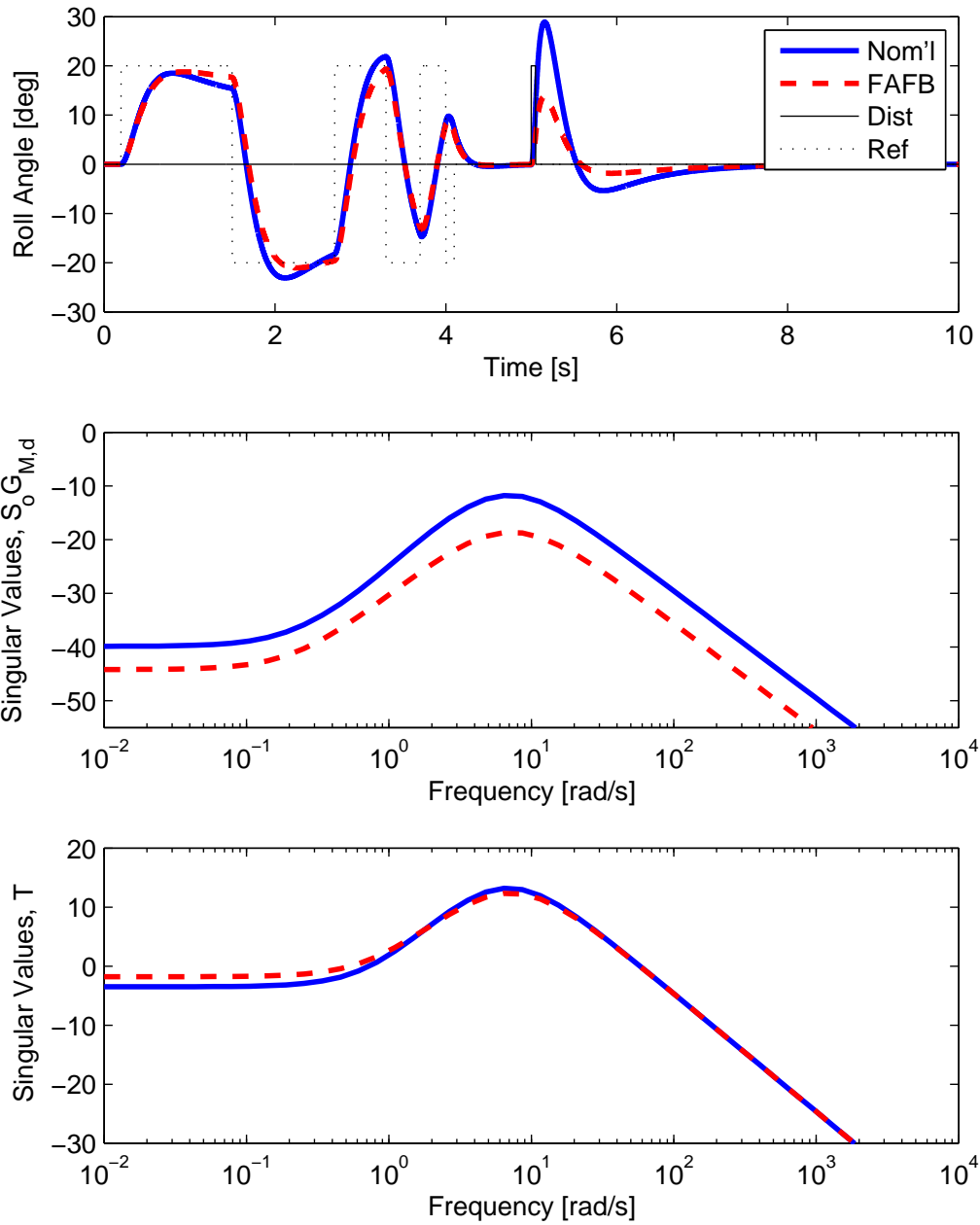
Figure 4.28: Simulated roll response time history for nominal attitude feedback (blue), force-adaptive feedback with feedforward (red) and singular value plots of $S_o G_{M,d}$ and T_o

Figure 4.30 illustrates the effects of measurement noise in the accelerometers on the system output. Figure 4.30b shows the angular acceleration estimated by the simulated accelerometer array with and without noise, shown in green and red respectively. Figure 4.30a shows the resulting roll angle tracking and impulse roll disturbance rejection for these cases. Clearly, even for highly noisy acceleration estimates, the accuracy of the roll angle tracking is not significantly diminished. Figure 4.30c confirms this result via the singular values of the transfer function mapping measurement noise $\boldsymbol{n}$ to output $\boldsymbol{y}$ (Figure 4.29). Attenuation of this transfer function is shown as the noise frequency increases. This is a positive result, as sensor noise is typically characterized by relatively higher frequencies.
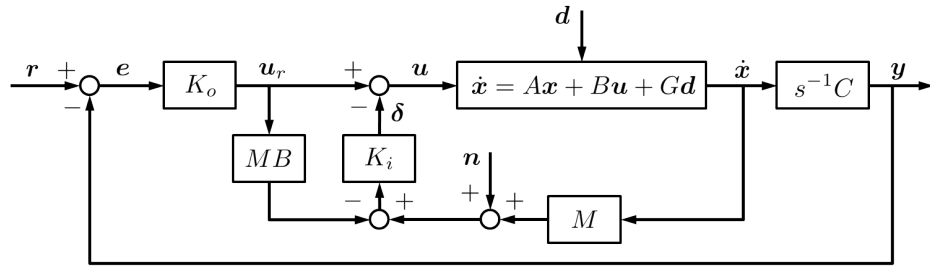
Figure 4.29: State space block diagram of attitude tracking loop with feedback-feedforward from accelerometers with noise
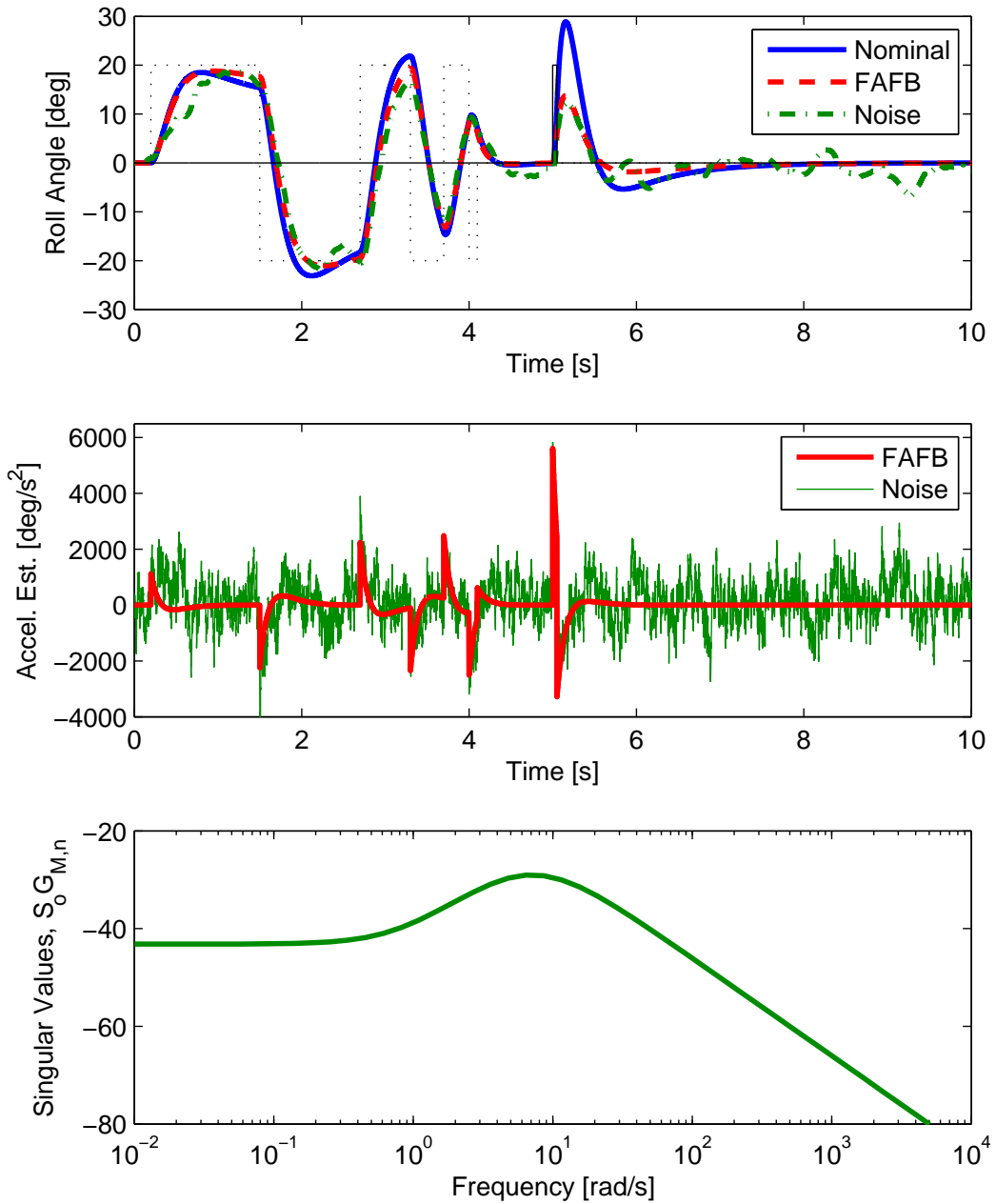
Figure 4.30: Simulated roll response time history for nominal attitude feedback (blue), force-adaptive feedback (red) with noise (green), acceleration estimate without noise (red) and without noise (green), and singular value plot of $S_oG_{M,n}$

125

4.2.3.2 Implementation Performance Analysis

The control laws described in (4.40), (4.41), and Figure 4.12 based on the reduced-order model detailed in Section 4.2.2.2 were implemented on the DJI quadrotor. Force feedback on the vehicle was provided via estimates of translational and angular acceleration, a_y and $\dot{p}$ respectively, from the distributed accelerometer array characterized in Section 3.4. As with the disturbance rejection performed for the ocellar sensor, detailed in Section 4.1.1, additive impulse disturbances were injected into the motor speed controller commands. This allowed for repeatable precise, disturbances to best compare the control strategies. Figure 4.31 displays the results of this closed-loop implementation. The mean trajectory over 10 total trajectories for each control case, nominal and force-adaptive feedback (FAFB) respectively, are shown with a solid bold line, with the variance across trajectories shown as shaded bands. Attenuation of the disturbance can be clearly seen from these results and correlates to the simulated disturbance response shown in Figure 4.30, validating our simulation results. To quantify the performance of the controllers, the 2-norm of the mean error signal, $e(t)$, is calculated as

$$||e(t)||_2 \equiv \left(\int_{-\infty}^{\infty} e(t)^2 dt \right)^{1/2} \tag{4.64}$$

where the mean error signal is defined as the deviation of the mean trajectory from zero. The performance of the disturbance rejection is quantified and summarized in Table 4.4.
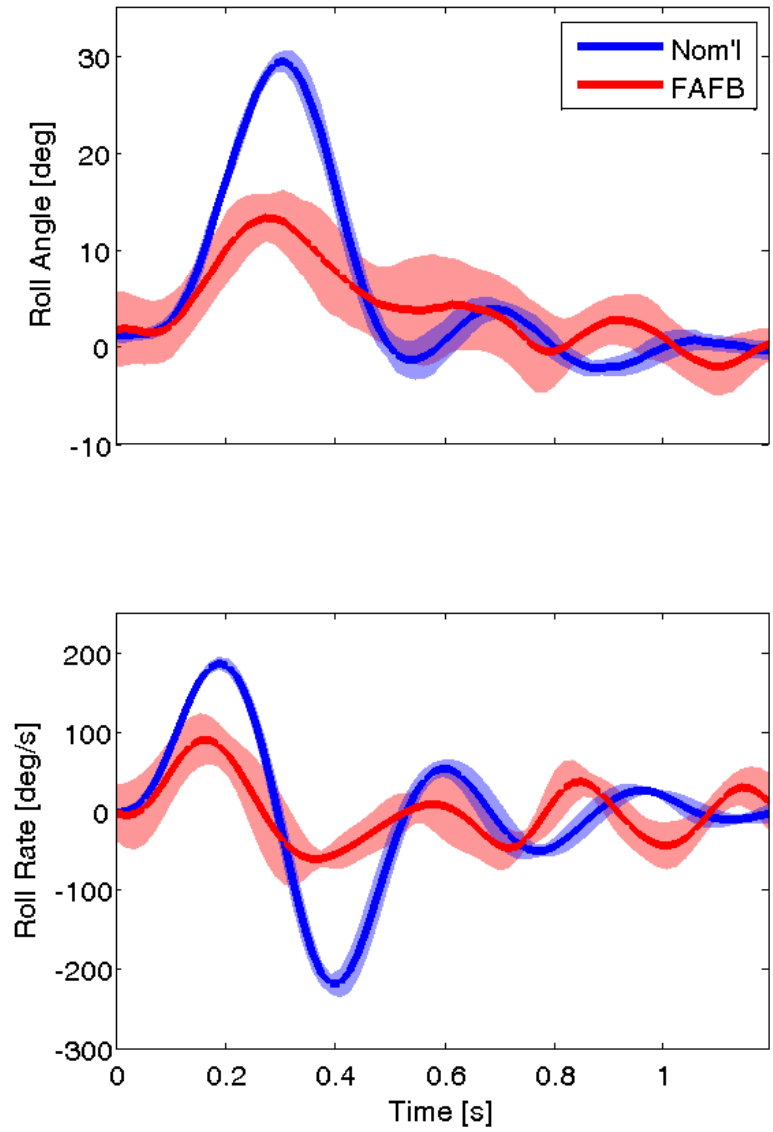
Figure 4.31: Roll response for with force-adaptive feedback as shown in Figure 4.12

From the results summarized in Table 4.4, the mean peak response $\bar{M}_p$ and mean error norm $||e(t)||_2$ yield improvements of 54% and 48% respectively when the FAFB control is implemented in comparison to the nominal attitude control.

Table 4.4: Distributed acceleration actuator disturbance rejection performance metrics

Control Case	$\bar{M}_p$ [deg]	$||e(t)||_2$ [deg]
Nominal	29.4	92.4
FAFB	**13.4**	**48.0**

Using this same control, rejection of disturbances from an external gust source was performed. As before, the mean taken over 10 trajectories for each control case is shown in Figure 4.32 with a solid bold line, with the variance shown as a shaded band. The location and direction of the gust source is shown with a black arrow. This gust source produced a nominal freestream velocity of 15 m/s at a distance of 0.5 m from the source, i.e. the mean distance between the vehicle center and the source when it was imparted. The level of disturbance rejection attained for each of these cases was characterized by quantifying the deviation of the mean trajectories away from the desired path. As these implementations do not include an outer loop position tracking control and are effectively open loop in the position states, the initial undisturbed path may be used to indicate the desired path subsequent to the disturbance. To do this, the trajectories were detrended for each control case based on the mean trajectory prior to reaching the gust source. Extrapolations of these trend lines, considered to be the desired paths, are shown as dashed lines in Figure 4.32. Having detrended the mean trajectories, the 2-norm of the mean error signal $e(t)$ as given by (4.64) was calculated, where the mean error signal was defined as the difference between the mean trajectory after encountering the gust and the extrapolated linear trend lines. The respective values of the performance
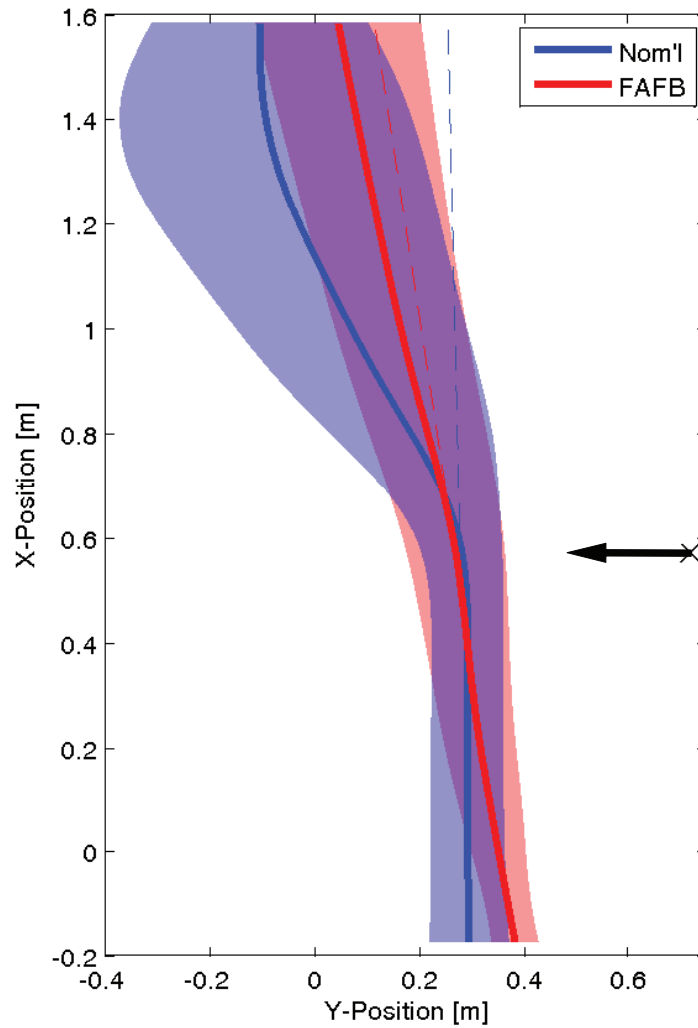
Figure 4.32: Trajectories in response to lateral gust source (black) with force-adaptive feedback control as shown in Figure 4.12, desired paths shown (dashed)

metric $||e(t)||_2$ for the nominal and FAFB control cases are shown in Table 4.5.

This defined performance metric for gust rejection yields a 82% improvement in gust rejection with force-feedback control. From Table 4.5 it is also evident that there is a 81% improvement in disturbance rejection when considering peak deviation $\bar{M}_p$,

Table 4.5: Distributed acceleration gust disturbance rejection performance metrics

Control Case	$\bar{M}_p$ [m]	$||e(t)||_2$ [m]
Nominal	0.36	1.89
FAFB	**0.069**	**0.34**

from the desired path.

Thus we have successfully demonstrated and quantified closed-loop implementation of the rejection of undesired forces and torques on a quadrotor in the form of both actuator disturbances and exogenous wind gusts, with feedback via force and torque estimates from a distributed array of accelerometers affixed to the vehicle airframe.

Chapter 5: Conclusions

This thesis provides the framework for and demonstrates the feasibility of analog implementable, and therefore highly scalable, mechanisms for improving the stability and gust tolerance of small unmanned aircraft systems. Biologically inspired models of the sensing systems common to several species of flying insects were the basis for the design, fabrication, implementation, and testing of two attitude stabilization and disturbance rejection sensing mechanisms. Through analysis of biological sensing mechanisms and their underlying physical functions and inherent advantages, in terms of noise reduction, information extraction, and rapid responsiveness, two novel sensors were developed. This is the first effort to implement a fully analog ocellar sensor for rate feedback stabilization of a flight vehicle. This is also the first work to implement a distributed array of redundant acceleration sensors to estimate the full 6-DOF acceleration state of a flight vehicle for disturbance rejection.

The outcome of this thesis is the design of two sensing modalities, supported by analytical, simulation, characterization, and implementation results, that augment the stability and gust tolerance of a flight vehicle, in a highly scalable framework. The approach for the design and implementation of each of these systems was not

to replicate the response of their biological analogues in a fully bio-mimetic sense. Instead, the goal was to determine and formalize the characteristics of the respective sensing modalities that provide useful, robust, and scalable state estimate architectures that may be transitioned to engineering solutions. For each of these systems a key result is shown, that static linear estimation from sensor measurements may be used to produce robust and rapid estimates of the respective vehicle motion states. This characteristic is critical in that it makes implementations of the sensors in analog-VLSI possible, and thereby provides the path to extreme miniaturization. Additionally, each of the sensing systems designed and detailed in this work are capable of providing their respective states estimates with comparable or improved speed when compared to alternative sensing systems.

The technical contributions from this work are listed below:

1. A model of the ocelli in flying insects and a method of static linear estimation of the pitch and roll rates from its outputs was developed.

2. A method for the static linear estimation of force and torque from a spatially distributed array of acceleration measurements was developed

3. A fully analog sensor was designed and fabricated to replicate the response of the ocellar visual system, producing static estimates of pitch and roll rate.

4. An array of arbitrarily placed linear accelerometers was constructed, static linear estimation of the acceleration states was implemented in hardware, and an automatic calibration algorithm was developed.

5. Stabilizing rate feedback from an analog ocellar sensor on a sUAS was demonstrated in the presence of actuator disturbances.

6. Disturbance rejection feedback from a spatially distributed accelerometer array was demonstrated in the presence of actuator and gust disturbances.

Elaborating on these unique technical contributions a summary of the results produced in this work is presented here. The ocellar model was based on the anatomical, functional, and electrophysiological characteristics in insects and its outputs were found to linearly and robustly encode angular velocity, in a cluttered urban 3-D simulation environment. This simulation result was used to validate a geometrically derived, but simplified, analytical ocellar model for egomotion sensing. The mathematical framework for the linear static estimation of the 6-DOF force and torque vector from spatially distributed array of arbitrarily located and oriented linear acceleration measurements was developed. From simulation of the distributed acceleration estimation methodology, empirical relationships between the force-torque estimate accuracy and the sensor noise, position error, and sensor number were developed. Using the ocellar simulation model a fully analog sensor was designed and fabricated to replicate the response of the model. In addition to mimicking the response of insect ocelli to luminance stimuli, static analog estimation of pitch and roll angular velocities was built into the sensor circuitry. The response of the sensor output estimates were compared to inertial and visual methods of angular velocity estimation. This comparison demonstrated improvements in sensor response speed when compared to the various other methods of egomotion estima-

tion. This characterization illustrated, in hardware, the complementary spectral responses between the ocelli and compound eye analog across a range of input excitation frequencies. A redundant array of arbitrarily placed, but rigidly connected linear MEMS digital accelerometers was designed and constructed. An automatic calibration algorithm was developed to estimate the position, orientation, gain, and bias of the sensors from ground truth measurements from and external motion capture system. Static linear estimation of the acceleration states that comprise the force-torque vector was implemented in digital hardware, and the response of the acceleration estimate was characterized. The first implementation of rate feedback from an analog ocellar sensor on a sUAS was demonstrated. The closed loop stabilization and disturbance rejection performance of the sensor was characterized and found to provide comparable stability to a MEMS inertial implementation. The first implementation of combined complementary ocellar and optic flow rate feedback on a sUAS for stabilization was demonstrated. The first implementation of a redundant array of linear accelerometers to estimate force and torques for disturbance rejection feedback on a sUAS was demonstrated.

Chapter 6:   Future Work

Several potential directions may be taken to expand on the work presented in this thesis. Initial efforts might likely be focused on expanding the stabilization and disturbance rejection implementation, discussed in Section 4.2.1.4, to additional degrees of freedom requiring further modeling of the system vehicle dynamics. A full 6-DOF controller implementation that is capable of tracking accelerations accurately may also be useful in aggressive maneuvering where precise following of acceleration trajectories is desired.

It would also be a logical next step to fuse these two sensing modalities with an optic flow sensor, to perform navigation, stabilization, and disturbance rejection. Development of fully analog solutions for all three of these sensing mechanisms would also allow for transition to smaller platforms. Further miniaturization of the sensing modalities would aid in fully demonstrating their advantages, as vehicle scale diminishes and bandwidth requirements increase.

Implicit in the static estimation of the forces and torques acting on the vehicle with distributed accelerometers is the assumption that the sensor and the airframe are rigidly connected. In applying this sensing technique to more flexible aircraft, such as traditional fixed-wing platforms, structural motions will need to be account-

ed for in the estimation scheme. To that, a similar array of strain sensors, spatially distributed across the airframe, could provide real-time measurements of the position of the accelerometers in the body frame, providing a solution to (2.39) for the non-rigid case.

Chapter A: Distributed Accelerometer Block Diagram Manipulation

The nominal state space aircraft system may be represented with the block diagram in Figure A.1, as defined in Section 4.2.1.2 with reference r, error e, control
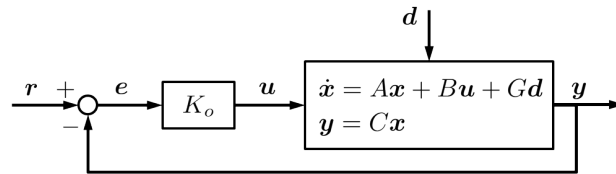
Figure A.1: State space block diagram with feedback from IMU

command u, disturbance d, and system output y. The outer loop attitude controller K_o stabilizes the plant, represented by typical dynamic, control, disturbance, and measurement matrices, A, B, G, and C respectively. Through block diagram manipulations, the system may be represented in a typical robust framework as in Figure A.2 where the manipulated control K_M and manipulated plant G_M are given
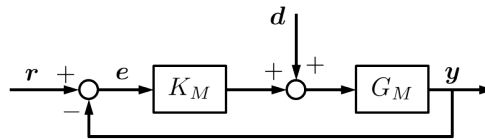
Figure A.2: Manipulated state space block diagram with feedback from IMU

by

$$K_M = G^{-1}BK_o \tag{A.1}$$

$$G_M = C(sI - A)^{-1}G \tag{A.2}$$

The loop transfer function L_o, when viewing the system from the output $\boldsymbol{y}$ as is typical, is defined

$$L_o \equiv G_M K_M \tag{A.3}$$

The sensitivity and complementary sensitivity transfer functions, S_o and T_o, are defined

$$S_o \equiv (I + L_o)^{-1} \tag{A.4}$$

$$T_o \equiv L_o(I + L_o)^{-1} \tag{A.5}$$

where the mapping from reference $\boldsymbol{r}$ to output $\boldsymbol{y}$ is given by T_o, and the mapping from disturbance $\boldsymbol{d}$ to output $\boldsymbol{y}$ is given by $S_o G_M$, that is

$$\boldsymbol{y} = T_o \boldsymbol{r} + S_o G_M \boldsymbol{d} \tag{A.6}$$

These transfer functions may be used to quantify the response of the system to various inputs in a robust context, via the singular values as detailed throughout Section 4.2.

Introducing the force-adaptive feedback (FAFB) with feedforward control as

detailed in Section 4.2.1.4 with feedback from the accelerations states within $\dot{\boldsymbol{x}}$, the block diagram is modified as shown in Figure A.3. Here the output of the plant is
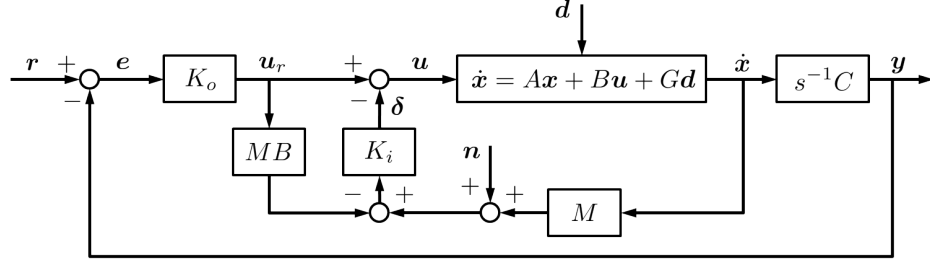
Figure A.3: State space block diagram with force feedback-feedforward

considered to be $\dot{\boldsymbol{x}}$ rather than $\boldsymbol{y}$ and additive noise in the acceleration estimates is represented with $\boldsymbol{n}$. The inner loop FAFB controller K_i is defined as in (4.41).

Starting with this complex block diagram, several manipulations must be performed in order to reach a system similar to that in Figure A.2. Firstly, this new system plant may be broken into two dynamic systems, defined as P and H, with inputs from control command $\boldsymbol{u}$ and disturbance $\boldsymbol{d}$ respectively. The output of these two systems are components of the state derivative that may be superposed to yield the total state derivative $\dot{\boldsymbol{x}}$. Defining the systems P and H as in (4.18) and repeated here

$$P \equiv s(sI - A)^{-1}B, \quad H \equiv s(sI - A)^{-1}G \tag{A.7}$$

the block diagram is represented by Figure A.5 The feedforward component of the control may be collected into a single term (Figure A.6). Moving the transfer function P before the summation yields Figure A.7. Then placing the noise input summation after the PK_i block results in Figure A.8. Simplifying the feedback loop
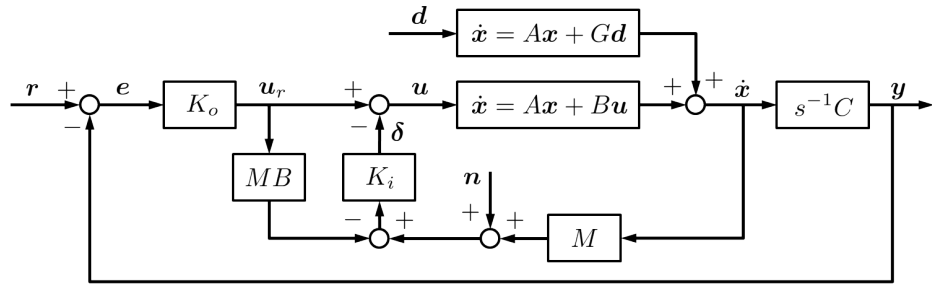
Figure A.4: State space block diagram with force feedback-feedforward with separated plant
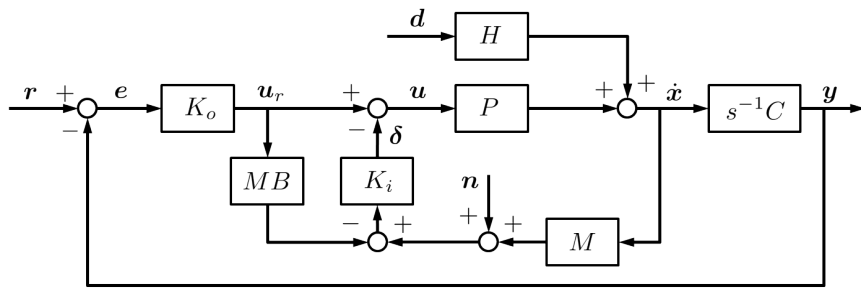
Figure A.5: State space block diagram with force feedback-feedforward with simplified separated plant
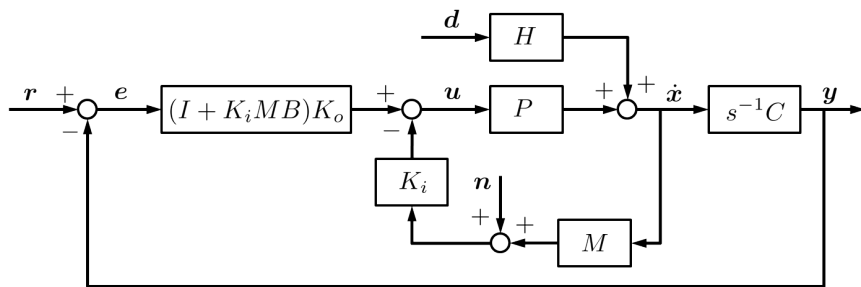
Figure A.6: State space block diagram with force feedback-feedforward with collapsed feedforward component

yields Figure A.9. Finally, pushing the terms H and PK_i into the loop yields the system in a typical robust analysis formulation. As the responses of the system out-
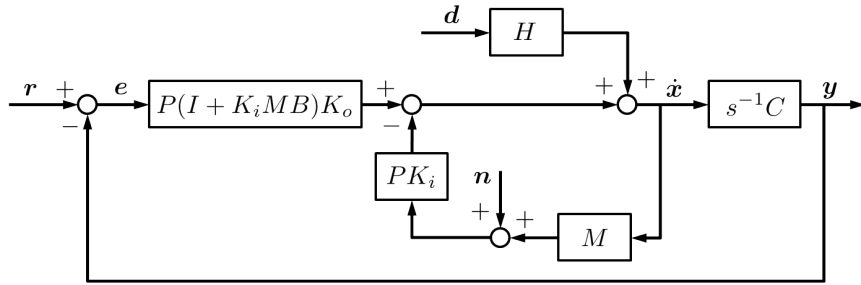
Figure A.7: State space block diagram with force feedback-feedforward with advanced plant
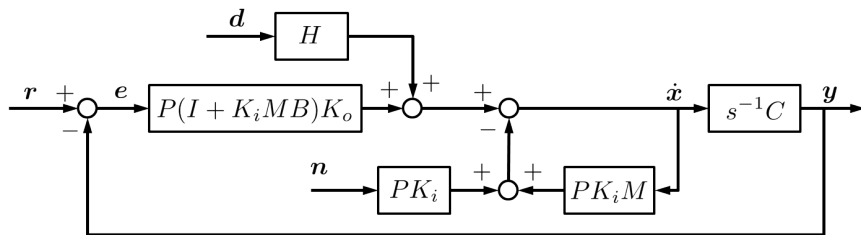
Figure A.8: State space block diagram with force feedback-feedforward with postponed noise
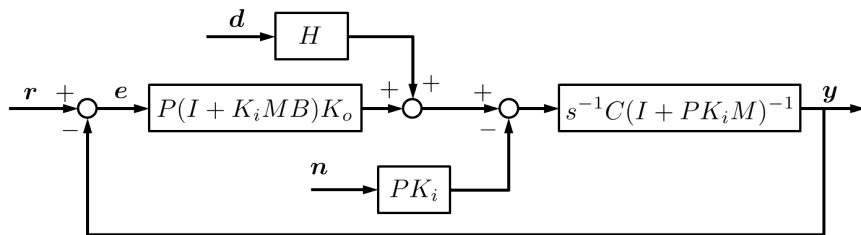
Figure A.9: State space block diagram with force feedback-feedforward with collapsed feedback

put to the various inputs may be superposed to yield the total response, the robust analysis may be similarly performed component-wise. For the case without noise in the acceleration state estimates, i.e. $\boldsymbol{n} = 0$, this system simplifies to the case shown in Figure A.11 (Figure A.2) where the transfer functions that comprise the loop are
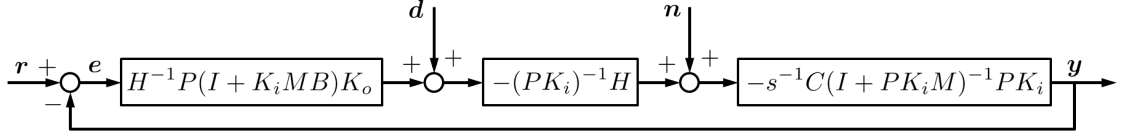
Figure A.10: Manipulated state space block diagram with force feedback-feedforward
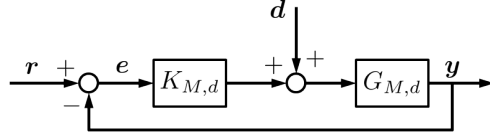
Figure A.11: Manipulated state space block diagram with force feedback-feedforward with disturbance

instead defined as

$$K_{M,d} = H^{-1}P(I + K_i MB)K_o \tag{A.8}$$

$$G_{M,d} = s^{-1}C(I + PK_i M)^{-1}H \tag{A.9}$$

and thus, through the relationships defined in (A.3), (A.4), and (A.5), the mappings from reference and disturbance to output are

$$
\begin{aligned}
\boldsymbol{y} &= s^{-1}C(I + PK_i M)^{-1}P(I + K_i MB)K_o \left(I + s^{-1}C(I + PK_i M)^{-1}P(I + K_i MB)K_o\right)^{-1}\boldsymbol{r} \\
&= T_o \boldsymbol{r} \tag{A.10}
\end{aligned}
$$

$$\boldsymbol{y} \;=\; s^{-1}\left(I + s^{-1}C(I + PK_iM)^{-1}P(I + K_iMB)K_o\right)^{-1} C(I + PK_iM)^{-1}H\boldsymbol{d}$$

$$\;=\; S_oG_{M,d}\boldsymbol{d} \tag{A.11}$$

Alternatively, for the case of a system with noisy acceleration estimates and no exogenous disturbance, i.e. $\boldsymbol{d} = 0$, as shown in Figure A.12, the functions that comprise the loop are defined as

$$K_{M,n} = -(PK_i)^{-1}P(I + K_iMB)K_o = -K_i^{-1}(I + K_iMB)K_o \tag{A.12}$$

$$G_{M,n} = -s^{-1}C(I + PK_iM)^{-1}PK_i \tag{A.13}$$

The loop and complementary sensitivity transfer functions, L_o and T_o, and thus
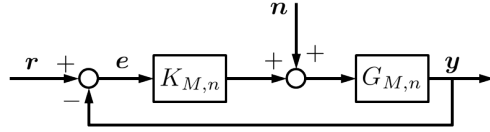
Figure A.12: Manipulated state space block diagram with force feedback-feedforward with noise

the mapping from reference to output remain unchanged (A.10). Furthermore, the mapping from estimate noise to output is given by

$$\boldsymbol{y} \;=\; -s^{-1}\left(I + s^{-1}C(I + PK_iM)^{-1}P(I + K_iMB)K_o\right)^{-1} C(I + PK_iM)^{-1}PK_i\boldsymbol{n}$$

$$\;=\; S_oG_{M,n}\boldsymbol{n} \tag{A.14}$$

Using this more complex formulation, the case of force feedback without feedforward, as in Section 4.2.1.3, may be analyzed by simply setting the MB terms in (A.10) and (A.11) to 0. This yields mappings from reference to output

$$
\begin{aligned}
\boldsymbol{y} &= s^{-1}C(I + PK_iM)^{-1}PK_o\left(I + s^{-1}C(I + PK_iM)^{-1}PK_o\right)^{-1}\boldsymbol{r} \\
&= T_o\boldsymbol{r} \quad\quad\quad\quad\quad\quad\quad\quad\quad\quad\quad\quad\quad\quad\quad\quad\quad\quad\quad\quad\quad\text{(A.15)}
\end{aligned}
$$

and disturbance to output

$$
\begin{aligned}
\boldsymbol{y} &= s^{-1}\left(I + s^{-1}C(I + PK_iM)^{-1}PK_o\right)^{-1}C(I + PK_iM)^{-1}H\boldsymbol{d} \\
&= S_oG_{M,d}\boldsymbol{d} \quad\quad\quad\quad\quad\quad\quad\quad\quad\quad\quad\quad\quad\quad\quad\quad\quad\quad\quad\text{(A.16)}
\end{aligned}
$$

Bibliography

[1] Ben Motazed, David Vos, and Mark Drela. Aerodynamics and flight control design for hovering micro air vehicles. In *Proceedings of the 1998 American Control Conference*, volume 2, pages 681–683. IEEE, 1998.

[2] Thomas Kordes, Marco Buschmann, Stefan Winkler, Hanns-Walter Schulz, and P Vorsmann. Progresses in the development of the fully autonomous mav carolo. In *2nd AIAA Unmanned Unlimited Systems, Technologies, and Operations Aerospace*, 2003.

[3] Richard K Arning and Stefan Sassen. Flight control of micro aerial vehicles. In *AIAA Guidance, Navigation, and Control Conference and Exhibit*, pages 16–19, 2004.

[4] Jan Wendel, Oliver Meister, Christian Schlaile, and Gert F Trommer. An integrated gps/mems-imu navigation system for an autonomous helicopter. *Aerospace Science and Technology*, 10(6):527–533, 2006.

[5] Wei Wang, Yong Zhou, Feng Wang, Yang Cheng, Yuze Song, and Kenzo Nonami. Attitude controller design for a small size multi-rotor mav. *Information Engineering Letters*, 2(3), 2012.

[6] Graham K Taylor and Holger G Krapp. Sensory systems and flight stability: what do insects measure and why? *Advances in Insect Physiology*, 34:231–316, 2007.

[7] Holger G Krapp. Ocelli. *Curr Biol*, 19(11):R435–R437, 2009.

[8] M Srinivasan, SW Zhang, M Lehrer, and T Collett. Honeybee navigation en route to the goal: visual flight control and odometry. *J Exp Biol*, 199(1):237–244, 1996.

[9] HG Krapp and M Wicklein. Central processing of visual information in insects. *The senses: A comprehensive reference*, 1:131–204, 2008.

[10] Holger G Krapp, Roland Hengstenberg, et al. Estimation of self-motion by optic flow processing in single visual interneurons. *Nature*, 384(6608):463–466, 1996.

[11] Martin Wilson. The functional organisation of locust ocelli. *J Comparative Physiology*, 124(4):297–316, 1978.

[12] H Schuppe and Roland Hengstenberg. Optical properties of the ocelli of calliphora erythrocephala and their role in the dorsal light response. *J Comparative Physiology A*, 173(2):143–149, 1993.

[13] Joshua van Kleef, Richard Berry, and Gert Stange. Directional selectivity in the simple eye of an insect. *J Neurosci*, 28(11):2845–2855, 2008.

[14] Titus R Neumann and Heinrich H Bülthoff. Behavior-oriented vision for biomimetic flight control. In *Proceedings of the EPSRC/BBSRC international workshop on biologically inspired robotics*, pages 196–203, 2002.

[15] G Stange, S Stowe, J Chahl, and A Massaro. Anisotropic imaging in the dragonfly median ocellus: a matched filter for horizon detection. *J Comparative Physiology A*, 188(6):455–467, 2002.

[16] Karin G Hu, Heinrich Reichert, and William S Stark. Electrophysiological characterization of *drosophila* ocelli. *J Comparative Physiology*, 126(1):15–24, 1978.

[17] K Kirschfeld, R Feiler, and K Vogt. Evidence for a sensitizing pigment in the ocellar photoreceptors of the fly (*musca, calliphora*). *J Comparative Physiology A*, 163(4):421–423, 1988.

[18] Matthew M Parsons, Holger G Krapp, and Simon B Laughlin. Sensor fusion in identified visual interneurons. *Curr Biol*, 20(7):624–628, 2010.

[19] P Simmons, S Jian, and F Rind. Characterisation of large second-order ocellar neurones of the blowfly calliphora erythrocephala. *J Exp Biol*, 191(1):231–245, 1994.

[20] Simon B Laughlin, Matthew M Parsons, and Holger G Krapp. Sensor fusion for feedback control of gaze stabilisation in the fly. Technical report, DTIC Document, 2010.

[21] Roland Hengstenberg. Gaze control in the blowfly *calliphora*: a multisensory, two-stage integration process. *Seminars in Neuroscience*, 3(1):19–29, 1991.

[22] Gert Stange. The ocellar component of flight equilibrium control in dragonflies. *J Comparative Physiology*, 141(3):335–347, 1981.

[23] Stphane Viollet and Jochen Zeil. Feed-forward and visual feedback control of head roll orientation in wasps (polistes humilis, vespidae, hymenoptera). *J Exp Biol*, 216(7):1280–1291, 2013.

[24] Wei-Chung Wu, Luca Schenato, Robert J Wood, and Ronald S Fearing. Biomimetic sensor suite for flight control of a micromechanical flying insect: design and experimental results. In *IEEE International Conference on Robotics and Automation*, volume 1, pages 1146–1151. IEEE, 2003.

[25] Luca Schenato, Wei Chung Wu, and Shankar Sastry. Attitude control for a micromechanical flying insect via sensor output feedback. *Robotics and Automation, IEEE Transactions on*, 20(1):93–106, 2004.

[26] Titus R Neumann and Heinrich H Bülthoff. Insect inspired visual control of translatory flight. In *Advances in Artificial Life*, pages 627–636. Springer, 2001.

[27] L. Kerhuel, S. Viollet, and N. Franceschini. Steering by gazing: An efficient biomimetic control strategy for visually guided micro aerial vehicles. *Robotics, IEEE Transactions on*, 26(2):307–319, April 2010.

[28] Richard James Donald Moore, Saul Thurrowgood, Daniel Bland, Dean Soccol, and Mandyam V Srinivasan. A fast and adaptive method for estimating uav attitude from the visual horizon. In *IEEE/RSJ International Conference on Intelligent Robots and Systems*, pages 4935–4940. IEEE, 2011.

[29] Javaan Chahl, Sarita Thakoor, Naig Le Bouffant, Gert Stange, Mandyam V Srinivasan, Butler Hine, and Steven Zornetzer. Bioinspired engineering of exploration systems: a horizon sensor/attitude reference system based on the dragonfly ocelli for mars exploration applications. *J Robotic Systems*, 20(1):35–42, 2003.

[30] J. Chahl and A. Mizutani. Biomimetic attitude and orientation sensors. *Sensors Journal, IEEE*, 12(2):289–297, Feb 2012.

[31] M. Motamed and J. Yan. A review of biological, biomimetic and miniature force sensing for microflight. In *Intelligent Robots and Systems, 2005. (IROS 2005). 2005 IEEE/RSJ International Conference on*, pages 3939–3946, Aug 2005.

[32] Laurence H Field and Thomas Matheson. Chordotonal organs of insects. *Advances in Insect Physiology (United Kingdom)*, 1998.

[33] John William Sutton Pringle. The gyroscopic mechanism of the halteres of diptera. *Philosophical Transactions of the Royal Society of London. Series B, Biological Sciences*, pages 347–384, 1948.

[34] Robert L Chevalier. The fine structure of campaniform sensilla on the halteres of drosophila melanogaster. *Journal of morphology*, 128(4):443–463, 1969.

[35] David C Sandeman. Angular acceleration, compensatory head movements and the halteres of flies (lucilia serricata). *Journal of comparative physiology*, 136(4):361–367, 1980.

[36] G Nalbach. The halteres of the blowfly calliphora. *Journal of Comparative Physiology A*, 173(3):293–300, 1993.

[37] Roland Hengstenberg. Biological sensors: Controlling the fly's gyroscopes. *Nature*, 392(6678):757–758, 1998.

[38] Bradley H Dickerson, Zane N Aldworth, and Tom L Daniel. Control of moth flight posture is mediated by wing mechanosensory feedback. *The Journal of experimental biology*, pages jeb–103770, 2014.

[39] Ulrich Müller and Amanda Littlewood-Evans. Mechanisms that regulate mechanosensory hair cell differentiation. *Trends in cell biology*, 11(8):334–342, 2001.

[40] GL Smith, SS Bedair, BE Schuster, WD Nothwang, JS Pulskamp, CD Meyer, and RG Polcawich. Biologically inspired, haltere, angular-rate sensors for micro-autonomous systems. In *Society of Photo-Optical Instrumentation Engineers (SPIE) Conference Series*, volume 8373, page 44, 2012.

[41] Robert J Wood and Ronald S Fearing. Flight force measurements for a micromechanical flying insect. In *Intelligent Robots and Systems, 2001. Proceedings. 2001 IEEE/RSJ International Conference on*, volume 1, pages 355–362. IEEE, 2001.

[42] Julian FV Vincent, Sally E Clift, and Carlo Menon. Biomimetics of campaniform sensilla: measuring strain from the deformation of holes. *Journal of Bionic Engineering*, 4(2):63–76, 2007.

[43] Carlo Menon, Rebecca Brodie, Sally Clift, and Julian FV Vincent. Concept design of strain sensors inspired by campaniform sensilla. *Acta Astronautica*, 64(2):176–182, 2009.

[44] HB Chen and SG Zhang. Robust dynamic inversion flight control law design. In *Systems and Control in Aerospace and Astronautics, 2008. ISSCAA 2008. 2nd International Symposium on*, pages 1–6. IEEE, 2008.

[45] Barton J Bacon and Aaron J Ostroff. Reconfigurable flight control using nonlinear dynamic inversion with a special accelerometer implementation. *AIAA Paper*, 4565, 2000.

[46] Jeng-Heng Chen, Sou-Chen Lee, and Daniel B DeBra. Gyroscope free strapdown inertial measurement unit by six linear accelerometers. *Journal of Guidance, Control, and Dynamics*, 17(2):286–290, 1994.

[47] Kirill S Mostov, Andrey A Soloviev, and T-KJ Koo. Accelerometer based gyro-free multi-sensor generic inertial device for automotive applications. In *Intelligent Transportation System, 1997. ITSC'97., IEEE Conference on*, pages 1047–1052. IEEE, 1997.

[48] Chin-Woo Tan, Sungsu Park, Kirill Mostov, and Pravin Varaiya. Design of gyroscope-free navigation systems. In *Intelligent Transportation Systems, 2001. Proceedings. 2001 IEEE*, pages 286–291. IEEE, 2001.

[49] Grace A Clark. Angular and linear velocity estimation for a re-entry vehicle using six distributed accelerometers: Theory. 2003.

[50] Andrew Hyslop, Holger G Krapp, and J Sean Humbert. Control theoretic interpretation of directional motion preferences in optic flow processing interneurons. *Biological cybernetics*, 103(5):353–364, 2010.

[51] Andrew M Hyslop and J Sean Humbert. Wide-field integration methods for autonomous navigation of 3-d environments. In *Proceedings of the 2008 AIAA guidance, navigation and control conference and exhibit*, 2008.

[52] Andrew M Hyslop and J Sean Humbert. Autonomous navigation in three-dimensional urban environments using wide-field integration of optic flow. *Journal of guidance, control, and dynamics*, 33(1):147–159, 2010.

[53] John L Crassidis and John L Junkins. *Optimal estimation of dynamic systems.* CRC press, 2011.

[54] Jerry M Mendel. *Lessons in estimation theory for signal processing, communications, and control.* Pearson Education, 1995.

[55] N Jeremy Kasdin and Derek A Paley. *Engineering dynamics: a comprehensive introduction.* Princeton University Press, 2011.

[56] Richard R Spencer and Mohammed Shuaib Ghausi. *Introduction to electronic circuit design.* Prentice Hall Upper Saddle River, 2003.

[57] Mandyam V Srinivasan. An image-interpolation technique for the computation of optic flow and egomotion. *Biol Cybern*, 71(5):401–415, 1994.

[58] Vladislav Klein and Eugene A Morelli. *Aircraft system identification: theory and practice.* American Institute of Aeronautics and Astronautics Reston, VA, USA, 2006.

[59] Sawyer B Fuller, Michael Karpelson, Andrea Censi, Kevin Y Ma, and Robert J Wood. Controlling free flight of a robotic fly using an onboard vision sensor inspired by insect ocelli. *Journal of The Royal Society Interface*, 11(97):20140281, 2014.

[60] James Sean Humbert, Andrew Hyslop, and Michael Chinn. Experimental validation of wide-field integration methods for autonomous navigation. In *IEEE/RSJ International Conference on Intelligent Robots and Systems*, pages 2144–2149, 2007.

[61] Joseph Conroy, Gregory Gremillion, Badri Ranganathan, and J Sean Humbert. Implementation of wide-field integration of optic flow for autonomous quadrotor navigation. *Autonomous Robots*, 27(3):189–198, 2009.

[62] Robert C Nelson. *Flight stability and automatic control*, volume 2. WCB/McGraw Hill, 1998.

[63] Richard C Dorf and Robert H Bishop. *Moderm Control Systems*. Addison-Wesley Publishing Company, 1995.

[64] Gene F Franklin, J David Powell, Abbas Emami-Naeini, and J David Powell. *Feedback control of dynamic systems*, volume 3. Addison-Wesley Reading, 1994.

[65] Sigurd Skogestad and Ian Postlethwaite. *Multivariable feedback control: analysis and design*, volume 2. Wiley New York, 2007.

[66] Arch W Naylor and George R Sell. *Linear operator theory in engineering and science*. Springer, 2000.

[67] Kemin Zhou, John Comstock Doyle, Keith Glover, et al. *Robust and optimal control*, volume 40. Prentice Hall New Jersey, 1996.

[68] Gregory M Gremillion, Lina M Castano, and J Sean Humbert. Disturbance rejection with distributed acceleration and strain sensing. In *AIAA SciTech Conference*, 2015.

[69] Brian L Stevens and Frank L Lewis. *Aircraft control and simulation*. John Wiley & Sons, 2003.

[70] Mark B Tischler and Robert K Remple. *Aircraft and rotorcraft system identification*. 2006.